CONTENTS

ABSTRACTS

Elena Bezvesilnaya, Yuryj Podchashinsky, Alexandr Dobrozhansky
Requirements for airborne gravimetry system

In the article the requirements to system for airborne gravimetry are formulated. A system for airborne gravimetry must consist of five functional subsystems for 1) specific force measurement, 2) geometric stabilization, 3) terrestrial navigation, 4) altimetry, and 5) computation. The general error of measurements of gravitational anomalies does not exceed 10 mgal. The accuracy requirement to main bodies of the block diagram of system for airborne gravimetry are determined ba-sed on analysis of errors of measurements.

Elena Bezvesilnaya, Yuryj Podchashinsky, Igor Korobyjchuk
Gravimeter with two-dimension digital processing of measuring information

Gravimeter with two-dimensional digital data processing about acceleration of gravity is considered in a paper. The result of measurements in gyroscopic gravimeter contains errors. An influence on gravimeter inertial absolute acceleration and other disturbing influences cause the errors of measurements. These of acceleration arise by work gravimeter onboard the plane in structure of air gravimetric system. The structural scheme of gyroscopic gravimeter is proposed in a paper for multiple precision. This construction is providing immediate measurements of acceleration of gravity. The possibility of digital data processing is considered in view of a two-dimensional character of an array of measuring information.

Mariusz Bogdan, Józef Błachnio, Marcin Derlatka
Computer-aided method of diagnostics of gas turbine blades

The article presents a computer-aided method of diagnostics of gas turbine blades with use of artificial neural networks. The subject of presentation is the developed neural network, with help of which – on the basis of features of blade surface images – realised is determination of their condition (operable element – inoperable element). Basing on conclusions formulated on the basis of microstructure examinations and concerning evaluation of state of overheating (blades suitable and not suitable for further operation), as patterns assumed were surface images representing blades in various states (neural pattern classification). Additionally, combining and segregating (according to their applicability for the network teaching process) image parameters, acquired from histograms as well as from matrix of events, automated and increased was the credibility (computer aiding) of decision process. The application of artificial neural network enables better representation of complex relations between blade image and its condition, than in the case of subjective methods used currently by diagnosticians.

Henryk Borowczyk, Paweł Lindstedt, Janusz Magier
A method of reliability characteristics estimation on the basis of adjustment and diagnostic information

The paper presents innovative method of reliability characteristics estimation on the basis of symptoms of parametric and temporary defects (prior to occurrence of catastrophic defects). The method is based on evident relations between adjustment, diagnostics and reliability, which are observed in an organised system of utilisation of each complex technical object.

Sergey G. Chulkin, Aleksandr D. Breki, Irina V. Soloviova, Mikhail M. Radkevich
Research of base and alloyed oil MC-20 influence on the tribotechnical characteristics of roller bearings

This article is devoted to research of the influence of an oil additive "serpentinite” on to roller bearings friction behavior. In this article the influence of the additive «serpentinite» on the roller bearings (208 series) friction behaviour is considered. It has been established that the serpentinite addition to the oil MC-20 allowed to reduce friction losses at the start-up of the mechanism 15-20% in comparison with the base oil.

Mykolas Daunys, Povilas Krasauskas, Romualdas Dundulis
Fracture toughness of 19Mn5 steel pipe welded joints materials

This paper presents an investigation of Ignalina NPP reactor’s main circulated circuit (MCC) pipeline welded joints materials fracture toughness properties. Standard compact C(T)-1T specimens containing “V” and “K” – type welds were cut off from the various MCC pipe’s zones, produced from the 19Mn5 steel pipe and welded by electrodes UTP-068HH, YONI-13/55 and CT-36. Critical J – integraf J_{Ic} values were defined Rusing J–R curve test method, which results on determination of J – integral values as a function of crack extension Δa. The investigation enables to calculate critical crack length Δa_{max} and Δa_c sizes and J – integral J_{Ic}, J_{max} and J_{Pmax} values, which are used to predict safe service lifetime of the cracked pipelines.

Tomasz Dzitkowski, Andrzej Dymarek
Synthesis and sensitivity of multiaxial drive systems

The selection of the dynamical properties of machines is one of the methods enhancing their durability and reliability. Such task may be accomplished with the use of the analysis and synthesis algorithm. Accordingly, the issue of the synthesis, enabling the determination of the parameters and structure of the systems in view of their dynamical characteristics, may be applied as a tool supporting the design process under any operating conditions. The scope of discussion is the mixed method of synthesizing dynamic characteristics enabling the derivation of the parameters and models of drive systems.

Sezgin Ersoy, Sertaç Görgülü
Computer based education and progress alternative for electro-mechanics lesson

The rapid developments in technology make it costly to educate the work force for the sectors. In modern technology and in today's world in which the education system is more modern and the need for modern stuff is increasingly high, Computer-Based Education (CBE) techniques and software are no more a luxury but a necessity. Because these softwares become the basic component and means of easy and comprehensible manner of telling in modern education system due to the visuality that they concern. This study presents the examples of material to make the content and the subject of electromechanics more effective and comprehensible.

Piotr Grześ
Finite element analysis of disc temperature during braking process

The aim of this paper was to investigate the temperature fields of the solid disc brake during short, emergency braking. The standard Galerkin weighted residual algorithm was used to discretize the parabolic heat transfer equation. The finite element simulation for two-dimensional model was performed due to the heat flux ratio constantly distributed in circumferential direction. Two types of disc brake assembly with appropriate boundary and initial conditions were developed. Results of calculations for the temperature expansion in axial and radial directions are presented. The effect of the angular velocity and the contact pressure evolution on temperature rise of disc brake was investigated. It was found that presented finite element technique for two-dimensional model with particular assumption in operation and boundary conditions validates with so far achievements in this field.

Andrzej Katunin, Anna Korczak
The possibility of application of B-spline family wavelets in diagnostic signal processing

Nowadays, wavelets are widely used in many applications, e.g. signal processing. The application of wavelet transform allows to obtain considerably more information about technical state of machine (especially for non-stationary signals) than traditional methods, e.g. Fourier transform. The aim of the paper is to analyze the goodness of B-spline family wavelets in diagnostic signal processing. Three types of B-spline wavelets were investigated. Their applicability was verified using degree of scalogram density on synthetic and operational signals. Results of the analysis of B-spline family wavelets show that proposed approach gives more accurate results in comparison with other chosen wavelets and can be applied in industrial diagnostics.

Robert Litwinko, Wiera Oliferuk
Yield point determination based on thermomechanical behaviour of polycrystalline material under uniaxial loading

The paper is devoted to yield point determination based on the thermomechanical coupling that takes place in the material during its uniaxial tension. Experiments were performed on aluminum alloy and on austenitic steels. The stress value corresponding to the temperature minimum is treated as the critical resolved stress at which plastic deforma-tion on the macroscopic scale begins. The obtained results are compared with values of stress which produces the irreversi-ble strain equal to 0.2%. Such value of the stress is usually regarded as the yield point determined from the stress-strain curve. It is found that the values of yield point determined on the ground of the thermomechanical coupling are lower than these obtained from stress-strain curve.

Stanisław Piróg, Tomasz Siostrzonek, Marcin Baszyński, Jarosław Czekoński
The control system of the flywheel energy storage

In this article authors described the control system for Flywheel Energy Storage. The device consists of the power electronic system and control system. The control system based on the FPGA. The power electronic system consists of the special rectifier and converter.

Małgorzata Poniatowska
Determining the uncertainty of the object coordinate system position in coordinate measurements of free-form surfaces

Coordinate measurements are a source of digital data in the form of coordinates of measurement points with a discrete distribution on the measured surface. Geometric deviations of free-form surfaces are determined at each point as normal deviations of these points from the nominal surface (a CAD model). The calculations are preceded by fitting the measurement data to the CAD model. The relations between the object coordinate system and the coordinate system of the machine are described by the transformation parameters. This paper presents the idea of the process of data fitting with the use of the least square algorithm method as well as the way of determining the uncertainty on the assumption that transformation parameters are subject to a multivariate normal probability distribution. The theoretical issues were verified by experiments carried out on a free-form surface obtained in the milling process and characterised by random geometric deviations.

Paweł Skalski, Krzysztof Woźnica, Jerzy Bajkowski
Parameters identification of bodner-partom model for fluid in MR damper

This paper presents an approach to describe a dynamic behaviour of magnetorheological damper by the Bodner-Partom constitutive law. The B-P equations usually used for metals are presented for shear stresses to express viscoplastic proprieties of MR fluid. Material parameters for the B-P law for fluid in the LORD RD 1005-3 damper are determined. Experimental results are compared with numerical results.

Valentyn Skalsky, Oleh Serhiyenko, Denys Rudavskyy, Yurij Matviyiv
Estimation of diagnostics of fibers failure in composite materials by the method of acoustic emission

The model of acoustic emission caused by formation of penny-shaped cracks in fiber composite materials taking into account stress relaxation in breaking fibers is proposed. It is found that the maximal values of components of displacement vector are directly proportional to the total area of defect, which is formed, and inverse proportional to the relaxation time.

Vasiliy Stavrov, Vladimir Lashkovski, Anatoly Sviridenok

A biomechanical model of operated achilles tendon

The paper discusses a biomechanical model reflecting deformation and tear of a tendon part, namely, ellipric in cross-section strand formed by stochastically located collagen fibers whose strain to stress relation obeys the exponential law. Recovery of the tendon by a plastic reinforcement is shown to result in elevated rigidity and shorter limiting elongation of the strand proportionally to the reinforced portion length, the strength of the restored strand being preserved almost fully. The limiting deformation of the recovered strand made with incisions for adaptation of the ends increases the more the deeper are the incisions, their number and the total length of the areas being adapted. This, nevertheless, decreases essentially the breaking load during further loading.

Tomasz Sudakowski

Premises of operational method of calculation of reliability of machines on the base of parametric and momentary symptoms of damage

In the article presented was the practical method of calculation of standard reliability characteristics of technical objects of unchanging and changeable structure during their work, based only on parametric and momentary symptoms of damage, the method of determination of symptoms of parametric damage on the base of diagnostic and momentary information and on the base of information about the state of adjustment of the object.

Heorhiy Sulym, Iaroslav Pasternak

Self-regular stress integral equations for the axisymmetric elasticity

The stress hypersingular integral equations of axisymmetric elasticity are considered. The singular and hypersingular integrals are regularized using the imposition of auxiliary polynomial solution, and self-regular integral equations are ob-tained for bounded and unbounded domains. The stress-BEM formulation is considered basing on the proposed equations. Considered numerical examples show high efficiency of the proposed approach. New problem for inclusion in finite cylinder is considered.

Kirill Voynov, Helen Chertok

Ball pump

A new and very effective ball pump is created. It can pump across the different liquids, for example: water, lubricants, oil, glycerine and even blood. Moreover it works not only like a pump but as a hydro-machine which can be applied in the various systems, namely, locomotives, robots and so on.

REQUIREMENTS FOR AIRBORNE GRAVIMETRY SYSTEM

Elena BEZVESILNAYA[*], Yuryj PODCHASHINSKY[**], Alexandr DOBROZHANSKY [**]

[*]Department of Instrument-making, National Technical University of Ukraine "KPI",
Peremogy str., 37, Kiev, 03056, Ukraine
[**]Department of Informational-computing Technology, Zhitomir State Technological University,
Chernyachovsky str., 103, Zhitomyr, 10005, Ukraine

bezvesilna@mail.ru, ju-p@ztu.edu.ua, victoriya_rh@rambler.ru

Abstract: In the article the requirements to system for airborne gravimetry are formulated. A system for airborne gravimetry must consist of five functional subsystems for 1) specific force measurement, 2) geometric stabilization, 3) terrestrial navigation, 4) altimetry, and 5) computation. The general error of measurements of gravitational anomalies does not exceed 10 mgal. The accuracy requirement to main bodies of the block diagram of system for airborne gravimetry are determined based on analysis of errors of measurements.

1. INTRODUCTION

A knowledge of gravity anomalies on a global scale is all that is required to determine the shape of the geoid and to map deflections of the vertical through use of the formulas of Stokes and Vening Meinesz. The computations involved require a relatively dense and accurate gravity net near the computation point, and less dense and accurate measurements over the rest of the world. The techniques of airborne gravimetry seem particularly suited to the task of supplying coarse data on remote regions of the world for use in conjunction with more accurate local nets established by surface measurements.

2. STRUCTURE OF SYSTEM FOR AIRBORNE GRAVIMETRY

A system for airborne gravimetry must consist of five functional subsystems for 1) specific force measurement, 2) geometric stabilization, 3) terrestrial navigation, 4) altimetry, and 5) computation (Bezvesilnaya, 2001; 2007). In determining the accuracy required of such a system, or in evaluating the utility of a given system, we must recall that the only use for global gravity data is the computation of geoid heights and deflections of the vertical. Overall system accuracy should then be evaluated in terms of the resulting accuracy in these computations. Although measurement accuracies on the order of ±1 to 3 mgal may ultimately be required, significant improvement in the existing gravity net would result from measurements accurate to 10 gmal.

Even with a high speed data gathering system such as an airborne gravimeter, we cannot hope to obtain an infinitely dense measurement net over the entire surface of the earth. The ultimate accuracy attainable in geoid heights and deflections of the vertical is limited by the density of the gravity net if the net is ideal (i. e. zero measurement error). A method for computing the error in geoid heights and deflections of the vertical due to a given measurement spacing is given in (Bezvesilnaya, 2007), and results are calculated for ideal measurement profiles spaced 2°, 4°, 10° and 20° apart. The question which must then be answered is, "What measurement accuracy is necessary along these profiles in order that no significant additional errors occur above those due to non-continuous gravity data cove rage?" The general steps in obtaining the answer to this question are as follows:

- The desired accuracy in computing geoid heights and deflections of the vertical must be specified by geodesists.
- Based on the existing worldwide gravity net and the economics of airborne system operation, the spacing of measurement profiles must be specified.
- Assuming perfect data in the form specified in b) to be available, an optimum interpolation scheme is used to predict anomalies at points between the measurement profiles, and the average error in these interpolated values is evaluated. The measurement errors along the profiles should then be small relative to this average interpolation error.

The average interpolation error in establishing a gravity anomaly profile between two data points:

$$\overline{\varepsilon^2} = C_0\left[1-\frac{\sigma}{d}+2\left(e^{2d/\sigma}-1\right)^{-1}\right], \tag{1}$$

where C – mean squared gravity anomalies over the whole earth, d – the distance between the two data points, σ – correlation length for gravity anomalies,

The procedures and reasoning outlined above will, in most cases, be of only academic interest to the design engineer, since he will most often be asked to provide the lowest overall system uncertainty possible within the state-of-the-art.

In attempting to determine surface gravity anomalies from measurements at altitude, two effects must be considered. First, gravity anomalies are attenuated at altitude, and the downward extension of airborne anomaly measurements will result in a surface map on which small amplitude variations have been filtered. Second, gravity measurements at altitude do not represent surface point anomalies, but give the weighted average of gravity anomalies over an area whose diameter is about 18 times the flight altitude. If the gravimeter output is further averaged in time, this area will be extended along the ground track of the aircraft.

Gravity anomalies are caused by mass anomalies in the earth's crust. Consider a hypothetical gravity anomaly Δg_0, measured at the earth's surface, due to a mass excess at a depth d beneath the surface. The magnitude of this anomaly is proportional to d^{-2}. If we now move a height h above the surface and again measure the gravity anomaly Δg_h, the result will be proportional to $(d + h)^{-2}$. Thus the gravity anomaly measured at altitude is attenuated with respect to surface value by a factor of

$$\frac{\Delta g_h}{\Delta g_0} = \frac{d^2}{(d+h)^2} = \frac{1}{\left(1+h/d\right)^2}. \qquad (2)$$

It should be noted that this attenuation is not corrected by the free air correction, which only takes account of the variation of reference gravity with altitude. The influence of this effect on an airborne gravimeter may be thought of in terms of an all-pass filter with variable attenuation connected to the output. This attenuation cannot be accurately compensated since the depth compensation of the Airy-Heiskanen isostatic system (~40 km), the attenuation factor becomes 0.64. In making this comparison, an attenuation correction was applied based on the known surface data. Such a correction would, of course, not be available
in an operational system. While downward continuation techniques can be used to reduce the anomalies measured at altitude to a sea level datum, they cannot recover the detail in the gravity field lost through attenuation into the noise level of the system. This then places a fundamental limitation on the amplitude resolution obtainable with airborne gravimetry systems.

The spatial resolution of an airborne gravimetry system will also be limited due to the fact that anomalies measured at altitude are influenced by anomalies over a sizable area on the ground. The gravity anomaly measured at an altitude h may then be thought of as a spatial average of surface anomalies over a circular area centered directly beneath the aircraft. In order to gain some insight as to the area involved, we may analyze a simplified model.

3. THE GRAVIMETER STABILIZATION SUBSYSTEM

In order to carry out a gravity survey from a moving vehicle, some means of stabilizing the gravimeter along a reference direction is required. Since it is ultimately necessary to deduce the specific force in the direction of the local geographic vertical, the direct instrumentation of the vertical provides the most desirable measurement environment. Instrumentation of the vertical on a moving base requires however, a rather complex subsystem using high-grade inertial navigation data. The drawbacks of complexity are reduced somewhat by the fact that such a stabilization system can also serve as the heart of a geographic inertial navigator.

As an alternate to stabilization along the vertical, the gravimeter may be allowed to track the apparent vertical, provided the proper compensation term is added to the gravimeter output. Stabilization along the apparent vertical also places a greater load on any gravimeter output-filtering scheme due to the presence of components of short term horizontal acceleration in the gravimeter output.

An airborne gravimetry system may be thought of as the instrumentation of a single dynamic equation, relating the outputs of the required subsystem to the indicated gravity anomaly. As this equation shows, the indicated gravity anomalies are obtained by compensating the output of a specific force sensor (gravimeter) which is stabilized along a vertical or apparent vertical axis. Four types of compensation term appear: 1) vertical accelerations of the aircraft, 2) Coriolis and centrifugal force corrections, sometimes called Eotvos corrections, 3) free air gravity reduction terms, and 4) the computed reference value of gravity at sea level. If an apparent vertical stabilization system is used, the Browne correction must also be applied. All but the first of these compensation terms can be easily computed from the outputs of the previously specified subsystems. The first term, aircraft vertical acceleration, is more difficult to deal with, because it cannot be measured directly due to the indistinguishability of gravitational and inertial accelerations. There remains the possibility of double differentiation of altitude data, separation by filtering and combinations of these techniques.

The sensitivities of the other, more readily computed compensation terms, to errors in the navigation and altimeter subsystem outputs. Compensation error due a given velocity measurement error varies with, both aircraft heading and latitude, the minimum sensitivity for any latitude occurring on a due west heading.

For a given specific force sensor uncertainty, the minimum system uncertainty results when the sensor is physically stabilized along the z axis (vertical axis) of an instrumented local geographic coordinate frame. Errors in the z axis alignment of such a frame result in 1.20 mgal error for each arc minute of misalignment due to projection of horizontal Coriolis forces along the measurement axis, and a smaller second order error which reaches 0.4 mgal at 3 arc minutes vertically error.

4. COMPENSATION OF VERTICAL ACCELERATIONS

In ground-based gravimetry, the term gravimeter has been applied to devices used to measure the difference between gravity at some reference point and at the measurement point. Although the term is still applied to these sensors when used in moving-base systems, they no longer indicate gravity changes alone, but the net specific force acting on a test mass. They are thus more correctly referred to as specific force sensors.

Several sensors developed for land or sea use, such as the LaCoste-Romberg, the Askania-Graf, and the Worden, have been modified for airborne use. These devices all have been successfully tested in an airborne environment, but they do have some disadvantages, primarily in the areas of data readout and dynamic range.

There exists a large class of specific force sensors developed for use as accelerometers in guidance and navigation system. Several of these sensors seem particularly well suited to use in airborne gravimetry systems. One of the more promising devices, the pendulous integrating gyro accelerometer or PIGA, is currently being readied for flight tests by the MIT Experimental Astronomy Laboratory under Air Force Cambridge Research Laboratory sponsorship.

It is probably neither economically nor technically feasible to choose a single navigation technique such as Doppler, inertial, etc. That can fully meet the requirements of an airborne gravimetry system. The rather specialized requirements for continuous accurate position and velocity output, together with the requirement for global capabilities, indicate the choice of a hybrid navigation system making use of both onboard measurements and navigation aids such as satellites. Specifically, a Doppler-inertial navigator used in conjunction with position fixes from a satellite navigation system would seem best suited. Such a system should be capable of indicating velocity to 0.5 knot or better and position to 0.5 mile or better for long duration flights at 500 knots.

An examination of the currently available sources of altitude data shows that a direct and continuous determination of sea-level altitude to the accuracy required by an airborne gravimetry system is not possible using any single source of information. Radar altimeter appears capable of supplying data on sea-level altitude to a sufficient accuracy, but only when over regular terrain or water of known elevation. Errors in determining atmospheric parameters cause prohibitively large errors in pressure altitude measurements relative to a sea-level datum. Pressure measurements can, however, be used to compute with adequate precision, the altitude deviations from a nearby isobaric surface. The hypsometer would seem to be the best-suited instrument for this measurement.

Combination of air-mass velocity measurements with ground velocity and heading information from the navigation system can, through use of Henry's correction, yield information on the slope of the isobaric surface being flown. Additional data on the height of this isobaric surface can be provided by periodic radar measurements, and by measurements made at surface weather stations.

Data from various sources can be combined in a manner assigned to minimize the mean-squared error in the resulting estimate. This estimate of isobaric surface height, together with the output of a hypsometer, can provide the required altitude data for gravimeter compensation.

The nature of the signal processing and filtering problem is, in most cases, such that post-flight data processing is possible. This allows the design of a filter free of the usual realizability constraints.

The noise present in the gravimeter output before filtering is mostly due to aerodynamic, wind, and turbulence loading of the airframe. These interfering forces result in aircraft accelerative that are partially counteracted by the autopilot system. The characteristics of the airframe – autopilot system will, in general, change with time, thus the truly optimum, filter should be adaptive in nature.

5. CONCLUSIONS

A system for airborne gravimetry must consist of five functional subsystems for 1) specific force measurement, 2) geometric stabilization, 3) terrestrial navigation, 4) altimetry, and 5) computation. In determining the accuracy required of such a system, or in evaluating the utility of a given system, we must recall that the only use for global gravity data is the computation of geoid heights and deflections of the vertical.

From the results of the error analysis,we see that an airborne gravimetry system capable of measurement accuracy of the order of 10 mgal, must be capable of nominal subsystem accuracy as follows (Bezvesilnaya, 2007):

- velocity over the ellipsoid 0.5 knot;
- latitude 1.0 mile;
- verticality 3.0 arc minutes;
- sea-level altitude 30 feet;
- specific force measurement 2 mgal.

For a system capable of accuracy on the order of 3 mgal, these subsystem requirements become:

- velocity
- no heading restriction 0.18 knot;
- no westerly headings 0.4 knot;
- latitude 0.5 mile;
- verticality 1 arc;
- sea-level altitude 10 feet;
- specific force measurement 1 mgal.

REFERENCES

1. **Безвесільна О.М.** (2001), В*имірювання прискорень: Підручник*. – К.: Либідь.
2. **Безвесільна О.М.** (2007), *Авіаційні гравіметричні системи та гравіметри*: Монографія. – Житомир: Житомирський державний технологічний університет.

GRAVIMETER WITH TWO-DIMENSION DIGITAL PROCESSING OF MEASURING INFORMATION

Elena BEZVESILNAYA[*], Yuryj PODCHASHINSKY[**], Igor KOROBYJCHUK[**]

[*]Department of Instrument-making, National Technical University of Ukraine "KPI",
Peremogy str., 37, Kiev, 03056, Ukraine
[**]Department of Informational-computing Technology, Zhitomir State Technological University,
Chernyachovsky str., 103, Zhitomyr, 10005, Ukraine

bezvesilna@mail.ru, ju-p@ztu.edu.ua, kiv-igor@list.ru

Abstract: Gravimeter with two-dimensional digital data processing about acceleration of gravity is considered in a paper. The result of measurements in gyroscopic gravimeter contains errors. An influence on gravimeter inertial absolute acceleration and other disturbing influences cause the errors of measurements. These of acceleration arise by work gravimeter onboard the plane in structure of air gravimetric system. The structural scheme of gyroscopic gravimeter is proposed in a paper for multiple precision. This construction is providing immediate measurements of acceleration of gravity. The possibility of digital data processing is considered in view of a two-dimensional character of an array of measuring information.

1. INTRODUCTION

The most perspective type of gravimeter based on dynamically customized gyroscope. The examples of realisations such gravimeter are reduced in (Odintsov, 1982). However many errors is inherent in it gravimeter. These errors can essentially distort result of measurements.

These errors are stipulated by that gravimeter measures a collection of acceleration of gravity (useful component of result of a measurement) and inertial absolute acceleration (parasite signal calling an errors of result of measurements). The inertial absolute acceleration is called by vertical acceleration of the plane, on which is installed gravimeter. The magnitude of such parasite signal can exceed magnitude useful component in result of measurements. The forward and angular vibrations of the plane also can reduce in essential errors of result of measurements.

Development of methods of compensating of these errors is actual task. The good result can be received on the based of applications of the digital computing device. This computing device fulfils algorithmic handling of result of measurements. Such handling includes a filtration of a measuring information from a feeler of gravimeter. Compression of a measuring information also applied for effective saving of this information to memory of computing device.

For effective application of methods of algorithmic handling it is desirable, that gravimeter measured immediately value of acceleration of gravity. For this purpose it is necessary to bring in some modifications to a construction of gravimeter. Centre of mass of a rotor of a two-degree dynamically customised gyroscope is displaced along it of axes of rotation. Also into the scheme of gravimeter are entered a transmitter of an angle of a turn, low-pass filter and device of an evaluation of an output signal gravimeter (digital computing device).

2. STRUCTURE AND MATHEMATICAL MODEL OF GRAVIMETER

Gravimeter (Fig. 1) contains a two-degree dynamically customized gyroscope (1) with a rotor (2). To a gyroscope are connected a transmitter of an angle of a turn (3), transmitter of a moment (4), low-pass filter (5) and device (6) for an evaluation of an output signal of gravimeter. The centre of mass of a rotor is displaced concerning it of an axes of rotation on magnitude l .

The multiple precision of measurements of acceleration of gravity is ensured because the centre of masses of a rotor is displaced concerning it of an axes of rotation. Therefore this gravimeter fulfils an immediate measurement of acceleration of gravity. These measurements are fulfilled with the help of transmitter of an angle of a turn.

This property is a possibility to execute a filtration of a measuring signal. The most part of a power of useful component of a measuring signal is concentrated on frequencies below 0.1 radian/sec (Line 2, Fig. 2). The most part of a power of errors in a measuring signal is concentrated on frequencies above 0.1 radian/sec (Line 1, Fig. 2). Therefore low-pass filter can execute a filtration of errors in a measuring signal. The device of an evaluation of an output signal will transform a result of a filtration to an output signal of gravimeter.

Also at use of the modern digital computing device there is a possibility to fulfil a filtration of a measuring signal
in view of its two-dimensional character. Thus it is necessary to accumulate result of measurements and to consider them in fixation to coordinates of points on a surface of the Earth.

Thus, the essential errors of measurements are eliminated from an output signal of gravimeter. If these errors to not eliminate, their magnitude can be commensurable with a value of a useful signal. Therefore offered method of handling of a measuring information allows essentially to increase of measurement accuracy of acceleration of gravity.

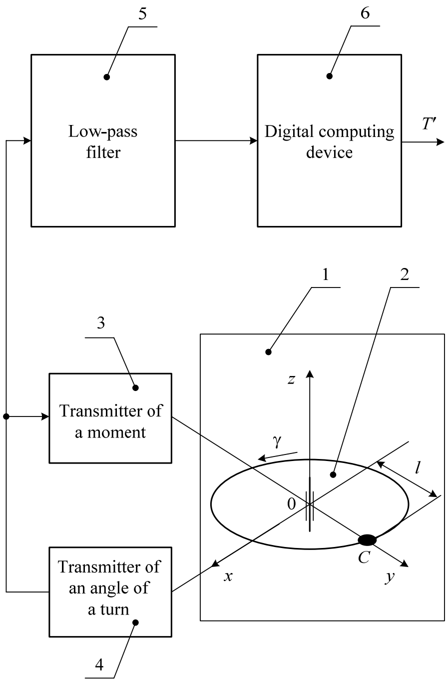

Fig. 1. The block diagram of gravimeter

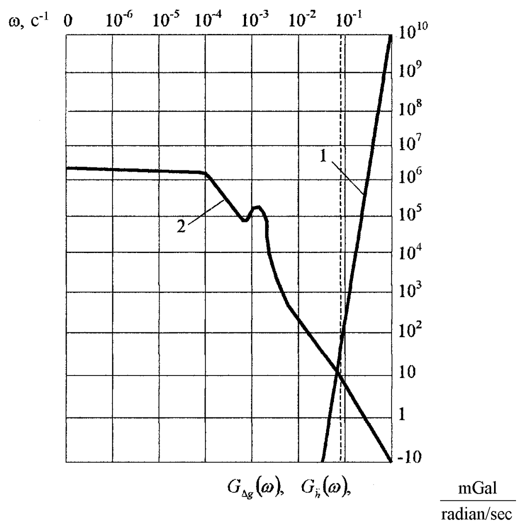

Fig. 2. The graph of a spectral denseness useful component and errors of results of measurements

Gravimeter works as follows. At exposition of work of gravimeter basic positions are taken from (Pavlovsky, 1986; Samotokin et al., 1986).

Rotor of a gyroscope rotation by an angular velocity γ. At a lack of exterior actions the rotor rotates in a horizontal plane. At presence of acceleration of gravity along an axes of rotation the moment M_g is created and the rotor begins to deviate:

$$M_g = mgl \cdot \cos\alpha , \tag{1}$$

where m – mass of a rotor, l – displacement of a centre of masses of a rotor concerning it of an axes of rotation, α – angle of a deviation of a rotor.

The moment $M_{\ddot{h}}$ from vertical acceleration $\ddot{h}$ along an axes of sensitivity of gravimeter is equalled:

$$M_{\ddot{h}} = m\ddot{h}l \cdot \cos\alpha . \tag{2}$$

The moment M_T elastic forces of the elements of a suspension bracket of a rotor is equalled:

$$M_T = C_x \alpha , \tag{3}$$

where C_x – rigidity of the elastic elements of a suspension bracket at their torsion.

The centrifugal moment M_u is equalled:

$$M_u = I\dot{\gamma}^2 \sin\alpha , \tag{4}$$

where I – moment of inertia of a rotor, γ – angular velocity of rotation of a rotor.

If to accept, that $\alpha << 1$ radian, it is possible to note:

$$C_x \alpha + I\dot{\gamma}^2 \alpha = -mlg + ml\ddot{h} . \tag{5}$$

From here, by designating $k = \tilde{N} + I\dot{\gamma}^2$, we obtain:

$$\alpha = -\frac{ml}{C + I\dot{\gamma}^2}\left(g + \ddot{h}\right) = -\frac{ml}{k}\left(g + \ddot{h}\right). \tag{6}$$

By designating $S=ml/k$, we obtain an entering signal of a low-pass filter:

$$T = \frac{1}{S}\alpha = -g + \ddot{h} . \tag{7}$$

From here

$$\alpha = \left(-g + \ddot{h}\right)S . \tag{8}$$

Thus, the angle α deviation of a rotor is proportional to acceleration of gravity g and vertical acceleration $\ddot{h}$ of the plane.

The output signal of a transmitter of an angle of a turn passes through the amplifier (in a Fig. 1 is not shown) with an amplification factor $1/S$ and come on an input of a low-pass filter. At an output signal of a transmitter of an angle of a turn also there are errors. These errors stipulated by forward and angular vibrations of the plane, on which gravimeter is installed. In view of these errors the input signal of a low-pass filter is defined of the formula:

$$T = \frac{1}{S}\alpha = -g + \ddot{h} - \left(R_x \alpha - R_y\right)\beta - \frac{B}{ml}\left(\dot{\omega}_x + \dot{\omega}_y \alpha\right) + \frac{M_{i2}}{ml} , \tag{9}$$

where: R_x, R_y – projection on an axes $0x$, $0y$ accelerations of forward vibrations of the plane, β – constant of proportionality, B – moment of inertia of a rotor of a gyroscope, $\dot{\omega}_x, \dot{\omega}_y$ – projection on an axes $0x, 0y$ accelerations of angular vibrations of the plane, M_{i2} – moment of tool errors of a two-degree dynamically customized gyroscope.

3. FILTRATION OF MEASURING INFORMATION IN GRAVIMETER

Frequency spectrum of acceleration of gravity and errors is different (Fig. 2, Lines 2 and 1). The dominant frequency of the first signal is equalled 0.00175 radian/sec. Dominant frequency of the second signal is equalled 0.269 radian/sec.

The low-pass filter has cutoff frequency 0.1 radian/sec and fulfils a filtration of a signal *T* with the purpose of an elimination of errors. In an outcome on an exit of a filter the output signal *T'* is obtained.

For a low-pass filter it is possible to note a relation (Goldenberg et al., 1990):

$$T'(\tau) = \int_{-\infty}^{\infty} w(t-\tau)T(\tau)d\tau \, , \tag{10}$$

where $w(.)$ – weight function of a filter.

The weight function of a filter is equalled:

$$w(t) = \int_{-\infty}^{\infty} W(j\omega)e^{j\omega\tau}d\omega = 2\omega_0\left[\frac{\sin\omega_0 t}{\omega_0 t}\right], \tag{11}$$

where $W(j\omega)$ – transfer function of this filter.

The output signal of a low-pass filter acts in a device of an evaluation of an output signal of gravimeter. This device calculates an output signal under the formula:

$$T'(\tau) = \int_{-\infty}^{\infty} 2\omega_0\left[\frac{\sin\omega_0(t-\tau)}{\omega_0(t-\tau)}\right]T(\tau)d\tau \, . \tag{12}$$

In this case $\tau = 2\pi n$ – slice of time of an evaluation of an output signal, n=1, 2,… – amount of full turnovers of an exterior framework of a gyroscope.

In an outcome the output signal *T'* is obtained which contains a measuring information about acceleration of gravity *g*. In this signal there are no all errors which dominant frequency exceeds 0.1 radian/sec. These errors are stipulated: accelerations of forward vibrations with dominant frequency 3140 radian/sec; accelerations of angular vibrations with dominant frequency 6.7, 10, 20, 40 and 60 radian/sec.

During evaluations $\tau = 2\pi n$ errors of a gyroscope completely will be eliminated. For a full turnover of an exterior framework these errors in turn equalled positive and negative values. On the average this error will be equalled to zero.

Thus, in an output signal of gravimeter a series of errors of measurements completely is compensated. It allows essentially increasing measurements accuracy of acceleration of gravity.

4. METHODS OF TWO-DIMENSIONAL DIGITAL PROCESSING OF MEASURING INFORMATION IN GRAVIMETER

The filtration of the gravity measuring information can be executed by the one-dimensional filter for the array of data. These data are received along one line of flight of aircraft gravity system. Such filtration is carried out during flight in rate of receipt of the data or at processing gravity measurements after flight.

In the given research other variant is offered also. It consists in formation two-dimensional array of the gravity measuring information on anomalies of acceleration of gravity. The array is formed in fixation to coordinates of points of a surface of the Earth, in which these data were received. This array corresponded to series lines of flight. After that carry out a filtration of the generated array with the help of two-dimensional digital low-pass filter. Two-dimensional correlation in a useful signal about anomalies of acceleration of gravity in addition take into account. Such filtration can be executed at processing results of gravity measurements after flight.

Interrelation of such approach with the basic requirements to gravimetric survey on some district are considered.

Known regional and detailed gravimetric survey (Malovichko and Kostitsyn, 1992). The regional gravimetric survey is displayed on cards of scale 1:200 000 with section of isolines through 2 mGal. The gravimetric survey is continuous. The cards, made by results of survey, give representations about general structure of an abnormal field, his basic features and regularity. The cards of anomalies are used at the decision of astronomical and geodetic tasks.
The anomalies at regional shooting also provide the decision of tectonic tasks.

The detailed gravimetric survey will be carried out in conditions, when the regional survey is already carried out and basic regularity and the properties of an abnormal field are known. The detailed survey differs from regional survey to structure of a network and flights, scales of cards and accuracy of definition of anomalies, ways of their processing and interpretation (Kostitsyn, 1989; Malovichko et al., 1989). In Table 1 (Malovichko and Kostitsyn, 1992; Instruction on Gravimetric Investigation, 1980) the basic characteristics of detailed gravimetric survey for flat country are given.

Tab. 1. The basic characteristics detailed gravimetric survey for conditions of flat country

Scale of gravimetric cards and diagrams	Section of isolines [mGal]	Root-mean-square errors of definition		Step *h* of measurements along of profiles [m]	Distance between profiless [m]
		Heights [m]	Coordinates [m]		
1:50000	0.50	0.70	40	100…500	(3…5)*h*
1:50000	0.25	0.35	40	50…250	(3…5)*h*
1:25000	0.26	0.35	20	50…250	(3…5)*h*
1:25000	0.20	0.25	20	20…100	(3…5)*h*
1:10000	0.20	0.20	4	20…100	(3…5)*h*
1:10000	0.10	0.10	4	10…50	(3...5)*h*

At detailed survey the network consists of parallel profiles, distance between which in (3..5) times more step on a profile. In this connection the accuracy of study of an abnormal field on profile is higher, than on interprofiles section.

Thus, by results of gravimetric survey two-dimensional array of the gravity measuring information can be generated. This array is constructed in fixation to coordinates of points of a surface of the Earth, in which these data were received. In this case two-dimensional correlation of anomalies of acceleration of gravity on a surface of the Earth also take account. The crimp have casual not correlated character (different noise and casual indignation) or character of periodic vibrations. These vibrations have one-dimensional correlation along a line of moving gravimeter and mobile basis. Two-dimensional filtration is possible of effectively to separate of useful signal from crimp handicapes in generated two-dimensional array of the gravity measuring information.

Methods, known from digital image filtration, can be used for formation of amplitude-frequency response of the two-dimensional filter (Gonsales, Woods, 2005; Adaptive Filters, 1988). The amplitude-frequency response so that maximum to keep the useful information on fine details of an arrangement of anomalies of acceleration of gravity on a surface of the Earth. Simultaneously periodic crimp effectively deleted. The frequence of this crimp corresponded to certain local sites of amplitude-frequency response of two-dimensional digital filter. As the consequence, accuracy of the gravity measuring information is raises.

For researches the results of gravity measurements on range by the size 650x650 km with a step 2.5...5.0 angular minutes on a longitude and latitude are used (Bezvesilnaya, 2001). The given method of a filtration has excluded many errors from the gravity measuring information. These errors are caused: forward vibrating accelerations with prevailling frequency 3140 radian/sec; angular vibrating accelerations with prevailling frequency 20 radian/sec, which is equal to frequency of own fluctuations of gravimeter (most dangerous case of the main resonance); angular vibrating accelerations with prevailling frequency 40 radian/sec and 60 radian/sec; angular vibrating acceleration with frequency 6.7 and 10 radian/sec (harmonic fluctuation). Also level of casual noises and disturbances which run on gravimeter has decreased. The accuracy of the gravity measuring information on anomalies of acceleration of gravitation has increased on (20...25) % in comparison with an one-dimensional way of a filtration.

The compression of measuring information can be applied in this gravimeter. It ensures more effective storage of such information in memory of the digital computing device. The compression is fulfilled by the following method:

1. The two-dimensional array of digital references of gravimetric measuring information is formed. Thus the digital references of a gravimetric measuring information note in this array in fixation to coordinates of points on a surface of the Earth.
2. Fulfil a low-frequency filtration of gravimetric measuring information. Thus take into account singularities of frequency spectra of a useful signal and errors (Fig. 2). In an outcome of a filtration from measuring information the errors are eliminated.
3. Fulfil compression of a two-dimensional array of digital references of a gravimetric measuring information with the help of one of methods of compression of two-dimensional digital arrays (videoimages). The methods based on wavelets and fractals (Walstead, 2003) are most effective in this case. Thus the parameters of a method of compression select by such, what the distortions of a measuring information did not exceed a error of measurements. This error included error of a measurement of acceleration of gravity, errors of a measurement of a height and navigational parameters.

The gravimetric measuring information is submitted as sequence of digital references. These references characterize size of acceleration of gravity in certain points of a surface of the Earth. A latitude and longitude of these points will derivate two-dimensional space. Therefore from references the two-dimensional array of the gravimetric measuring information can be generated. Volume of this array can be very large. Therefore actual there is a compression of such information. It also is influenced by limited volume of storage devices for accumulation and storage
of the gravimetric measuring information.

The compression of the gravimetric measuring information provides compact storage of this information. Thus the conditions are observed:

– maintenance of specific accuracy of representation of this information at a minimum allowed degree of compression;
– or maintenance of a specific degree of compression of this information at minimum allowed(permissible) accuracy of representation.

In a method of compression the low-frequency filtration of the gravimetric measuring information is executed. The basis of such filtration is difference in spectral density of a useful signal and handicapes (Fig. 2). In an outcome of a filtration initial errors of the measuring information essentially decrease. The transformed constituent of an error also decreases. She is stipulated by presence of a set of computing operations in a method of compression. In an outcome the tolerance by the methodical constituent of an error stipulated by application of the algorithm of compression with an exclusion of a part of the information can be increased.

The increase of a degree of compression of the gravimetric measuring information also is provided because of applications of effective methods of compression of two-dimensional arrays of the information because of fractals. Such approach for the information on objects of a natural origin especially is effective. It concerns also gravimetric measuring information. Thus the parameters of a method of compression are selected so that the errors of the gravimetric measuring information after compression have not exceeded specific values.

5. CONCLUSIONS

In gravimeter the algorithmic handling of a measuring information allows to separate a useful signal of acceleration of gravity from errors. These errors stipulated vertical acceleration, forward and angular vibrations of the plane, on which is installed gravimeter. Thus, in an output signal of gravimeter a series of errors of measurements completely is compensated. The exactitude of measurements of acceleration of gravity makes 1 mGal.

REFERENCES

1. **Адаптивные фильтры** (1988): *Пер. с англ.* / Под ред. К.Ф. Коуэна и П.М, Гранта. – М.: Мир.
2. **Безвесільна О.М.** (2001), *Вимірювання прискорень: Підручник*. – К.: Либідь.
3. **Гольденберг Л.М., Матюшкин Б.Д., Поляк М.Н.** (1990), *Цифровая обработка сигналов: Учебное пособие для вузов.* – М.: Радио и связь.
4. **Гонсалес Р., Вудс Р.** (2005), *Цифровая обработка изображений.* – М.: Техносфера.
5. **Инструкция по гравиметрической разведке** (1980). – М.: Недра.
6. **Костицын В.И.** (1989), М*етоды и задачи детальной гравиразведки.* – Иркутск: Иркутский ун-т.
7. **Маловичко А.К., Костицын В.И.** (1992), *Гравиразведка: Учебник для вузов.* - М.: Недра.
8. **Маловичко А.К., Костицын В.И., Тарунина О.Л.** (1989), *Детальная гравиразведка на нефть и газ.* – М.: Недра.
9. **Одинцов А.А.** (1982), *Динамически настраиваемые гироскопы*: Учебное пособие. – К.: КПИ.
10. **Павловский В.А.** (1986), *Теория гироскопов*. – К.: Вища школа.
11. **Самотокин Б.Б., Мелешко В.В., Степанковский Ю.В.** (1986), *Навигационные приборы и системы.* – К.: Вища школа.
12. **Уэлстид С.** (2003), *Фракталы и вейвлеты для сжатия изображений в действии*. – М.: Триумф.

COMPUTER-AIDED METHOD OF DIAGNOSTICS OF GAS TURBINE BLADES

Mariusz BOGDAN*, Józef BŁACHNIO*, Marcin DERLATKA*

*Białystok Technical University, Faculty of Mechanical Engineering, 15-351 Białystok, Poland

m.bogan@pb.edu.pl, jozef.blachnio@itwl.pl, mder@pb.edu.pl

Abstract: The article presents a computer-aided method of diagnostics of gas turbine blades with use of artificial neural networks. The subject of presentation is the developed neural network, with help of which – on the basis of features of blade surface images – realised is determination of their condition (operable element – inoperable element). Basing on conclusions formulated on the basis of microstructure examinations and concerning evaluation of state of overheating (blades suitable and not suitable for further operation), as patterns assumed were surface images representing blades in various states (neural pattern classification). Additionally, combining and segregating (according to their applicability for the network teaching process) image parameters, acquired from histograms as well as from matrix of events, automated and increased was the credibility (computer aiding) of decision process. The application of artificial neural network enables better representation of complex relations between blade image and its condition, than in the case of subjective methods used currently by diagnosticians.

1. INTRODUCTION

Selection of material for gas turbine blade of required resistance must consider the spectrum of coercion in the zone of influence of maximum exhaust gas temperature. Frequent cause of damage to gas turbine is overheating of material as well as thermal fatigue of blades of nozzle unit and rotor caused by both excessive temperature and time of its action as well as chemical activity of exhaust gas. During the entire period of operation observed is change in colour of surface of blade feathers. Colour changes resulted from various degree of material overheating. Defects resulting from overheating of blade material lead to faulty operation of gas turbine. This type of defect is repaired always in the course of engine general overhaul. As for today, the decision about necessity of engine repair is taken by a diagnostician, who, using the visual method with help of a videoscope, can diagnose the condition of hardly-accessible elements of turbine. The evaluation of condition is realised on the basis of recorded image of surface of diagnosed element and comparison of this image with pattern images of suitable and unsuitable surfaces of similar elements of turbine blades. Such criteria of evaluation are very imprecise, because the vision of a diagnostician (organoleptic method of evaluation) causes deformation of blade diagnostics results due to subjectivism of examination. Additionally, the colour is a physicopsychological phenomenon, what causes that the evaluation of blade condition made by a diagnostician can be crippled with great error. Until now there is no objective and fully credible method of non-destructive detection of overheating of gas turbine blades. Application of digital technology of image recording combined with computer analysis and computer-aided decision making (neural networks) will contribute to increase of objectivism and credibility of diagnostics of these turbine elements. As for possibilities of diagnostics of blade condition on the basis of image of its surface, i.e. on the basis of parameters determined from histogram (information about lightness) and matrix of events (information about texture – repeatability of pattern on surface of blades), various technical conditions of blades can be correlated with information contained in recorded digital images. For defined technical condition blade surfaces have similar colour and roughness (texture). On the basis of parameters determined from histogram and matrix of events, and with help of neural network (pattern classification) will be possible to assign the blade image (recorded surface) to certain class representing given state (operable, inoperable).

2. ACQUISITION OF IMAGES OF GAS TURBINE BLADES

The subject of examinations are new blades (annealed in five values of temperature close to working temperatures – alloy EI-867 WD – blades of gas turbine rotor of an aircraft turbojet engine) as well as used ones (alloy ŻS-6K – blades of gas turbine stator ring of an aircraft turbojet engine). Acquisition of images was realised at special laboratory stand with help of digital camera and industrial videoscope; guaranteed was also proper repeatability and quality of surface images (Bogdan, 2008). Next, carried out were metallographic examinations aimed at determination of technical condition of examined turbine element. Considered were parameters of microstructure, i.e. change in thickness of aluminium protective coating and change in average size of precipitations of γ' (phase reinforcing the alloy, which mainly determines creep-resistance properties) (Błachnio, 2009). This allowed systematisation of blades according to their technical condition. Fig. 1 shows an example of assumed classification of blades in various technical condition (material criterion).

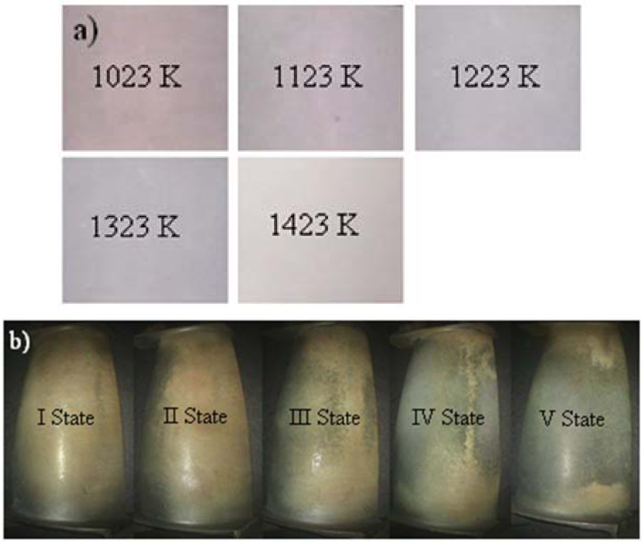

Fig. 1. Acquisition of image of blade surface: a) annealed – with help of digital camera), b) used – with help of videoscope

As a result of influence of high temperatures occurs change of structure of superalloys. Modification of microstructure is simultaneously accompanied by change of coating roughness. The state of coating has influence on reflection and absorption of light stream. Utilised are relations between wave properties of light and physicochemical properties of examined surfaces, which determine angle relations between falling and reflected light as well as absorption of individual wavelengths of electromagnetic radiation spectrum. Additionally, on the basis of examination of chemical composition we have discovered that as a result of influence of high temperatures modified was the weight concentration of elements forming the coating.

3. NEURAL NETWORKS

The assessment of the value of classification error (or classification adequacy) is realised on the basis of simulation of test data set in a previously trained network. Additionally, for the test data set the real classification is already known. This allows to compare decision made by modelled network with real classification and to find out, whether, and to which extent the neural network appropriately anticipates adherence to certain class (group). Overall error rate is defined as the relation (Osowski, 1996):

$$\varepsilon_{ov} = \frac{n_{bl}}{n_{test}}, \tag{1}$$

where: n_{bl} – number of incorrectly classified test data, n_{test} – total number of test data. The measure of classification adequacy (accuracy, efficiency) is defined as the supplement to one of overall classification error:

$$\eta_{ov} = 1 - \varepsilon_{ov} = 1 - \frac{n_{bl}}{n_{test}} = \frac{n_{popr}}{n_{test}}, \tag{2}$$

These measures are alternatively presented in percent on a 100-percent scale. The bigger η_{ov} (the smaller ε_{ov}) the more effective is classification made by „trained" network. At present available are many models of supervised networks, although they are actually variants or modifications of limited number of models. Considered were only those, which gave best results (verification of classification adequacy on a test data set) i.e. the multilayer perceptron (MLP) and the network with radial basis functions (RBF). Exemplary structures of these networks are shown in Fig. 2.

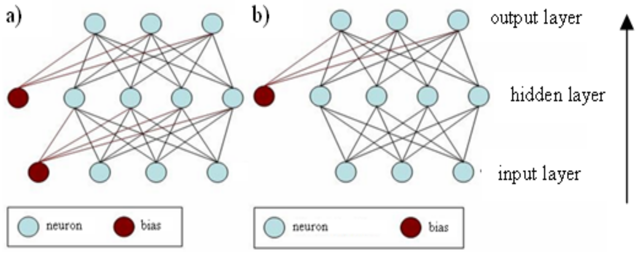

Fig. 2. Scheme of network structure (Zieliński and Strzelecki, 2002): a) multilayer perceptron; b) network with radial basis functions

Number of hidden layers can be virtually arbitrary, however it was proved that two layers are quite sufficient for any mapping of input data into output data. Learning of this type of networks is realised usually with help of a teacher, with first- or second-order gradient method, through minimization of error function. In the case of a multilayer perceptron the level of neuron excitation is the weighted sum of inputs (plus the threshold value added as so-called bias). Introduction of an additional bias input to the neuron causes that the network has increased ability (capability) of learning, what is connected with possibility of shifting of activation threshold depending on weight of bias. In a network with radial basis functions bias is connected only with neurons in output layer. Moreover, this type of network makes use of radial basis functions and has usually one hidden layer containing neurons with radial function of activation. Output neurons are usually the weighted sum of signals send by radial neurons of hidden layer. Learning of this type of network consists in selection of weights of output layer and parameters of Gauss radial functions (Zieliński and Strzelecki, 2002).

4. DIAGNOSTICS OF BLADE CONDITION ON THE BASIC OF PATTERN CLASSIFICATION WITH HELP OF NEURAL NETWORKS

Having tested at least a few computer programs for building and modelling of neural networks we have chosen the program STATISTICA 8 – Data Miner (Bogdan, 2008). This choice allowed us to obtain better, more accurate and more repeatable results. The task of developed neural classifier was elaboration of the method (computer-aided), which enables determination of blade condition on the basis of image (its properties) of its surface. Considered was the following case i.e. two-state classification (new annealed blades and used blades): class 1 – operable state (non-overheated blade), class 2 – inoperable state (overheated blade). The first stage was acquisition of data, which were later used for modelling of the network (input data) and its testing (examination of ability of correct classification). To reduce information size, coloured images were transformed to monochromatic images (8-bit grey-scale 0-255). Next, selected were 10 input parameters (image properties). First six parameters (P1-P6) describe the histogram, or distribution of brightness of pixels for examined image fragments. Next four parameters (P7-P10) were determined from the matrix of events (for the distance equal to 1 and angle 0º) – table 1 (Zieliński and Strzelecki, 2002).

Tab. 1. Input data – vector of properties

Designation	Description	Designation	Description
P1	value of maximum saturation	P6	histogram excess
P2	value of average brightness	P7	contrast
P3	variation of bright-ness distribution	P8	correlation
P4	histogram skewness	P9	energy
P5	histogram kurtosis	P10	homogeneity

Thanks to metallographic examination (material criterion) we hale discovered that new blades annealed at 1023K and 1123K have correct structure, and annealed at 1323K and 1423 – overheated structure. However, in the case of used blades, blades in state I and II have correct structure; and blades in state IV i V – overheated structure. This classification allowed modelling of the network with STATISTICA program. The stages of modelling were as follows:

– Standardisation of data and encoding of inputs (classes);
– Division of data into learning sample and test sample (ratio 50% : 50%);
– Adjustment of parameters of neural network creator, e.g.: minimum and maximum number of hidden layers (for MLP and RBF), types of activation functions for hidden neurons as well as for output neurons (for MLP), minimum and maximum weight reduction for hidden neurons and output neurons (for MLP).

The network was learned with the set of input data due to small number of surface images, without current verification of learning progress with help of the validation set. As a result of simulation in learning as well as in testing mode we obtained optimum models of neural networks (see table 2) for the case No. 1 (two-state classification of annealed blades).

Tab. 2. Models of networks for the problem of two-state classification (diagnostics) of annealed blades

Network No.	Network name	Quality (learning)	Quality (testing)	Learning algorithm	Error function	Activation (hidden)	Activation (output)
1	RBF 10-6-2	88,9	94,4	RBFT	SOS	Gauss	Linear
2	MLP 10-9-2	94,4	88,9	BFGS 24	SOS	Exponential	Exponential
3	MLP 10-7-2	100	88,9	BFGS 25	SOS	Exponential	Logistic
4	MLP 10-15-2	94,4	88,9	BFGS 24	SOS	Exponential	Exponential

Tab. 3. Models of networks after reduction of input data for the problem of classification (diagnostics) of annealed blades

Network No.	Network name	Quality (learning)	Quality (testing)	Learning algorithm	Error function	Activation (hidden)	Activation (output)
1	MLP 8-10-2	100,0000	94,44444	RBFT	Entropy	Exponential	Softmax
2	MLP 10-9-2	94,4	88,9	BFGS 24	SOS	Exponential	Exponential

Tab. 4. Models of networks for the problem of two-state classification (diagnostics) of operating blades

Network No.	Network name	Quality (learning)	Quality (testing)	Learning algorithm	Error function	Activation (hidden)	Activation (output)
1	MLP 10-7-2	100,0000	100,0000	BFGS 23	Entropy	Tanh	Softmax
2	MLP 10-5-2	100,0000	100,0000	BFGS 21	Entropy	Line	Line
3	MLP 10-10-2	100,0000	100,0000	BFGS 19	SOS	Exponential	Sinus
1	MLP 10-7-2	100,0000	100,0000	BFGS 23	Entropy	Tanh	Softmax

Thick models of neural networks (No. = 2, 3, 4) have relatively high quality (ability) of learning and simultaneously high level of testing quality 89%. However, in two cases a blade in inoperable state was considered as an operable one. Such situation is disadvantageous from the point of view of diagnostics of turbine blade. To eliminate these classification errors we have examined applicability of individual parameters (P1-P10) for differentiation of classes (states). For two classes (groups) of data we have carried out the test, which purpose was the comparison of basic statistics for 10 variables with 18 trials for each class. The data set was arranged in such way, so that each case represents one unit identified with grouping variable (state). On the basis of obtained results we have stated that parameters P3 and P4 are unnecessary, because they do not provide valuable information for the „classification problem". In the table 3 presented are results of modelling of neural networks after reduction of input data.

The ability of restoration of learning set – the measure of retention ability of learning data amounts in this case to 100%, however, the ability of generation of correct solutions for data contained in testing set, on which the network was not trained (measure of generalization ability) amounts to 94% .The same method of creation of models of neural networks was applied for used blades. In the table 4 presented are some neural networks – for input data obtained from blade surface images recorded with an American videoscope.

In the case of assessment of condition of used blades with help of neural classification we hale obtained network models (No. = 1-3), which learn and map classes correctly – three types of network have made no mistakes during testing.

5. SUMMARY

On the basis of obtained results it was stated that neural networks are valuable tool for assessment of blade condition both new (annealed) and used ones (tab. 3, 4). Developed neural classification model (network of certain architecture) enables assessment of blade condition on the basis of properties (parameters) of its image with satisfactory credibility. Additional advantage of this type of approach is the possibility of full automation of diagnostic process in operational conditions (without disassembly of the turbine), i.e. the image of surface of examined turbine element acquired with videoscope is transferred to the computer, where, with help of suitable software, recognized are its properties, and on this basis the „modelled network" (correctly trained) correctly determines technical condition of the blade.

REFERENCES

1. **Błachnio J.** (2009), The effect of high temperature on the degradation of heat-resistant and high-temperature alloys, *Solid State Phenomena*, Vol. 147-149, 744-752.
2. **Bogdan M.** (2008), An attempt of evaluation of overheating of gas turbine blades, *Journal of Polish CIMAC – Diagnosis, reliability and safety*, 3(1), 25-32.
3. **Osowski S.** (1996), *Algorithms of neural network*, Warsaw.
4. **Zieliński K. W., Strzelecki M.** (2002), *Computer analysis of biomedical images*, Warsaw.
5. www.statsoft.pl – User's manual of Statistica 8.

A METHOD OF RELIABILITY CHARACTERISTICS ESTIMATION ON THE BASIS OF ADJUSTMENT AND DIAGNOSTIC INFORMATION

Henryk BOROWCZYK[*], Paweł LINDSTEDT[*], Janusz MAGIER[**]

[*]Białystok Technical University, Wiejska 45c, 15-333 Bialystok, Poland
[*]Air Force Institute of Technology, Ks. Boleslawa 6, 01-494 Warsaw, Poland

borowczyk@post.pl, p.lindsted@pb.edu.pl, janusz.magier@gmail.com

Abstract: The paper presents innovative method of reliability characteristics estimation on the basis of symptoms of parametric and temporary defects (prior to occurrence of catastrophic defects). The method is based on evident relations between adjustment, diagnostics and reliability, which are observed in an organised system of utilisation of each complex technical object.

1. INTRODUCTION

During operation of expensive and complex technical objects (aircraft, aircraft engines) grows importance of their maintenance comprehended as optimum actions within the frames of their adjustment, diagnostics and reliability examination (Bobrowski, 1985; Boliński and Stelmaszczyk, 1981; Borgoń et al., 1998; Lindstedt 2002; 2009; Żurek, 2001).

In operational practice observed is frequently following chain of events:

– adjustment actions are caused by wear of components of a technical object, or in other words by change of technical condition, thus the adjustment is combined in natural way with diagnostics;
– wear of elements of the object leads to occurrence of various defects in various time periods, which form the base for determination of reliability indexes, thus the reliability is directly combined with diagnostics.

In the maintenance of technical objects important is preservation of proper relations between adjustment, diagnostics and reliability with consideration of the fact that the adjustment and the diagnostics are based on determined functions and the reliability – on probabilistic functions.

The reliability examinations can be carried out individually for each technical object in its environment on the basis of information about all maintenance actions carried out on the object. The possibility of determination of individual reliability characteristics on the basis of functional and diagnostic information can be particularly important for cases, when the set of objects is small and their environment very diversified.

2. DEFECTS AS A BASE OF RELIABILITY CHARACTERISTICS

In the course of reliability examinations great role play comprehensive examinations of occurrence of various accidental defects. The defect changes the reliability state, which is quantitatively described by reliability indexes.

In the process of determination of reliability of a technical object considered are various types of defects: catastrophic (total), parametric (ageing, partial), and temporary (Bobrowski, 1985; Borgoń et al., 1998; Sotskow, 1973; Zamojski, 1981).

These defects have various forms and various mechanism of formation, therefore during reliability examinations defects identification is the substantial problem.

Catastrophic (total) defects are sudden events leading to the catastrophe or total inoperability of the technical object. These defects are unambiguous and evident, therefore easy to identification and must be considered arbitrarily in the process of calculation of reliability indexes.

The parametric defect (partial, ageing, degradation) is an event, which gradually leads to the inoperability state of the object. In given moment of operation this defect does not cause inoperability of the object and is only a premise to occurrence of the state of inoperability in the future. The identification of a parametric damage is difficult and requires special measurement systems applied for assessment of the system operation and for diagnostic examinations (Borgoń et al., 1998; Lewitowicz and Kustroń, 2002; Lindstedt et al., 2003). These defects should be considered in calculation of reliability indexes.

The temporary defect is an event, which appears randomly and after a certain period disappears automatically without leaving unambiguous evidence of its occurrence. Identification of temporary defects is very difficult and requires diagnostic examinations. These defects should be used for calculation of reliability indexes.

During calculation of reliability indexes determination of probability of operability R(t) is necessary. These calculations should consider three basic types of defects (catastrophic, parametric and temporary). In analysis of reliability we assume that occurring defects are independent events (Sotskow, 1973) and in this case:

$$R(t) = f\left(R_a(t), R_b(t), R_c(t)\right) \tag{1}$$

where: $R_a(t)$ – probability of correct operation in view to catastrophic defect, $R_b(t)$ – probability of correct operation in view to parametric defect, $R_c(t)$ - probability of correct operation in view to temporary defect.

In the process of operation the maintenance crew tries to prevent appearance of catastrophic defects ($R_a(t)=1$), then:

$$R(t) = f\left(R_b(t), R_c(t)\right) \tag{2}$$

It is observed that during operation and maintenance (adjustment and diagnostics) it is possible to determine symptoms of parametric (b) and momentary (c) defects, what enables determination of estimators of reliability characteristics $R_b^*(t_i)$ and $R_c^*(t_i)$. Then we have:

$$R(t) = f\left(R_b^*(t), R_c^*(t)\right) \tag{3}$$

From the physical description of parametric defects results that they are relevant to the technical condition of the object and, temporary defects are relevant to the state of adjustment of the object.

Hence changes of technical condition (technical potential) exceeding assumed threshold can be considered as symptoms of parametric defects, and changes of state of adjustment (adjustment potential) exceeding assumed threshold – as symptoms of temporary defects.

3. ADJUSTMENT AND TECHNICAL POTENTIALS OF AN OBJECT

An object must be correctly adjusted. Required is proper relation between utility (functional) signals U_O and signals D_K resulting from the technical condition of the machine. This relation can be described with state equation (Lindstedt et al., 2005; Lindstedt, 2009; Söderström and Stoica, 1997):

$$\frac{dU_O}{d\Theta} = a_{R_C} U_O + b_K D_K \tag{4}$$

where: U_O – complex signal of operational adjustment (environment); D_K – complex diagnostic signal; a_{Rc} – parameter of state of adjustment (adjustment potential); b_K – parameter of intensity of effect of technical condition on possibility of adjustment.

Complex signals resulting from functioning of the object in the environment U_O and complex signals resulting from changes of technical condition D_K in the environment U_O can be determined from the following relations (Lindstedt et al., 2003; 2005; Lindstedt and Magier, 2004; Lindstedt, 2009):

$$U_O = \sqrt{N_{U1}^2 + N_{U2}^2 + N_{U3}^2 + \ldots.} \quad ; \qquad D_K = \sqrt{N_{D1}^2 + N_{D2}^2 + N_{D3}^2 + \ldots} \tag{5}$$

Where N_U with relevant index refers to number of operational thresholds exceeding for all signals of environment, and N_D with relevant index refers to number of exceeding of operability thresholds for all diagnostic signals. The method of reduction of the course of any signals to numbers of exceeding of relevant thresholds is shown in Lindstedt et al. (2003; 2005); Lindstedt and Magier (2004); Lindstedt (2009):

Current value of state of adjustment a_{Rc} can be determined from following relation resulting from the state equation (4):

$$a_{Rc} = \frac{\Delta U_0}{\Delta\Theta\left(U_0 + \hat{a}_{Rc} D_K\right)} \quad where \quad \hat{a}_{Rc} = -\frac{b_K}{a_{Rc}} = \frac{\sum U_{Oi} D_{Ki}}{\sum D_K{}^2} \tag{6}$$

Changes of the parameter a_R can be considered as symptoms of temporary defects.

The object must be in proper technical condition. Required is proper relation between diagnostic signals D_K resulting from the technical condition of the object and environment signals U_O. We can formulate following state equation (Lindsted et al., 2005; Lindstedt, 2009; Söderström and Stoica, 1997):

$$\frac{dD_K}{d\Theta} = a_{Rb} D_K + b_U U_O \tag{7}$$

where: a_{Rb} – parameter of technical condition (technical potential); b_U – parameter of intensity of effect of operation on technical condition.

Current value of technical condition can be determined using the relation resulting from the state equation (7):

$$a_{Rb} = \frac{\Delta D_K}{\Delta\Theta\left(D_K + \hat{a}_{Rb} U_O\right)} \quad \text{where } \hat{a}_{Rb} = -\frac{b_U}{a_{Rb}} = \frac{\sum D_{Ki} U_{Oi}}{\sum U_{Oi}{}^2} \tag{8}$$

It is assumed that:

- exceeding by the parameter of technical potential a_{Rb} its standard deviation by 1/2σ can be considered as occurrence of a symptom of parametric defect, which allows determination of estimators of parametric defects $R_b^*(t_i)$.
- exceeding by the parameter of adjustment potential a_{Rc} its standard deviation by 1/2σ can be considered as occurrence of a symptom of temporary defect, which allows determination of estimators of temporary defects $R_c^*(t_i)$;

Above assumptions are basis for reliability characteristics estimation:

$$R_b^*(t_i) = \frac{n_b - m_b(t_i)}{n_b} \tag{9}$$

where: $m_b(t_i)$ – number of parametric defects in time interval $[0, t_i]$; n_b – number of parametric defects in object life-time.

$$R_c^*(t_i) = \frac{n_c - m_c(t_i)}{n_c} \tag{10}$$

where: $m_c(t)$ – number of temporary defects in time interval $[0, t_i]$; n_c – number of temporary defects in object life-time.

4. ESTIMATION OF RELIABILITY CHARACTERISTICS OF RR ALLISON 250 TURBO-SHAFT ENGINE BEARING UNIT (AN EXAMPLE)

The bearing unit (Fig. 1) consists of eight bearings installed in engine supports and one bearing installed inside the wheel driving the reduction gear (Lindstedt et al., 2003).

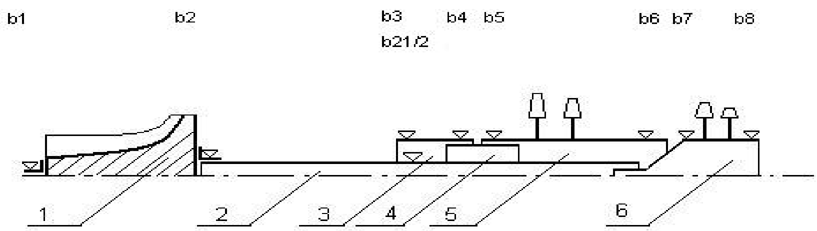

Fig. 1. Bearing unit of the RR Allison 250 turbo-shaft engine (1 – compressor, 2, 3, 4 – shaft, 5 – low pressure turbine, 6 – high pressure turbine, b1 – b8 – bearings)

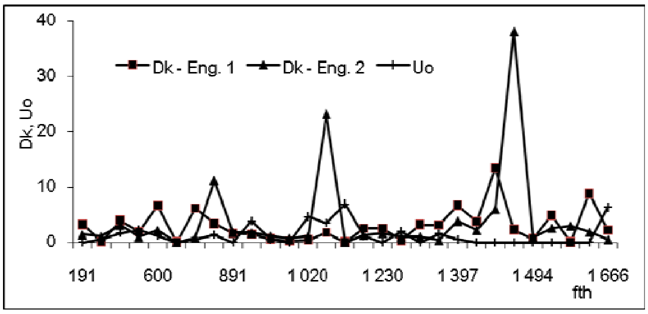

Fig. 2. Complex diagnostics of bearing unit of the Allison 250C20B engines No. 1 and 2 on the basis of normalised numbers of exceeding of threshold values of diagnostic signals

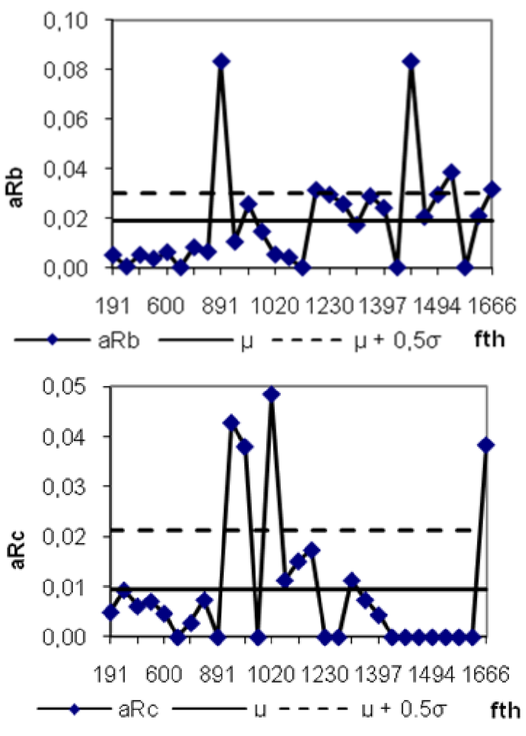

Fig. 3. Changes of parameters a_{Rb} and a_{Rc} vs. flight time – engine No. 1

The bearing unit operates in unfriendly environment of other engine subassemblies, which are represented by the complex signal U_O. Its technical condition changes continuously, generating partial diagnostic signals reduced to the complex diagnostic signal D_K.

Results of operational examination of engines 1 and 2 are presented in Lindstedt et al. (2003, 2005); Lindstedt and Magier (2004). Acquired signals are of various physical nature. They are reduced to universal form, i.e. to number of exceeding of diagnostic thresholds of these signals.

Results of examinations after reduction to numbers of threshold exceeding and complex signals U_O and D_K are shown in Fig. 2.

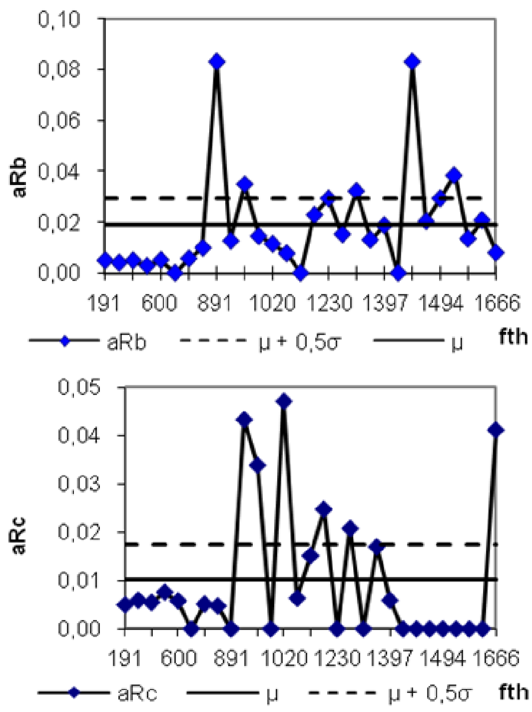

Fig. 4. Changes of parameters a_{Rb} and a_{Rc} vs. flight time – engine No. 2

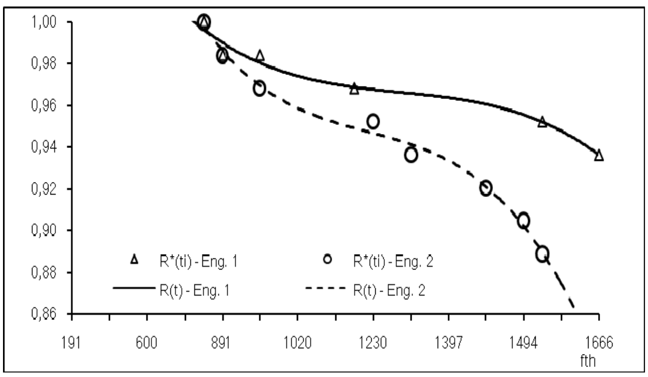

Fig. 5. Reliability characteristics for engines RR Allison 250 No. 1 and No. 2

On the basis of results presented in Fig. 2, and using formulas (6) as well as (8) determined were curves of adjustment potential a_{Rc} and technical potential a_{Rb} of the unit – Fig. 3.

Estimators $R_c^*(t_i)$ i $R_b^*(t_i)$ and corresponding reliability functions $R(t)$ for engines 1 and 2 are shown in Fig. 5.

Fig. 5 shows reliability characteristics for engines 1 and 2. It is easy to see that they differ markedly. Hence expected time of failure-free operation of each engines will be different.

5. SUMMARY

The basis of proper operation of complex technical object is the suitable knowledge about its operational condition (automatics), technical condition (diagnostics) and state of reliability (theory of reliability). It has been found that the observation of changes of parameters of operational condition and technical condition can form the basis for determination of symptoms of parametric and momentary defects, and hence – corresponding reliability estimators, and finally – specific reliability characteristic.

Presented method is characterised with the fact that the reliability characteristic can be determined prior to occurrence of dangerous catastrophic defects for each single object.

REFERENCES

1. **Bobrowski D.** (1985), *Models and mathematic methods in the theory of reliability*, WNT, Warsaw.
2. **Boliński B., Stelmaszczyk Z.** (1981), *Utilisation of turbine engines*, WKŁ, Warsaw.
3. **Borgoń J., Jaźwiński J., Klimaszewski S., Żmudziński Z., Żurek J.** (1998), *Simulation methods of examination of flight safety*, Ed. ASKON Warsaw.
4. **Lewitowicz J., Kustroń K.** (2003), *Introduction to utilisation of airships*, Vol. 2. Ed. ITWL, Warsaw.
5. **Lindstedt P.** (2002), *Practical diagnostics of machines and its theoretical background*, Scientific Ed. ASKON Warsaw.
6. **Lindstedt P.** (2009), The method of complex worthiness assessment of an engineering object in the process of its use and service, *Solid State Phenomena*, Vol 144, 45÷52, TransTech Publications, Switzerland.
7. **Lindstedt P., Borowczyk H., Magier J.** (2003), Examination of possibilities of complex diagnostics of a bearing system on the basis of information acquired from functional, tribologic and vibroacoustic methods, *Research project KBN No. 5T12D01122*, Report ITWL No. 1371/50, Ed. ITWL Warsaw.
8. **Lindstedt P., Borowczyk H., Magier J.**(2005), Controlling of operation of turbine helicopter engine on the basis of complex diagnostic signals and environment signals, *8th International Conference AIRDIAG 2005*, Ed. ITWL Warsaw.
9. **Lindstedt P., Magier J.** (2004), Premises of normalisation and scaling of threshold values of diagnostic and environment signals for a bearing unit of a helicopter turbine engine, *Prace Naukowe ITW*L Zeszyt 18, Ed. ITWL Warsaw.
10. **Söderström T., Stoica P.** (1997), Identification of systems, PWN, Warsaw.
11. **Sotskow B. S.** (1973), *Reliability of elements and devices in automatics*, WNT Warsaw.
12. **Zamojski W.** (1981), *Reliability and utilisation of systems*, Ed. Wrocław TU, Wrocław.
13. **Żurek J.** (2001), Introduction to safety problems in aviation, *WLOP Review* 12/2001, Ed. EMPA Poznań.

RESEARCH OF BASE AND ALLOYED OIL MC-20 INFLUENCE ON THE TRIBOTECHNICAL CHARACTERISTICS OF ROLLER BEARINGS

**Sergey G. CHULKIN[*], Aleksandr D. BREKI[*], Irina V. SOLOVIOVA[*], Mikhail M. RADKEVICH[***]

[*]29 Polytechnicheskaya st. St. Petersburg, 195251 Russia The 1-st Building, 408

uwc99@mail.ru, albreki@yandex.ru, solovjeva_irina_@list.ru, radmich@mail.ru

Abstract: This article is devoted to research of the influence of an oil additive "serpentinite" on to roller bearings friction behavior. In this article the influence of the additive «serpentinite» on the roller bearings (208 series) friction behaviour is considered. It has been established that the serpentinite addition to the oil MC-20 allowed to reduce friction losses at the start-up of the mechanism 15-20% in comparison with the base oil.

1. INTRODUCTION

The questions, related to the definition of friction losses in roller bearings determined by the content and properties of the lubrication oils, are interesting to many branches of modern machine-building industry. It is known (Garkunov, 1985), that in roller bearings we can see the following types of losses as losses due to elastic hysteresis in contact zones of rolling elements with the running path of the rings, rubbing friction losses between rolling elements and separator, bearing races and separator (for several types of the bearings). Friction losses also appear between roller's end-faces and thrust surface of the inner ring (for roller radial-axial bearings), on the contact areas that appear due to the difference in instantaneous speed of the rings and rolling elements (Rozenberg, 1970) (so called „differential friction"), and also spinning of the balls. Special case is the case with friction losses in the lubricating material. This lubricating material fills the separator sockets, contact areas and working elements of the bearings. In this situation there is an overcoming of hydraulic friction.

Lubricants, used for roller bearings lubrication, have different antifriction properties and reduce friction losses to different extents. Friction losses differ in the case of various concentrations of additives in alloyed oils. Due to the appearance of new oils and lubricant compositions on the market there is a necessity to study their influence on the tribotechnical properties of the roller bearings.

2. RESEARCH METHODOLOGY

Investigations of the lubricant materials' influence on the tribotechnical properties of the roller bearings were carried out in the Department of "Machine Science and Machine Parts" on the experimental unit DM-28M (Fig. 1).

The unit makes it possible to determine the static friction characteristics and carry out tests within the following range of shaft speed: $0 < n \leq 800$rpm and the following total bearings load: $0N < F \leq 800$N. The tests of 208 series radial ball bearings with dynamic load rating of C=32000N and static load rating of C_o=17800N in the ranges of shaft speed and total bearings load mentioned below are still being carried out. The lubrication is performed at the normal oil level (center of the lower rolling element)

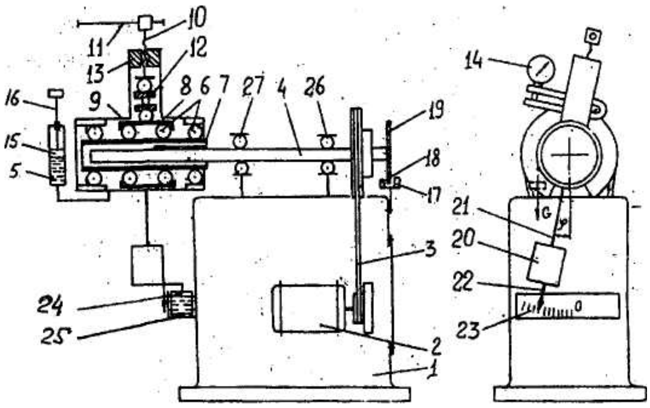

Fig. 1. Scheme of DM-28M unit: 1 – molded case, 2 – elektromotor, 3 – drive belting, 4 – shaft, 5 – oil reservoir, 6 – tested bearings, 7 –common liner. 8 – sleeve, 9 – housing, 10 – loading screw, 11 – tap wrench, 12 – dynamometer, 13 – nut, 14 – indicator, 15 – piston, 16 – screw, 17 – photoresistor, 18 – electric lamp, 19 – disk, 20 – load, 21 – rod, 22 – hand (arrow), 23 – moment scale, 24 – blade, 25 – oil sump

During the experimental part of the research, according to scale 23 the friction torque values are defined $T_{q,i,j}$, q=1,2,3,…,p (p – tests repeat number while the shaft speed and load values are fixed) at various values of total load F_j, j=1,2,3,…,m (m – quantity of the loads, equal to the quantity of trial runs) and shaft speed n_i, i=1,2,3,…, k (k – quantity of speed shaft values during the one trial run). One test run is carried out at fixed values of F_j and k different values of the shaft speed. At each value of shaft speed p values of friction torque $T_{q,i,j}$, are defined. Before the beginning of the trial run with number j, temperature measurement of the lubricating composition is carried out – $\tau j(^0C)$, and after finishing the trial run the realization time is fixed – t_j(min).

As a result, moment matrix, temperature and time values and all initial data are given in Tab. 1.

Tab. 1. The results of trial run # j

$n(rpm)$	n_1	n_2	…	…	n_{i-1}	n_i	…	n_k
$\tau_j(^0C)$	$F_j = N$, $j = 1, 2, 3, \ldots, m$						$t_j(\min)$	
$T(N\cdot mm)$	$T_{1,1,j}$	$T_{1,2,j}$	…	…	$T_{1,i-1,j}$	$T_{1,i,j}$	…	$T_{1,k,j}$
	…	…	…	…	…	…	…	…
	$T_{p,1,j}$	$T_{p,2,j}$	…	…	$T_{p,i-1,j}$	$T_{p,i,j}$	…	$T_{p,k,j}$
$F_{mp}(N)$	$F_{1,1,j}$	$F_{1,2,j}$	…	…	$F_{1,i-1,j}$	$F_{1,i,j}$	…	$F_{1,k,j}$
	…	…	…	…	…	…	…	…
	$F_{p,1,j}$	$F_{p,2,j}$	…	…	$F_{p,i-1,j}$	$F_{p,i,j}$	…	$F_{p,k,j}$
f	$f_{1,1,j}$	$f_{1,2,j}$	…	…	$f_{1,i-1,j}$	$f_{1,i,j}$	…	$f_{1,k,j}$
	…	…	…	…	…	…	…	…
	$f_{p,1,j}$	$f_{p,2,j}$	…	…	$f_{p,i-1,j}$	$f_{p,i,j}$	…	$f_{p,k,j}$

3. PROCESSING OF RESEARCH RESULTS

After completing the experimental part of the work the reduced factors and friction forces in the tested bearings are defined in accordance to $T_{q,i,j}$, F_j and n_i. In the roller bearings friction forces are reduced to inner diameter of the bearing. Superficial (reduced) friction factor:

$$f = \frac{F_{mp}}{F_n} \tag{1}$$

where: F_{mp} – friction force (N), reduced to inner diameter of the bearing, F_n – the force (N), acting on the bearing. Taking into consideration the fact that $T_n=F_{mp}\cdot d/2$, (1) can be written down in the following way:

$$f = \frac{2\cdot T_n}{d\cdot F_n} \tag{2}$$

where: T_n – bearing friction torque (Nmm), d – inner diameter of the bearing (mm).

In unit DM-28M all the bearings are symmetrically located with respect to the force application plane. In this connection, disregarding the item's dead weight, it can be considered that each of them is loaded with force

$$F_n = 0,5\cdot F \tag{3}$$

where F – axial force on the screw. The friction torque of the bearing T_n is connected with the friction torque T, which was measured by scale 23 using the relation:

$$T_n = 0,25\cdot T \tag{4}$$

Using equations (3) and (4), formula (2) can be written as follows:

$$f = \frac{T}{d\cdot F} \tag{5}$$

As $F_{mp}=f\cdot F$, then taking into consideration (5), the reduced friction force can be shown in the following way:

$$F_{mp} = \frac{T}{d} \tag{6}$$

Using the moment matrix that corresponds to the trial run # j, taking into consideration (6) the reduced friction forces matrix can be found. The matrix will correspond to the same trial run:

$$\begin{pmatrix} T_{1,1,j} & T_{1,2,j} & \ldots & T_{1,k,j} \\ \ldots & \ldots & \ldots & \ldots \\ T_{p,1,j} & T_{p,2,j} & \ldots & T_{p,k,j} \end{pmatrix} \cdot d^{-1} = \begin{pmatrix} F_{1,1,j} & F_{1,2,j} & \ldots & F_{1,k,j} \\ \ldots & \ldots & \ldots & \ldots \\ F_{p,1,j} & F_{p,2,j} & \ldots & F_{p,k,j} \end{pmatrix} \tag{7}$$

Using the relations (7) and (5) the superficial friction factors matrix in the trial run # j can be found from the equation:

$$\begin{pmatrix} F_{1,1,j} & F_{1,2,j} & \ldots & F_{1,k,j} \\ \ldots & \ldots & \ldots & \ldots \\ \mathrm{F}_{p,1,j} & \mathrm{F}_{p,2j} & \ldots & \mathrm{F}_{p,k,j} \end{pmatrix} \times F_j^{-1} = \begin{pmatrix} f_{1,1,j} & f_{1,2,j} & \ldots & f_{1,k,j} \\ \ldots & \ldots & \ldots & \ldots \\ \mathrm{f}_{p,1,j} & \mathrm{f}_{p,2,j} & \ldots & \mathrm{f}_{p,k,j} \end{pmatrix} \tag{8}$$

The elements of resulting matrixes are brought under the related cells of the above table.

As a matter of table records, it is possible to settle the dependence (function) of friction force and friction factor from the shaft speed and total bearing load: $f=g(F)$, $f=s(n)$, $F_{mp}=p(F)$, $F_{mp}=q(n)$. These dependences are showed up and compared for different lubricating materials.

4. THE PURSUANCE OF THE RESEARCH

On the basis of the methodology, investigations researches of the lubricant materials' influence on the tribotechnical properties of the roller bearings (208 series) were carried out.

There were trial runs of base oil MC – 20 and oil MC – 20 with addition of 1% geomodifier of the serpentinite fine particles with the average size $d\approx 0,6$µm in submicron content. The quantity of the normal loads and the quantity of test runs were selected as m=16.

Normal bearing loads were selected as the type of monotonically increasing sequence:

$$\{F_j \mid j = 1,2,\ldots,16\} =$$
$$\{125\mathrm{N},250\mathrm{N},500\mathrm{N},\ldots 6000\mathrm{N},7000\mathrm{N},8000\mathrm{N}\}$$

Load change from 500N to 6000N was carried out with the step of 500N.

The quantity of speed shaft values during one test run was taken as k=8. Selected shaft speeds were placed as the type of monotonically increasing sequence:

$$\{n_i \mid i = 1,2,\ldots,8\} =$$
$$\{0\mathrm{rpm},100\mathrm{rpm},150\mathrm{rpm},\ldots,400\mathrm{rpm}\}$$

Shaft speed change from 100(rpm) to 400(rpm) was carried out with the step of 50(rpm). The quantity of test repeats at fixed shaft speed and fixed normal bearing load was taken as p=10.

On the basis of the data o resulting from 32 preliminary test runs of the base oil MC-20 and oil MC-20 with geomodifier, dependences of the reduced friction force and superficial friction factor from normal bearing load at fixed values of shaft speed were established.

In particular, at static friction, alloyed oil MC-20 on the interval has better antifriction impact on the elements of the system DM-28M than base oil (Figure 2).

At fixed values of shaft speed n_i=50·(i+1) (rpm), (i=1,2,3,…,7), dependences of reduced friction force and superficial (reduced) friction factor from normal bearing load (Figure 3, Figure 4) were found. After than comparison it can be said that in the case of friction, base oil MC-20 has the best antifriction properties.

After an increase of the shaft speed there is a corresponding increase of reduced friction force and superficial (reduced) friction factor in the whole selected load range. The given consistent pattern is the characteristic of the system with base oil as well as with alloyed oil.

In the Cartesian coordinate system (Figure 3), on each straight line $F=F_j$ there are 70 experimentally obtained points $\{(F_j;\ F_{g,i,j})|\ q=1,2,\ldots,10;\ i=1,2,\ldots,7;\ j=\text{const}\}$. The number of all points, which are indicated in the Cartesian coordinate system, is 1120. There is overlapping of the points in each „vertical row” (Figure 3, Figure 4). It means that the same events appear in identical conditions as well as in various conditions.

5. CONCLUSIONS

1. The developed methodology allows us to carry out investigations of the lubricant materials influence of on the tribotechnical characteristics of ball and roller bea-rings from normal loading on the radial bearings (208 series) at its lubrication with the base and alloyed oil MC-20 that reduce friction losses per 15–20% in com-parison with base oil, but at dynamic friction – the base oil MC-20 has the best antifriction properties.
2. On the average, while the loading is fixed, with an increase of the shaft speed - the reduced friction force increases faster with the use of alloyed oil MC-20.
3. With the increase of shaft speed, rate of increase of the reduced friction force is decreased on the whole load range for the same oil.
4. The dependences of superficial (reduced) friction factors on the load significantly differ on the interval $F \in [250\text{N}, 2500\text{N}]$ at base oil as well as at alloyed oil MC-20.
5. The values of superficial (reduced) friction factors at identical values of the normal bearing load and shaft speed differ by the small quantity for the base and alloyed oil MC-20.
6. The obtained graphs have local maximums and minimums, flexible points that need to be additionally explained.
7. It is necessary to continue investigations at the used set of conditions for preparing the statistics.

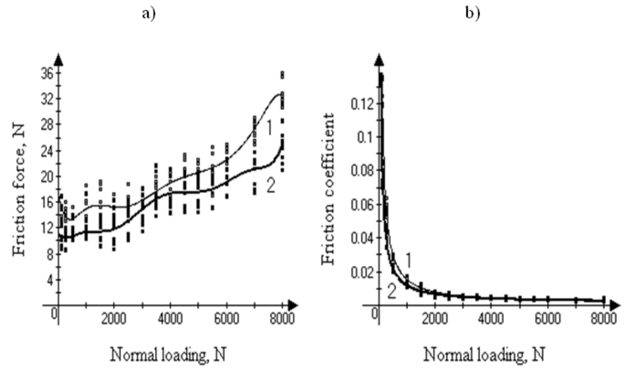

Fig. 2. Dependences of friction force (a) and superficial friction factor (b) from normal bearing load for base (1) and alloyed (2) oil MC-20 at static friction

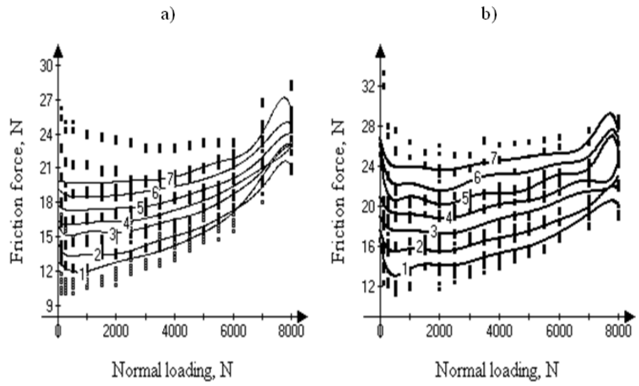

Fig. 3. Dependences of friction force from normal bearing loading at fixed values of shaft speed (1 – 100 rpm, 2 – 150 rpm, 3 – 200 rpm, 4 – 250 rpm, 5 – 300 rpm, 6 – 350 rpm, 7 – 400 rpm): a) based oil MC-20; b) alloyed oil MC-20

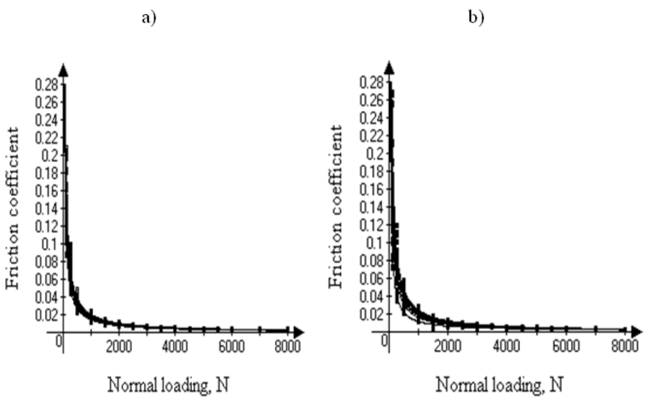

Fig. 4. Dependences of superficial (reduced) friction factor from normal bearing loading at fixed values of shaft speed: a) base oil MC-20; b) alloyed oil MC-20.

REFERENCES

1. **Garkunov D. N.** (1985), *Tribotechnique*, Machine Building, Moscow.
2. **Rozenberg Yu. A.** (1970), T*he influence of lubricating oils on the life time and reliability of machine components*, Machine Building, Moscow.

FRACTURE TOUGHNESS OF 19Mn5 STEEL PIPE WELDED JOINTS MATERIALS

Mykolas DAUNYS*, Povilas KRASAUSKAS*, Romualdas DUNDULIS*

Machine Design Department, Kaunas University of Technology, Kęstučio 27, LT-44021 Kaunas, Lithuania

Mykolas.Daunys@ktu.lt, Povilas.Krasauskas@ktu.lt, Romualdas.Dundulis@ktu.lt

Abstract: This paper presents an investigation of Ignalina NPP reactor’s main circulated circuit (MCC) pipeline welded joints materials fracture toughness properties. Standard compact C(T)-1T specimens containing “V” and “K” – type welds were cut off from the various MCC pipe’s zones, produced from the 19Mn5 steel pipe and welded by electrodes UTP-068HH, YONI-13/55 and CT-36. Critical J – integraf J_{Ic} values were defined Rusing *J–R* curve test method, which results on determination of J – integral values as a function of crack extension Δa. The investigation enables to calculate critical crack length Δa_{max} and Δa_c sizes and J – integral J_{Ic}, J_{max} and J_{Pmax} values, which are used to predict safe service lifetime of the cracked pipelines.

1. INTRODUCTION

The elements of the nuclear power plant (NPP) pipelines, also heavy loaded parts of other NPP structures (e.g. turbine rotors, its blades), during turbine start up, power download, testing or overloads during emergency situations, stresses and strains reaches its dangerous values, in some cases exceed limited ones.

The overloads in stress concentration zones, cracked parts or welded joints calls stress concentration, which cause crack origination and fatigue its growth and are one of the reasons of structure fracture. In order to examine lifetime of the repaired pipes welded zones it is necessary to know static and cyclic characteristics of the materials.

The inspection of the pipelines during exploitation by using nondestructive control methods has showed presence of crack type damages in the welded joints and its surrounding zones. According to the requirements of reactor technological regulation, cracks in the welded joints of the reactor’s main circulated circuit are unallowable, so in the case of one’s detection, it should be repaired until crack sizes reach dangerous values.

In order to evaluate the forecast of such situation, it is necessary to dispose of material fracture toughness characteristics, which are used for evaluating pipe material resistance to the crack propagation.

The pipelines of the main circulated circuit were produced from the low carbon steel 19Mn5 with diameter of Ø630 mm and wall thickness of 27mm and welded using pearlite structured electrodes YONI-13/45 and YONI-13/55 or high Ni concentration alloyed electrodes UTP-068HH and CT-36, thus the goal of our investigation was focused on definition of the fracture toughness criterion *J* – integral J_{Ic} for these MCC pipeline welded joints.

2. SPECIMENS AND TESTING TECHNIQUE

Chemical composition of tested materials is presented in Table 1, mechanical characteristics – in Table 2.

Investigation of fracture toughness criterion *J* – integral has been carried out on the standard compact C(T)-1T specimens (Fig. 1) cut off from the pipe’s welded zones with various welds configuration.

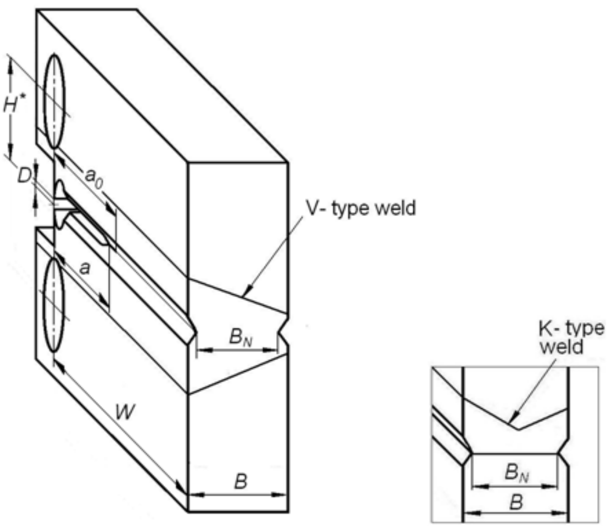

Fig. 1. Shape and dimensions of compact specimen with “V” and “K” - type welds

In fours specimens with “V” – type weld were cut off from 19Mn5 steel pipe welded by electrodes CT-36 and YONI-13/55, two specimens containing “V”– type weld and three specimens containing “K” – type weld we cut off from the pipe’s joint produced from 19Mn5 steel pipe welded by electrodes UTP-068HH (Tab. 3). The last ones were used to evaluate heat affected zone influence on crack resistance and fracture J – integral value.

In total, 13 specimens were tested to evaluate fracture characteristics of the MCC pipeline welded joints. Such selection of the weld types allowed evaluation fracture properties in the welds metal and in the joint heat affected zone as well.

Testing of the specimens has been performed at ambient temperature on the 50 kN capacity low cycle tension-compression testing machine according to the requirements presented in the standard ASTM E1820–08 (ASTM E1820-08). Testing machine drive during specimen reloading was controlled by high speed X-Y recorder.

According to the requirements (ASTM E1820-08), the specimens were precracked on a high frequency hydraulic testing machine keeping the ratio a/W (crack length vs width of the specimen) in the limits of $0.48\leq a/W\leq 0.73$ (Tab. 3).

When the sharp fatigue cracks were done, in order to maintain brittle crack growth, in the forecast crack propagation plane, on both sides of the specimen were made grooves in depth of 2 mm (Fig. 1).

Measurements of the specimens and precracking data are presented in Table 3.

Tab. 1. Chemical composition of 19Mn5 steel pipe and weld metals

Material	Amount of elements in %								
	C	Si	Mn	S	P	Cr	Ni	Mo	Addition
19Mn5	0.220	0.39	1.23	0.003	0.007	0.30	0.22	-	Cu 0.067
UTP-068HH	0.023	0.37	4.70	0.006	0.009	18.8	70.45	0.67	Fe 2.93; Cu 0.01; Ti 0.07; Co 0.01; Al 0.01; Nb 1.95
YONI-13/55	0.093	0.39	0.85	0.090	0.030	-	-	-	-
CT-36	0.051	0.10	7.96	0.005	0.005	-	61.2	6.16	Ti<0.1

Tab. 2. Mechanical characteristics of 19Mn5 steel pipe and weld metals

Material	Yield strength $R_{p0.2}$, MPa	Ultimate strength R_m, MPa	Reduction of cross-section area Z, %	Elongation A, %	Young's modulus $E\times10^5$, MPa	Energy density a_H, J/cm^2
19Mn5 steel pipe	490	600	78.5	-	1.9	-
Weld metal UTP-068HH	408	685	40.7	44.0	-	-
Weld metal YONI-13/55	364	577	-	28.3	-	24.9
Weld metal CT-36	311	595	-	28.2	-	18.7

Tab. 3. Measurements and precracking data of the specimens

Specimen Nº	W, mm	B, mm	B_N, mm	a_0, mm	a_0/W
Weld metal CT-36 "V"- type weld					
1	24.75	20.75	50.00	27.65	0.553
2	24.35	20.35	50.35	30.82	0.6121
3	24.35	20.35	50.35	27.44	0.545
4	24.85	20.85	50.10	25.69	0.513
Weld metal YONI-13/55 "V"- type weld					
1	24.75	20.75	50.25	25.53	0.508
2	24.35	20.35	49.88	28.50	0.571
3	24.74	20.74	49.60	27.30	0.550
4	24.4	20.48	49.35	25.92	0.525
Weld metal UTP-68HH "V"- type weld					
1	24.75	20.75	50.20	30.79	0.613
2	24.90	20.90	50.05	36.71	0.733
Weld metal UTP-68HH "K"- type weld (HAZ)					
1	25.20	21.20	50.05	24.00	0.480
2	25.21	21.21	50.0	31.90	0.638
3	25.20	21.20	50.05	25.48	0.509

3. INVESTIGATION OF 19Mn5 STEEL PIPE WELDED JOINTS FRACTURE TOUGHNESS

Fracture criterion for 19Mn5 steel pipes welded joints was taken J–integral and its critical value J_{Ic}, because definition of this criterion less depends on the sizes of the specimen to be tested. Procedure of J_{Ic} calculation is described in the Anderson (1991) and ASTM E1820-08 (2008).

Critical J–integral J_{Ic} values were defined using J–R curve method, which results on developing curve of J–integral values at evenly spaced crack extensions Δa. Initial data for developing of J–R curve is "force vs. load line displacement" (F–δ) records. Monotonously increasing reloading force, by the means of high speed X-Y recorder and computer via oscilloscope, these records were given in a form as shown in Fig. 2.

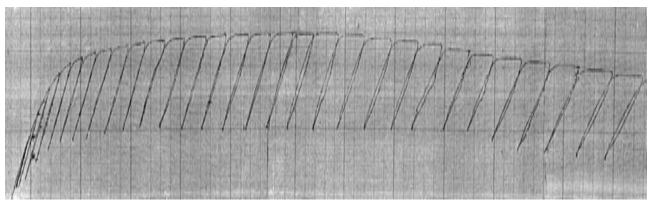

Fig. 2. Example of (F–δ) curve record

Recorded (F–δ) segments were used to calculate the increment of a crack length and corresponding to it J–integral values. Crack increment was calculated using elastic compliance method from loading/unloading segments unloading part compliance ($C_i = \delta_i/F_i$) change, current J–integral values and J_{Ic} was calculated according to ASTM E1820-08, (2008).

It should be noted that compliance calculation is a very sensitive process, because the angles of the adjacent se-gments, from which the compliance tilt is calculated differs in a very negligible margin. Moreover, as showed our experiment, compliance change during specimen loading/unloading was not enough stable process in that viewpoint, because especially in the initial stage of reloading, there was observed considerable compliance scatter, which may be the reason of saltatory crack grow with following its slow up in the next loading step. For this reason we had considerable difficulty in finding calculated compliance value, which results on J–integral calculation.

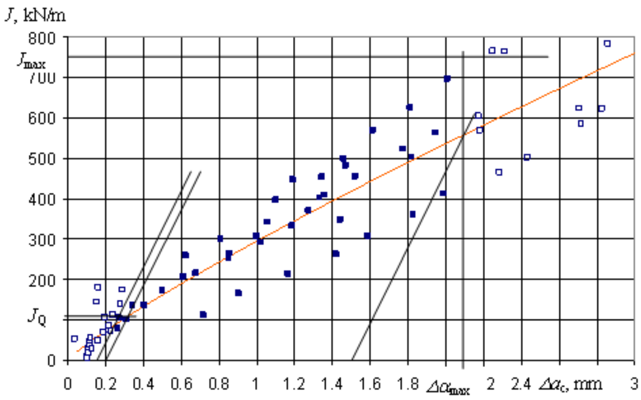

Fig. 3. Experimental fracture toughness data for “V”– type weld specimens welded by electrodes CT-36 and averaged J–R curve (line)

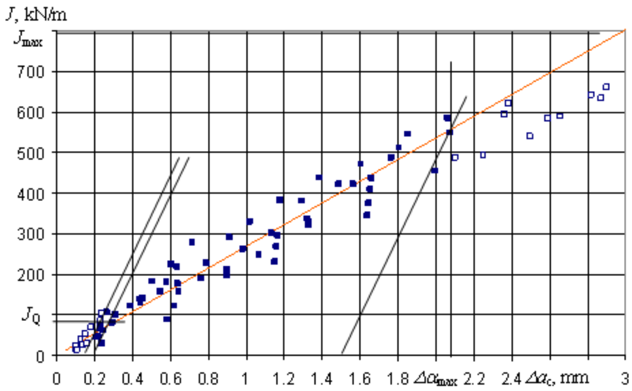

Fig. 4. Experimental fracture toughness data for “V” – type weld specimens welded by electrodes YONI-13/55 and averaged J–R curve (line)

According to the testing programme, for each specimen in series J–integral values J_i and crack extension Δa_i were calculated and then J_i– Δa_i curve were plotted. The results of these calculations are presented in Figs. 3 – 6. According to (ASTM E1820-08, 2008), J–R curves were established by smoothly fitting points to a power law regression line expressed as follows:

$$J = c_1\left(\Delta a_{\mathrm{p}}\right)^{c_2} \tag{1}$$

where c_1 and c_2 are the parameters of the equation of the region, limited by the given J_{max} and Δa_{max} and the exclusion line (2) derived from the point Δa_p=0.15mm.

$$J = 2\sigma_{\mathrm{Y}}\Delta a_{\mathrm{p}}\,, \tag{2}$$

where σ_{Y} is effective yieldstrength $\left[\sigma_{\mathrm{Y}} = \left(R_{\mathrm{p}0.2} + R_{\mathrm{m}}\right)/2\right]$.

The maximum crack extension capacity was calculated by the equation

$$\Delta a_{\max} = 0.1 b_0 \tag{3}$$

Following to the recommendations of (ASTM E1820-08, 2008) were defined the parameters J_{Q}, $J_{\max}$ and $J_{\max}$, which allow to evaluate stable (J_{Q} =J_{Ic}), maximal ($J_{\max}$) and critical (J_{Pmax}) crack growth. The J–integral value J_{Q} was defined at the intersection between the J–R curve (Eq. 1) and the exclusion line (Eq. 2), derived from the point Δa_{p}=0.20mm.

If calculated J_{Q} values satisfied condition $b_0 \geq (25J_{\mathrm{Q}}/\sigma_{\mathrm{Y}})=B^*$, it was assumed that J_{Q} =J_{Ic}.

As was noted before, the testing of welded specimens was characterized by the considerable scatter of the experimental results, thus thereafter J_{Ic} values were averaged of all tested specimens in each series.

Results of J–integral calculation are presented in Tab. 4.

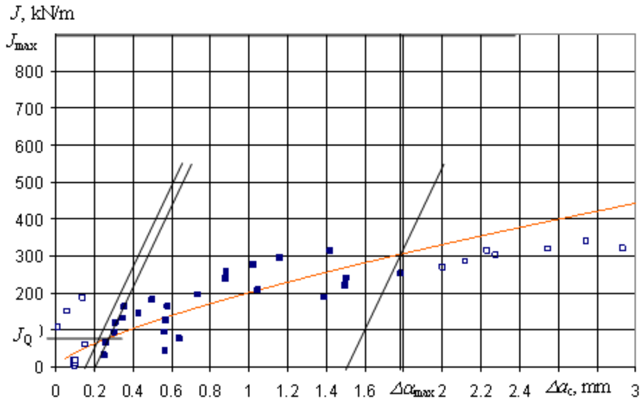

Fig. 5. Experimental fracture toughness data for “V”– type weld specimens welded by electrodes UTP-068HH and averaged J–R curve (line)

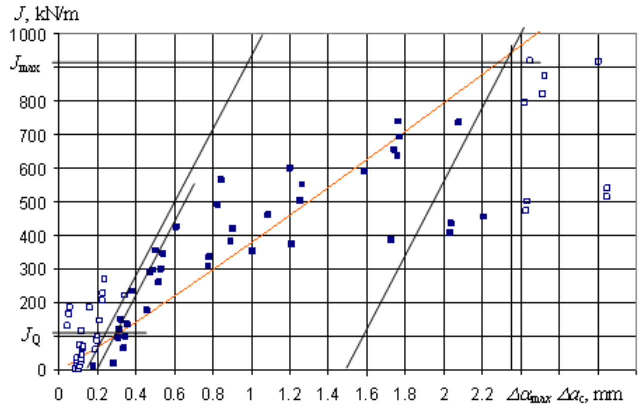

Fig. 6. Experimental fracture toughness data for “K”– type weld specimens (HAZ) welded by electrodes UTP-068HH and averaged J–R curve (line)

Tab. 4. Results of J integral calculation

Weld material	$\Delta a_{\max}$, mm	J_{Ic}, kN/m	$J_{\max}$, kN/m	J_{Pmax}, kN/m
CT-36	2.09	108	742	606
YONI-13/55	2.08	79	791	481
UTP-068HH “V”- type weld	1.78	101	902	146
UTP-068HH “K”- type weld	2.34	100	918	643

The analysis of the results presented in Table 4 has showed that highest J_{Ic} values was given for the welds using electrodes CT-36, for which J–integral critical value comprises J_{Ic}=108kN/m, lower J_{Ic} values was given for the specimens welded using the electrodes UTP-068HH (J_{Ic}=101kN/m) and lowest J_{Ic} ones was given for the specimens welded using electrodes YONI-13/55, for which J–integral critical value J_{Ic} was given 79 kN/m.

The best resistance to the crack propagation at maximal load $P_{\max}$ was given for the specimens UTP-068HH with "K"-type weld ($J_{P\max}$=643kN/m), i.e. in the case, when a crack start and grow in the heat affected zone.

From the other side, comparison of the specimens with "K" and "V" – type welds has showed that resistance to the crack propagation in the heat affected zones is similar to the crack growth resistance in the weld zone and crack growth does not depends on weld type: for the specimens with "K" – type weld there was found J_{Ic}=101kN/m and for the specimens with "V"-type weld J_{Ic} comprise 100kN/m. These results have showed that crack growth in the heat affected zone is the same like in the weld metal.

Summarising it could be concluded, that 19Mn5 steel pipe welded by electrodes CT-36 have better resistance to crack growth than joints welded by electrodes YONI-13/55 and UTP-068HH, thus in the case of a cracked main circulated circuit (MCC) pipeline repair, advantage should be taken to electrodes CT-36 in comparison with electrodes UTP-068HH and YONI-13/55.

Furthermore J–R calculation data was used to define critical stress intensity factors range K_c^*, which was defined using maximal load P_c value taken from the graphs (F–δ) (Daunys et al., 2005). This criterion represents fracture characteristic for the specimens of tested thickness (GOST 25.506-85, 1985).

Because the thickness of tested specimens in our experiment is near to the pipe thickness, given K_c^* values could be used to evaluate fracture toughness of the MCC pipeline from the positions of linear fracture mechanics as well. Comparison of stress intensity factor K_c^* range, calculated from (F–δ) curves and J_{Ic} values, obtained from the experiment have showed satisfactory correlation (Table 5).

Tab. 5. Weld material fracture toughness characteristics

Weld metal	K_c^*, MPa m$^{1/2}$	J_{Ic}, kN/m
CT-36 "V"- type weld	114,9	108
YONI 13/55 "V"- type weld	134,5	100
UTP-068HH "V"- type weld	91,7	79
UTP-068HH HAZ ("K"- type weld)	116,9	101

4. CONCLUSIONS

1. Fracture toughness investigation of 19Mn5 steel pipe welded joints used in Ignalina NPP has showed that in the case of cracked MCC pipeline repair, advantage should be taken to the electrodes CT-36 in comparison with the electrodes YONI-13/55 and UTP-068HH; however difference to the crack resistance is quite negligible. It means that for the pipeline repair could be used all three types of electrodes as well.
2. For qualitative crack growth evaluation in the welds using electrodes CT-36, should be used J–integral critical value J_{Ic}=108kN/m, for the welds using electrodes UTP-068HH – J_{Ic}=101kN/m and for the welds using electrodes YONI-13/55 J_{Ic}=79kN/m.
3. For calculated maximum crack extension Δa_{max} the maximal J–integral value was given for the joints welded using electrodes UTP-068HH and comprises J_{max}=902 – 918MPa in comparison with J_{max}=791MPa for the joints welded using electrodes CT-36 and J_{max}=742MPa for electrodes YONI-13/55.
4. The best resistance to the crack propagation at maximal load $P_{\max}$ was given for the specimens in the heat affected zone (UTP-068HH "K"-type weld), for which was given $J_{P\max}$=643 kN/m.
5. Comparison of the specimens with "K" and "V" – type welds using electrodes UTP-068HH has showed that resistance to crack propagation in the heat affected zone is similar to crack growth resistance in the weld, therefore it could be concluded that fracture toughness for this weld material does not depends on weld type.

REFERENCES

1. **Anderson T. L.** (1991), *Fracture Mechanics. Fundamentals and Applications*, CRC Press, Boca Raton, Ann Arbor, Boston.
2. **Daunys M., Krasauskas P., Dundulis R.** (2005), Fracture Toughness of Welded Joints Materials for Main Pipelines at Ignalina NPP, *Nuclear Engineering and Design,* Elsevier, Lausanne, Vol. 235, Issue 7, 747-760.
3. Mechanical test methods of metals. Determination of fracture toughness characteristics under static loading (in Russian), GOST 25.506-85, (1985).
4. Standard Test Method for Measurement of Fracture Toughness, ASTM E1820-08, (2008).

SYNTHESIS AND SENSITIVITY OF MULTIAXIAL DRIVE SYSTEMS

Tomasz DZITKOWSKI[*], Andrzej DYMAREK[*]

[*]Institute of Engineering Processes Automation and Integrated Manufacturing Systems,
Silesian University of Technology, ul. Konarskiego 18a, 44-100 Gliwice, Poland

tomasz.dzitkowski@polsl.pl, andrzej.dymarek@polsl.pl

Abstract: The selection of the dynamical properties of machines is one of the methods enhancing their durability and reliability. Such task may be accomplished with the use of the analysis and synthesis algorithm. Accordingly, the issue of the synthesis, enabling the determination of the parameters and structure of the systems in view of their dynamical characteristics, may be applied as a tool supporting the design process under any operating conditions. The scope of discussion is the mixed method of synthesizing dynamic characteristics enabling the derivation of the parameters and models of drive systems.

1. INTRODUCTION

The determination of such structure of the system and its parameters that meets the requirements concerning the assumed dynamical phenomena is a task inverse to analysis (Świtoński, 2004; Wojnowski et al., 1986), therefore, it is a synthesis (Buchacz et al., 2005; Dymarek, 2000; 2004; Dymarek and Dzitkowski, 2005; Dzitkowski, 2001; 2004; Dzitkowski and Dymarek, 2005; 2006; 2008). Such task may be regarded as a support of the stage of designing mechanical systems, where an essential element is the fulfillment of the required dynamical properties. These properties may be represented in a graphic or analytical form, or in a form of sequential zeros and poles, which shall be considered in the paper.

The scope of discussion is the synthesis of machine drive systems as models of torsional vibrations. Such vibrations are more difficult to detect than flexural ones, which are accompanied by noise and vibrations of the adjacent elements (for example, shaft frames). Due to the absence of symptoms, torsional vibrations are particularly dangerous, as they may be unnoticeable until the destruction of subsystems occurs. Therefore, the determination of basic frequencies of the drive system free vibration is of crucial importance, as it makes it possible to avoid the operation under resonance ranges which may hinder the durability and proper functioning of a machine.

2. THE SYNTHESIS OF TORSIONALLY VIBRATING DISCRETE SYSTEMS WITH BRANCHED STRUCTURE IN THE FORM OF GRAPHS

This paper discusses the mixed method of synthesising dynamic characteristics $U(s)$ – called immobility (combining the continued fraction distribution method – Foster's method with the partial fraction distribution method – Cauer's method). Theoretical details of this method are presented in Buchacz et al. (2005); Dymarek (2000). In this paper, numerical examples of synthesis torsionally vibrating discrete systems with branched structure are provided. The following requirements were subjected to synthesis:

- number of elements $n = 9$;
- furthermore, it was assumed that the resonance zones of the dynamical characteristic of the synthesized systems are in the neighborhood of poles, the values of which are: ω_0=0rad/s, ω_2=10rad/s, ω_4=20rad/s, ω_6=30rad/s, ω_8=40rad/s;
- the anti-resonance zones of the dynamical characteristics of the synthesized systems are in the neighborhood of zeros, the values of the characteristic frequencies are: Ω_1=5rad/s, ω_3=15rad/s, ω_5=25rad/s, ω_7=35rad/s.

Such formulation of the conditions of resonance and anti-resonance zones imply the dynamical rigidity $Z(s)$ of torsionally vibrating mechanical discrete system is given in the form

$$Z(s)=\frac{s^2\left(s^2+10^2\right)\left(s^2+20^2\right)\left(s^2+30^2\right)\left(s^2+40^2\right)}{\left(s^2+5^2\right)\left(s^2+15^2\right)\left(s^2+25^2\right)\left(s^2+35^2\right)} \tag{1}$$

where: $s = \boldsymbol{j}\omega$, $\boldsymbol{j} = \sqrt{-1}$.

After the transformation

$$U(s)=\frac{1}{s}Z(s), \tag{2}$$

the immobility $U(s)$ is given in the form

$$U(s)=H\,\frac{s\left(s^2+10^2\right)\left(s^2+20^2\right)\left(s^2+30^2\right)\left(s^2+40^2\right)}{\left(s^2+5^2\right)\left(s^2+15^2\right)\left(s^2+25^2\right)\left(s^2+35^2\right)}, \tag{3}$$

where: H – any real positive number.

At first immobility (3) is distributed into partial fraction. Consequently

$$\frac{U(s)}{H} = k_\infty s + \frac{B_1}{(s-j5)} + \frac{B_2}{(s+j5)} + \ldots + \frac{B_7}{(s-j35)} + \frac{B_8}{(s+j35)} \tag{4}$$

where: k_∞, B_1, B_2, …, B_7, B_8 – values of residuum pole suitably equal ∞, j^5, $-j^5$, ... , j^{35}, $-j^{35}$.

The residua can be calculated as follows

$$\begin{cases} k_\infty = \lim\limits_{s\to\infty} \dfrac{U(s)}{s} = 1, \\ B_1 = \lim\limits_{s\to j5} (s-j5)U(s), B_2 = \lim\limits_{s\to -j5} (s+j5)U(s), \\ \quad\vdots \\ B_7 = \lim\limits_{s\to j35} (s-j35)U(s), B_8 = \lim\limits_{s\to -j35} (s+j35)U(s). \end{cases} \tag{5}$$

Out of the equations (4) and (5) it is evident that B_1, B_2, …, B_7, B_8 are conjugate numbers, but analyzing the qualities of real positive rational function it is obvious that all residua on the imaginary axis are real and positive i.e.

$$\begin{aligned} &B_1 = B_2 = 134.585, B_3 = B_4 = 126.89, \\ &B_5 = B_6 = 109.585, B_7 = B_8 = 78.55, \end{aligned} \tag{6}$$

so

$$\begin{cases} \dfrac{B_1}{(s-j5)} + \dfrac{B_2}{(s+j5)} = \dfrac{2\cdot 134.585 s}{s^2+5^2}, \\ \dfrac{B_3}{(s-j15)} + \dfrac{B_4}{(s+j15)} = \dfrac{2\cdot 126.89 s}{s^2+15^2}, \\ \dfrac{B_5}{(s-j25)} + \dfrac{B_6}{(s+j25)} = \dfrac{2\cdot 126.89 s}{s^2+25^2} \\ \dfrac{B_{2n-1}}{(s-j35)} + \dfrac{B_{2n}}{(s+j35)} = \dfrac{2\cdot 78.55 s}{s^2+35^2}. \end{cases} \tag{7}$$

Applying the results of (7), equation (4) can be written as

$$\frac{U(s)}{H} = s + \frac{269.17s}{(s^2+5^2)} + \frac{253.78s}{(s^2+15^2)} + \frac{219.95s}{(s^2+25^2)} + \frac{157.1s}{(s^2+35^2)} \tag{8}$$

Equation (8) is presented as the sum of measurable functions in the forms

$$\frac{U(s)}{H} = s + \frac{(522.95s^3 + 66907.75s)}{(s^2+5^2)(s^2+15^2)} + \frac{219.95s}{(s^2+25^2)} + \frac{157.1s}{(s^2+35^2)}, \tag{9}$$

$$\frac{U(s)}{H} = s + \frac{(522.95s^3 + 66907.75s)}{(s^2+5^2)(s^2+15^2)} + \frac{(377.05s^3 + 367626.25s)}{(s^2+25^2)(s^2+35^2)}, \tag{10}$$

$$\frac{U(s)}{H} = s + \frac{(742.9s^4 + 448739s^2 + 43054562.5)}{(s^2+5^2)(s^2+15^2)(s^2+25^2)} + \frac{157.1s}{(s^2+35^2)}, \tag{11}$$

Rational functions in equations (8 ÷ 11) are distributed into continued fraction in the following way:

$$U(s) = J_1 s + \cfrac{1}{\cfrac{s}{c_2} + \cfrac{1}{J_2 s}} + \cfrac{1}{\cfrac{s}{c_3} + \cfrac{1}{J_3 s}} + \cfrac{1}{\cfrac{s}{c_4} + \cfrac{1}{J_4 s}} + \cfrac{1}{\cfrac{s}{c_5} + \cfrac{1}{J_5 s}} \tag{12}$$

$$U(s) = J_1 s + \cfrac{1}{\cfrac{s}{c_2} + \cfrac{1}{J_2 s + \cfrac{1}{\cfrac{s}{c_3} + \cfrac{1}{J_3 s}}}} + \cfrac{1}{\cfrac{s}{c_4} + \cfrac{1}{J_4 s}} + \cfrac{1}{\cfrac{s}{c_5} + \cfrac{1}{J_5 s}} \tag{13}$$

$$U(s) = J_1 s + \cfrac{1}{\cfrac{s}{c_2} + \cfrac{1}{J_2 s + \cfrac{1}{\cfrac{s}{c_3} + \cfrac{1}{J_3 s}}}} + \cfrac{1}{\cfrac{s}{c_4} + \cfrac{1}{J_4 s + \cfrac{1}{\cfrac{s}{c_5} + \cfrac{1}{J_5 s}}}} \tag{14}$$

$$U(s) = J_1 s + \cfrac{1}{\cfrac{s}{c_2} + \cfrac{1}{J_2 s + \cfrac{1}{\cfrac{s}{c_3} + \cfrac{1}{J_3 s + \cfrac{1}{\cfrac{s}{c_4} + \cfrac{1}{J_4 s}}}}}} + \cfrac{1}{\cfrac{s}{c_5} + \cfrac{1}{J_5 s}} \tag{15}$$

where: J_1, J_2, J_3, J_4, J_5 – are the values of the synthesized discrete inertial elements, c_1, c_2, c_3, c_4, c_5 – are the values of the synthesized discrete elastic elements.

The equal equations (12-15) represent the immobility function of the dynamical structures in the form of polar graphs. An example of the graph of the immobility function (14) is shown in Fig. 1.

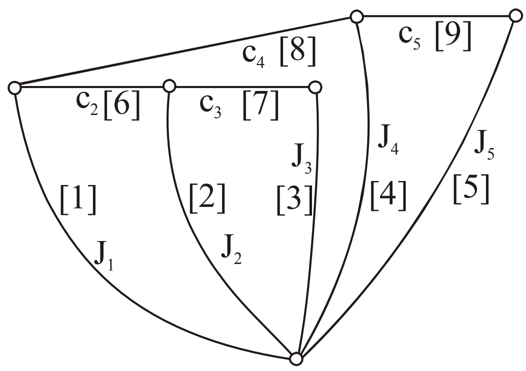

Fig. 1. Polar graph as an illustration of the implementation of equation (14)

The discrete mechanical system the graph of which is presented in Fig. 1 has the form presented in Fig. 2 and its parameters (inertial and elastic) are obtained (see Tab. 1).

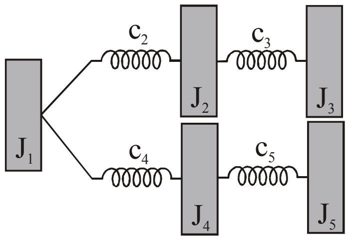

Fig.2. Synthesized mechanical system

Tab. 1. Inertial, elastic parameters of synthesized discrete system

	$(c)_{(i)}$[Nm/rad]	$(J)_{(i)}$[kgm^2]
1	-	1.00
2	522.95	4.28
3	350.71	7.61
4	377.04	0.43
5	43.09	0.05

Numerical calculations of the theoretical analysis are illustrated in Fig. 3.

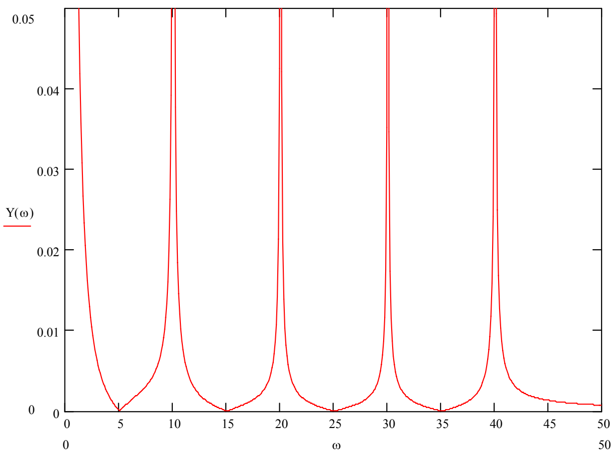

Fig. 3. Diagram of dynamical flexibility of the synthesized system

3. THE SENSITIVITY OF DISCRETE SYSTEMS REPRESENTED BY POLAR GRAPH AND STRUCTURAL NUMBERS

The way of examining the sensitivity of obtained discrete system, with respect to values of received parameters, as results of synthesis - by means the graphs and structural numbers methods - have been presented. Problems of examining the sensitivity in polar graphs categories and the structural numbers in a regard to discrete structures has been introduced in Wojnarowski et al., (1986).

In this paper, it has been show how to nominate the sensitivity function in order to direct flexibility. The examination has been solved with a usage of graphs (Fig. 1) and their connections with structural numbers.

After following calculations, graphical representations of sensitivity function are shown in Figs. 4 ÷ 5.

Analyzing the plots in Figs 4÷5 we can assume that the sections of a highest value of a sensitivity function are covering with the strands of resonance and anti-resonance frequencies of a synthesis structure. We can formulate following notice with the strands of resonance frequencies:

– the width of the resonance strand along the first frequency (10 rad/s) the biggest impact has the parameter J_3;
– comparing the width of an expanse of a sensitivity function along the second frequency (20 rad/s) it can be noticed that the parameter c_2 has a bigger influence on a width resonance section than the other parameters;
– observing the width of a section of a sensitivity function along the third frequency (30 rad/s) we can see that the more important parameters which have an influence on a width of a resonance strand along this frequency are stiffness c_5 and inertia J_5;
– analyzing the width of the section of sensitivity function along which the fourth frequency (40 rad/s) we can notice that the most important parameter which has an impact on the width of this area has a parameter c_4, the other huge impact has the parameter J_4.

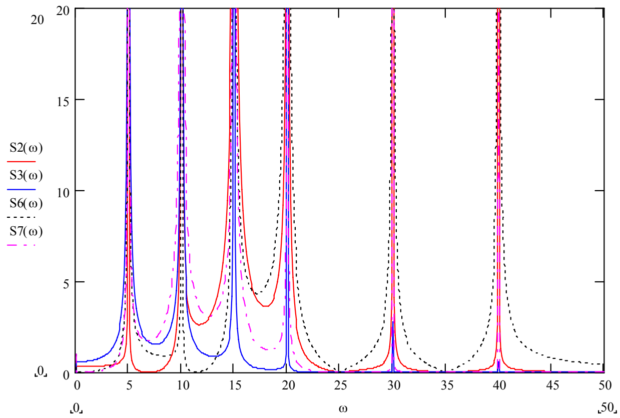

Fig. 4. Comparison of sensitivity function with elements S2(ω) - J2, S3(ω) - J3, S6(ω) - c2, S7(ω) - c3

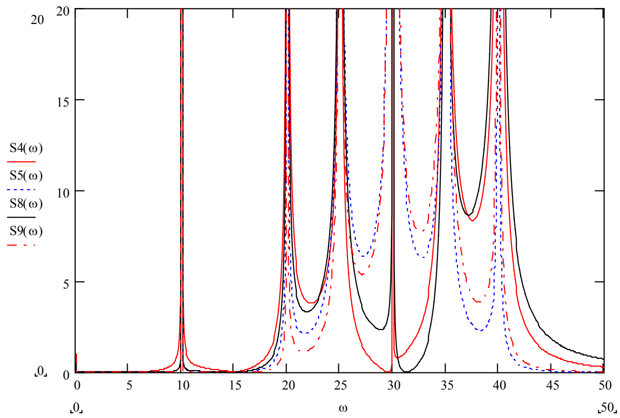

Fig. 5. Comparison of sensitivity function with elements S4(ω) - J4, S5(ω) - J5, S8(ω) - c4, S9(ω) - c5

However, when we compare the plots, which were nominated in order to all elements (see Fig.6) we can formulate following conclusions:

– the most important parameter through others, which has the biggest impact of the sensitivity function of examined structure, is stiffness c_4. This parameter has a huge

impact on the width of resonance strand in order to the fourth frequency (see Fig.7);
– the other huge impact on the width of strand along the frequency has the parameter c_5. This parameter has a huge impact on the width of resonance strand in order to the third frequency.

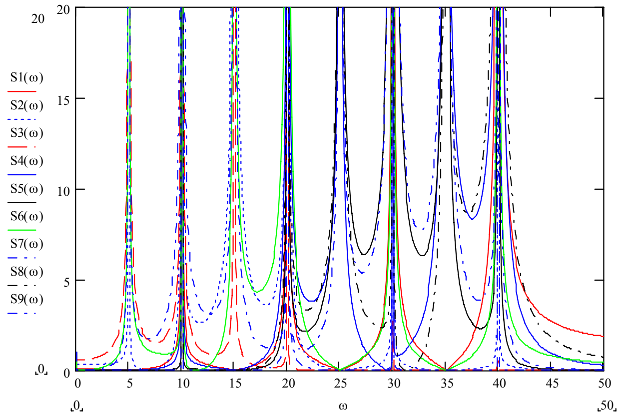

Fig. 6. The summary presentation of sensitivity function of examined mechanical system

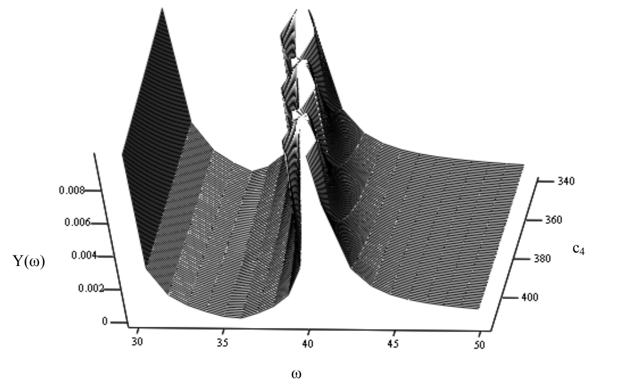

Fig. 7. Diagram of dynamical flexibility versus stiffness coefficient c4 – the increase of resonance zone at the fourth frequency

4. CONCLUSION

The greatest intensity of vibrations might be found in conditions of resonance. They can be avoided due to a proper selection of frequency free vibrations. Such task may be accomplished with the use of the synthesis algorithm.

Exiting the resonance zone is a crucial condition of the machine's work but it does not eliminate entirely the problem of vibrations. The free vibrations frequencies appear in more than one machine. In these cases damping has a decisive role as it lowers the vibration amplitude in a serious way. That is why the paper concerns formulating and solving the problem of synthesis and sensitivity of machine driving systems with and without damping. The method of synthesising and examining sensitivity may influence considerably the research and selection of parameters of the analyzed machine. The derived parameters constitute the bases for further verification of complex models, and a starting point for the optimization.

REFERENCES

1. **Buchacz A., Dymarek A., Dzitkowski T.** (2005), *Design and examining of sensitivity of continuous and discrete- continuous mechanical systems with required frequency spectrum represented by graphs and structural numbers*, Monograph No. 88, Silesian University of Technology Press, Gliwice (in Polish).
2. **Dymarek A., Dzitkowski T.** (2005), Modelling and synthesis of discrete – continuous subsystems of machines with damping, *Journal of Materials Processing Technology*, Vol. 164-165, 1317-1326.
3. **Dymarek A.** (2000), *The reverse task of vibrating mechanical systems with damping represented graphs and structural numbers*, PhD dissertation, Gliwice (in Polish).
4. **Dymarek A.** (2004), The Sensitivity as a Criterion of Synthesis of Discrete Vibrating Fixed Mechanical System, *Journal of Materials Processing Technology*, Vol. 157-158, 138-143.
5. **Dzitkowski T., Dymarek A.** (2008), Design and examining sensitivity of machine driving systems with required frequency spectrum, *Journal of Achievements in Materials and Manufacturing Engineering*, Vol. 26, 49-56.
6. **Dzitkowski T., Dymarek A.** (2006), Synthesis and sensitivity of machine driving systems, *Journal of Achievements in Materials and Manufacturing Engineering*, 20, Gliwice, 359-362.
7. **Dzitkowski T., Dymarek A.** (2005), The synthesis of machine driving systems, *Twelfth International Scientific and Engineering Conference - Machine-Building and Technosphere on the Border of the XXI Century*, Donetsk – Sevastopol, Vol. 5, 66-70.
8. **Dzitkowski T.** (2004), Computer aided synthesis of discrete – continuous subsystems of machines with the assumed frequency spectrum represented by graphs, *Journal of Materials Processing Technology*, Vol. 157-158, 144-149.
9. **Dzitkowski T.** (2001), *The reverse task of dynamics discrete-continuous mechanical systems represented graphs and structural numbers*, PhD dissertation, Gliwice (in Polish).
10. **Świtoński E.** (Ed.) (2004), *The modelling of mechatronic drive systems*, Monograph No. 70, Silesian University of Technology Press, Gliwice (in Polish).
11. **Wojnarowski J., Buchacz A., Nowak A., Świder J.** (1986), *Modelling of vibration of mechanical systems by means the graph and structural numbers methods*, No. 1266, Silesian University of Technology Press, Gliwice (in Polish).

Acknowledgments. This work has been conducted as a part of the research project No. 50207131/3719 supported by the Committee of Scientific Research in 2006 – 2009.

COMPUTER BASED EDUCATION AND PROGRESS ALTERNATIVE FOR ELECTRO-MECHANICS LESSON

Sezgin ERSOY*, Sertaç GÖRGÜLÜ**

*Marmara University Göztepe Campus Technical Education Faculty Mechatronics Education Department 34722 Goztepe, İstanbul,
**Kirklareli University Technical Education Faculty Kavakli, Kirklareli,

sersoy@marmara.edu.tr, sertac.gorgulu@kırklareli.edu.tr

Abstract: The rapid developments in technology make it costly to educate the work force for the sectors. In modern technology and in today's world in which the education system is more modern and the need for modern stuff is increasingly high, Computer-Based Education (CBE) techniques and software are no more a luxury but a necessity. Because these softwares become the basic component and means of easy and comprehensible manner of telling in modern education system due to the visuality that they concern. This study presents the examples of material to make the content and the subject of electromechanics more effective and comprehensible.

1. INTRODUCTION

1.1. Mechatronics and education

Mechatronics, the popular science of our century, is an interdisciplinary perception which grows out of the combination of machine, electric-electronic and software technology in the process of planning to production. Mechatronics which is in fact shortly expressed as 'interdisciplinary' is a synergism which is formed by technical and physical sciences. Mechatronics: It is the field of implementation which is realized in an interdisciplinary and equal-aimed structure of computer technology. Mechatronics products aim to produce smart machines, devices and systems that make human life easier (Toprakkiran and Ersoy, 2006).

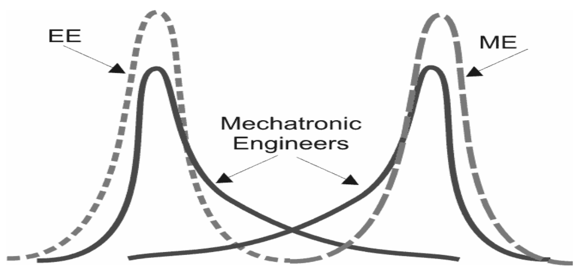

Fig. 1. Mechatronic engineers versus conventional mono-disciplinary EE's and ME's (Van Amerongen, 2006)

The human profile that the society of our present-day needs is different from the human profile that the society of the past-times needs. The globalization occurred due to the improvements in science and technology and the basic components that identify the human force profile which is required by info-based society. The discussions about the quality and quantity of education began to take place and the re-construction in education is put on the agenda. In the period of 2000s, the students' and the teachers' being able to gain new skills depends highly on their being able to use the technology. Because technology is a means of reaching, using, producing and sharing data. The most important means to enable us to reach the data is computers. The use of computers is becoming increasingly important in today's societies.

By considering these things, the educational institutions began work and implementation in order to make the students gain computer skills.

1.2. Web-based education

Within the developments in communication technology, the demand for the informal education has increased. As the instruments which are used in e-learning vary and get stronger, the interest in that type of learning has increased more.

Education and teaching aimed data's transference to the required place electronically by means of communication instruments such as radio, television, computer, internet and similar items is called 'e-learning'. Even the instructor and the student are in different places, the transference of information and teaching function is fulfilled by means of communication technology. Shortly, e-learning eliminates the difficulties of distance and participation. (University of Cukurova, 2007)

The Internet and web offer a number of advantages over other computer-based approaches to distance learning that do not use wide area networks. Here are some of them (Collaboratory for High Performance Computing and Communications, 2008):

1. Resource management;
2. Student/user management;
3. Time/place flexibility;
4. Currency;
5. Ease of use;
6. Cross platform compatibility;

7. Accessibility;
8. Customization;
9. Resource leveraging/enrichment;
10. Resource integration;
11. Collaboration;
12. Dual use;
13. Duplication and other distribution costs;
14. Productivity.

1.3. E-learning and the improvement of e-learning materials

For the teachers' being able to gain the skills to prepare effective teaching materials, they need to know very well the functions of these materials in teaching environment, the principles that they need to consider at the stage of preparation, the benefits and limits of commonly used materials and the features that needs to be considered when they choose and use these materials. When they know these things not in only information level but also in implementation and evaluation level, it will be helpful for these teachers to develop materials in their future lives.

It's shown below the way followed in combining technology and lessons for the education of teacher candidates (Gunduz and Odabasi, 2004).

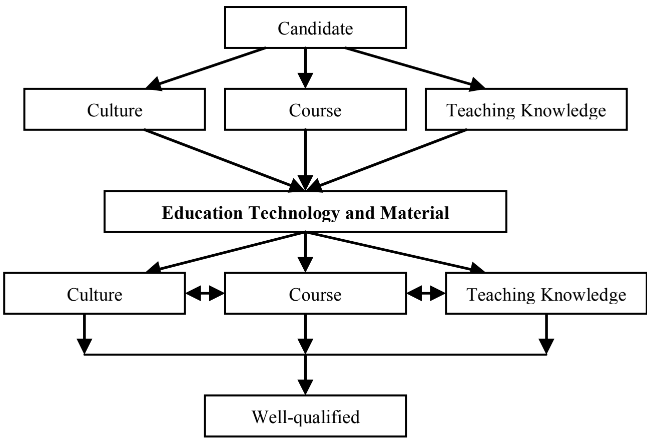

Fig. 2. Process of "education technology and material developing" course in Education Faculty

In order to increase the quality of education and teaching, the effective use of modern teaching technology in teaching of concepts is becoming more important day by day. In that case, one of the most important advantages of the use of computers in teaching environments is its increasing the degree of learning by appealing to a lot of sense organs at the same time and make what's learnt more permanent. Because of that reason, it is pointed out that the use of animations, pictures and sound at the same time eliminates the conventionalism of teaching environment and increases the degree of learning (Saka and Yilmaz, 2005; Clark and Craik,1992). On the other hand, technology-based teaching materials are extremely needed in order to construct teaching environment for the students who come from different social environments and who are physically, biologically and cognitively different from each other. However, the students' having different cognitive, perceptional qualities and physcomotor skills makes it more difficult for teaching technologies to improve by considering individual differences. Because of that, it is emphasized that there is no technology to make it possible that a topic is learnt by all the students at the same degree and at the same speed (Saka and Yilmaz, 2005; Akpinar, 1999).

2. THE STAGES OF DEVELOPMENT OF TEACHING MATERIAL

In order to be used in the software design of research content, "Macromedia Flash5" software is preferred due to its well-known file structure, rapid running, its files' taking little space, its interaction functions and its being user-friendly. In material's development process, the stages below have been fulfilled:

1. Available researches and developed teaching materials were examined by leading the research of computer-based education, experiment notes and related literature.
2. Some examinations were done about the experiments and the qualities of Electro Mechanic Laboratory.
3. The topics that the students have difficulty in the lessons that are done by traditional methods were considered.
4. The identified topics were examined by using the various lesson books which suits to the teaching program. As the result of interviews that are made with instructors, it's decided to develop a study sheet for teaching of these three concepts below.
5. Some experiments about the identified subjects and concepts were done in laboratories and were recorded.
6. A literature scan about visual design was done and the qualifications of an effective and a suitable interface were decided.
7. The necessary animations, texts and shapes were designed for to be prepared packet program by identifying the most suitable animations and design programs for the goal of the research (Fig. 3-5).
8. In Macromedia Flash5 program, an interface is prepared and all animations and texts were inserted into that preface (Fig. 6).
9. The suggestions about the visual design of the education expert were considered.
10. Some visual buttons were inserted in order to enable the interacting use of activity's implementation process.
11. The pilot implementation process will be implemented at the spring term of 2008-2009 education term (Fig. 7).

There are 30 students in the class. These students will be divided into 2 groups as the experiment group and the control group. The control group will have education with traditional methods and the experiment group will take the courses by E-learning Method. The length of time of the implementation of the Experiment group will be as much as the length of time of the implementation of Traditional group which will be exactly one day.

Lesson ELK232 Electromec. Sys. Theoric – 3 / The implementation will be implemented as 2 hours long, totally as 4 credits within 12weeks of academic term. The total implementation time will last for 3 days which will be totally 24 hours.

There needs to be an implementation at the laboratory workshop for the comprehension of topics of this lesson. The connection schemas of controlling unit circuits needs to be drawn at technical lessons in accordance with Turkish standards and the way how it Works needs to be told. During the implementation, some little voltage (lower that 50 V) needs to be used at the weak rheo controlling unit circuits for the security of life.

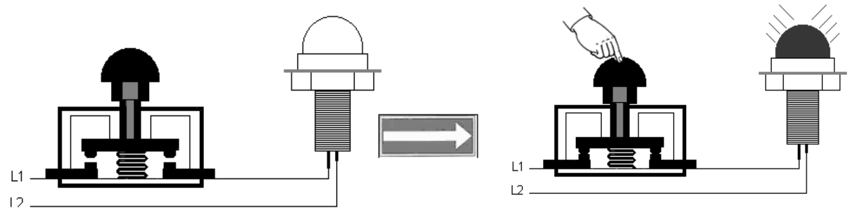

Fig. 3. Schematic shown of open switch in circuit

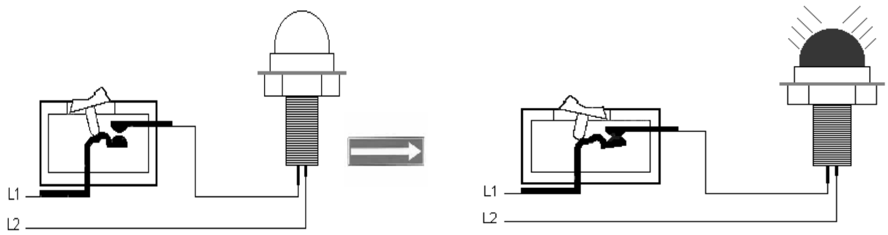

Fig. 4. Schematic shown of wrench in circuit

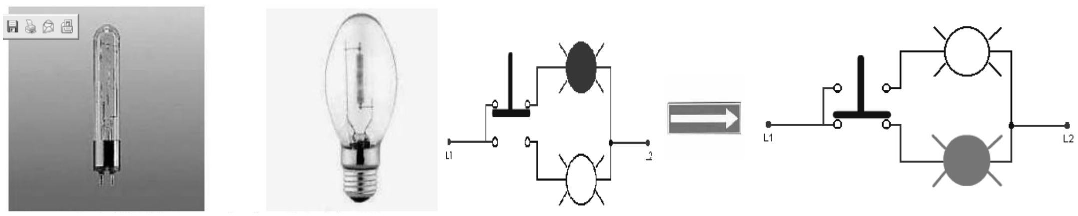

Fig. 5. Lamps and shown in circuit

3. THE CREATION OF THE MATERIALS

We can explain simulation in different ways:

The simulation of a system is the procedure of forming a model which can represent that system. Simulation is a process of the designation of the model of the real system, the implementation of experiments in order to understand the conduct of the system and evaluate the different strategies for the goal of running the system with that model.

Simulation is the experimental study which is done for fulfilling the process procedures of the duration which is improved or reorganized, executing experimental studies and estimating the time of the error of these procedures. We can understand the possible reactions that the new process gives against the changes. It is the observation of a qualification or a conduct about an event, a process or a system on the model.

4. THE COST

The rapid developments in information technology have affected the societies and it became possible for everyone to use the computers. Due to the rapidly changing world, it became a necessity to use the computers in teaching-learning process at schools in order to prepare our children who are face to face with a rapidly changing world to the information societies of 21st century.

As the relationship of the human being with information and society changed in our present day, the qualification of it changed too. The case of information explosion changed the function of information in the life of human being and society and the method of being produced and being gained. The modern society became different in the aspects of structure and function. All of these cases affect the basic model of the education and causes fundamental changes in education (Dogu and Eroglu, 2004).

The matter of education has been considered with common sense rather than a scientific approach for a long time. The education concerns the establishment and the assimilation of the ideas rather than the change of ideas. However, this era that we have been in possesses an imbalanced and an inconstant characteristic and it is characterized by the rapid change. In that atmosphere, the skills in mechanization are replaced by skills in information technology (Ozer, 1989).

In that case, the education needs a change to reprepare itself and a new conceptional frame in which the decisions about the innovation can be taken easily (Dogu and Eroglu, 2004).

The change for output and effectiveness in the process of teaching and learning becomes more and more important. Because the education services constitute one of the biggest costs in the life of the nations.Today none of the societies can endure an education with a high cost and low output (Dogu and Eroglu, 2004).

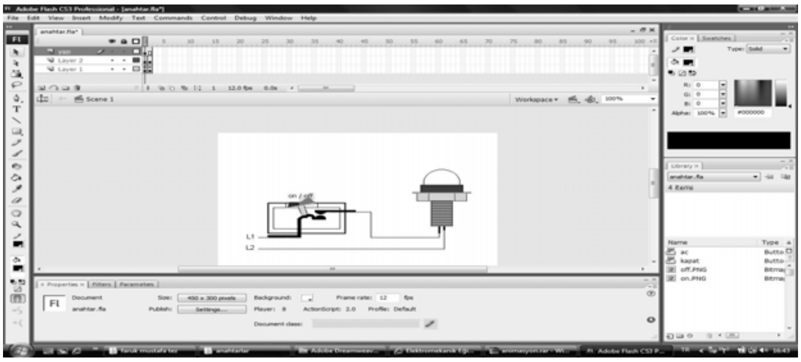

Fig. 6. Generated to materials animations

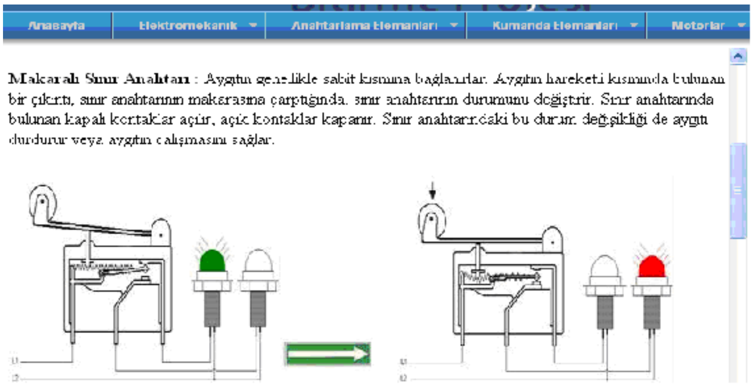

Fig. 7. Web page of using in Electro – mechanics course

5. CONCLUSION

The education which is put into practice during the process of educating workforce in developing disciplines like Mechathronics is costly and difficult. In addition the distribution and the spread of information is highly important at the process of globalization. The implementation and the pursuit of information during its stages of rise and development are possible with e-learning. Digital and online materials can dramatically reduce the cost of education materials, particularly for university students and researchers (Oxfam Briefing Paper, 2008).

The electro-mechanic lesson materials that we submitted during our study take little part in Mechathronic Education. The institutions need to focus on the studies about the e-learning model, spread it everywhere and form a basis for the updates.

REFERENCES

1. **Akpınar Y.** (1999), Bilgisayar destekli öğretim ve bilgi toplumunda insan nitelikleri, *Bilişim Teknolojileri Işığında Eğitim Konferansı ve Sergisi Bildirileri*, Ortadoğu Teknik Üniversitesi, 145.
2. **Clark R. E., Craik, T. G.** (1992), Interactive multimedia learning environments, *NATO ASI Series F: Computer and System Sciences*, 93, Springer, Berlin.
3. **Doğu M. B., Eroğlu E.** (2004), Uzaktan Öğretimde Kalite: .. Sayısal büyüklükler doyuma ulaştı.. Ya şimdi?.., *The Turkish Online Journal of Educational Technology – TOJET*, Vol. 3, Issue 4, Art. 20.
4. **Gündüz Ş., Odabaşı F.** (2004), Bilgi Çağında Öğretmen Adaylarının Eğitiminde Öğretim Teknolojileri ve Materyal Geliştirme Dersinin Önemi, *The Turkish Online Journal of Educational Technology – TOJET*, Vol. 3, Issue 1, Art. 7.
5. **Özer, B.**, Türkiye'de Uzaktan Eğitim, *Anadolu Üniversitesi Eğitim Fakültesi Dergisi*, Ekim, Cilt: 2, Sayı: 2, 1-24.
6. **Saka A. Z., Yılmaz M.** (2005), Bilgisayar Destekli Fizik Öğretiminde Çalışma Yapraklarına Dayalı Materyal Geliştirme Ve Uygulama, *The Turkish Online Journal of Educational Technology – TOJET*, Vol. 4, Issue 3, Art. 17.
7. **Toprakkıran S., Ersoy S.** (2006), *Eğitimde ve Endüstride Mekatronik*, Bilisim Market Dergisi, Ekim.
8. **Van Amerongen, J.** (2004), Mechatronics education and research - 15 years of experience, *3rd IFAC Symposium on Mechatronic Systems*, Sydney, Australia, 595–607.
9. Partnership or Power play?, Oxfam Briefing Paper, April 2008 www.fes.de/cotonou/OTHER_BACKGROUND_TRADE/PARTNERSHIP_OR_POWERPLAY_OXFAM_22APRIL2008.PDF (accessed Nov 2008)
10. http://collab.nlm.nih.gov/tutorialspublicationsandmaterials/sitedesign/sitedesign.html#1.1 (accessed Nov 2008)
11. http://e.cu.edu.tr/tanitim/distEdu.asp (accessed Nov 2008)

FINITE ELEMENT ANALYSIS OF DISC TEMPERATURE DURING BRAKING PROCESS

Piotr GRZEŚ*

*Faculty of Mechanical Engineering, Białystok Technical University, ul. Wiejska 45 C, 15-351 Białystok

p.grzes@doktoranci.pb.edu.pl

Abstract: The aim of this paper was to investigate the temperature fields of the solid disc brake during short, emergency braking. The standard Galerkin weighted residual algorithm was used to discretize the parabolic heat transfer equation. The finite element simulation for two-dimensional model was performed due to the heat flux ratio constantly distributed in circumferential direction. Two types of disc brake assembly with appropriate boundary and initial conditions were developed. Results of calculations for the temperature expansion in axial and radial directions are presented. The effect of the angular velocity and the contact pressure evolution on temperature rise of disc brake was investigated. It was found that presented finite element technique for two-dimensional model with particular assumption in operation and boundary conditions validates with so far achievements in this field.

1. INTRODUCTION

Over decades, frictional heating in brakes and clutches has been investigated by many researches. Temperature rise affected by conversion of large amounts of kinetic energy into heat energy is a complex phenomenon. All characteristics of the process (velocity, pressure, friction coefficient, thermal properties of the materials) vary with time. However, it is important to predict temperature distribution of heat generation during braking and clutch engagement.

Long repetitive braking terms, particularly during mountain descents or high-speed stops (autobahn stop) may cause significant concern. Undesirable effects (low frequency vibrations, fade of the lining with variations of friction coefficient, premature wear, brake fluid vaporization) directly affect braking performance. Hence it is essential to know the peak temperatures at the beginning of the design process.

Talati and Jalalifar (2008, 2009) formulated the problem of two models of heat dissipation in disc brakes: namely macroscopic and microscopic model. In the macroscopic model First Law of Thermodynamics has been taken into account and for microscopic model various characteristics such as duration of braking, material properties, dimensions and geometry of the brake system have been studied. Both disc and pad volume have been investigated to evaluate temperature distributions. The conduction heat transfer was investigated using finite element method (Talati and Jalalifar, 2008). In paper (Talati and Jalalifar, 2009) problem was solved analytically using Green's function approach. Influence of thermomechanical distortions during heat generation has been neglected.

Gao and Lin (2002) investigated non-axisymmetrical model of disc brake system with moving heat source. Appropriate boundary conditions due to analytical model have been imposed. To solve the problem, a transient FE technique has been used. Numerical estimations reveal that the operating parameters of the braking process significantly influence the disc/pad interface temperature distribution and the maximal contact temperature.

According to Ramachandra Rao et al. (1989) it is essential that the analysis is treated as a nonlinear (thermal conductivity and enthalpy for the disc material vary with respect to temperature). In this paper the simulation of the temperature field in the disc brake has been carried out using the finite element method. Both, wear and temperature distribution have been considered. The computer simulation of the fade mechanism using 'clock mechanism' is examined which is also verified with the experimental outcome.

Grieve et al. (1998) compares different materials for pad element of automotive disc brake with its significant weight advantages corresponds to lower maximum operating temperature. Three dimensional model of brake system assembly has been imposed with the finite element method simulation. The author examines the effect of the vehicle mass on the peak disc temperatures. Also Taguchi technique (1993) has been applied to develop influence of all the critical design and material factors.

FE modelling of the heat generation process in a mine winder disc brake is proposed in monograph: Ścieszka and Żołnierz (2007).

In this study, transient thermal analysis of disc brake utilizing finite element method is developed. Both analytical and numerical investigations are performed. Various boundary and operation conditions in two types of FE models with appropriate material properties (Talati and Jalalifar, 2009; Gao and Lin, 2002) are established.

2. REAL PROBLEM

Disc brake consists of cast-iron disc which rotates with the wheel, caliper fixed to the steering knuckle and friction material (brake pads) which is shown in Fig 1. When the braking process occurs, the hydraulic pressure forces the piston and therefore pads and disc brake are in sliding contact. Set up force resists the movement and the vehicle slows down or eventually stops. Friction between disc and pads always opposes motion and the heat is generated due to conversion of the kinetic energy. However, friction surface is exposed to the enlarged air flow for high speed braking and the heat is dissipated.

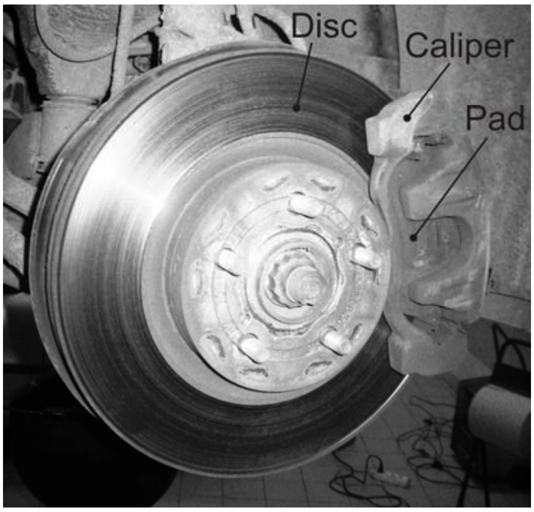

Fig. 1. Front disc brake of the passenger's car

Disc brake. In general disc brakes are made of gray cast iron and are either solid or ventilated. The ventilated types of discs have vanes or fins to increase surface of heat exchange by convection. Furthermore, higher order of disc brakes have drilled holes. Nowadays a cross-drilled discs are commonly used in motorcycles, racing cars or very high performance road cars. Cross-drilled enables more efficient gas release in the brake exert. The disc must have limited mass in order to diminish the inertia forces and non-suspending mass.

Pads. Several assumptions should be considered in the case of design process of friction material. It is known that the value of sliding friction depends of the nature of two surfaces which touch each other. Material selection must deal with the coefficient of friction which is supposed to remain constant in the braking process corresponding to wide variety of disc/pad interface temperature. Also wear is vital in case of braking performance.

Caliper. Generally two types of calipers are commonly used: the floating calipers and the fixed calipers. Depending on the way of operation, the floating caliper has either one or two pistons.

In the floating caliper (Fig. 1) the piston is located only in one side of the disc. Equal pressure at the same time is distributed on the two inner surfaces of pads by using reaction when the pressure acts piston on the one side of the disc.

The fixed caliper have two pistons in both sides of the disc brake. The equilibrium of pressure at any pad is settled by the single source of the hydraulic pressure partitioned to each canal of the piston. This type of caliper is heavier and also larger because of complexity of the disc brake assembly. The advantage is that they absorb more energy by heat dissipation.

3. PHYSICAL PROBLEM

Disc brake system consists of two elements: rotating axisymmetric disc and immovable non-axisymmetric pad (Fig. 2). The most important function of disc brake system in automotive application is to reduce velocity of the vehicle by changing the kinetic energy into thermal energy. When the braking process occurs total heat is dissipated by conduction from disc/pad interface to adjacent components of brake assembly and hub and by convection to atmosphere in accordance to Newton's law. The radiation may be neglected due to relatively low temperature and short time of the braking process.

In this paper for validation of proposed finite element (FE) modeling technique, two types of solid disc brake were analyzed (Fig. 2). Type A according to Talati and Jalalifar's paper (2009) and Type B according to Gao and Lin's paper (2002).

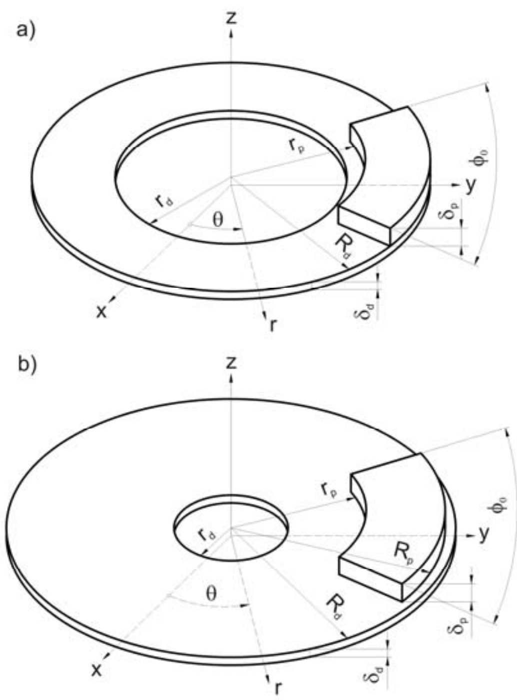

Fig. 2. The schematic representation of disc brake system a) Type A; b) Type B

For both types it has been assumed as follows:

1) Material properties are isotropic and independent of the temperature;
2) The real surface of contact between a disc brake and pad in operation is equal to the apparent surface in the

sliding contact. Hence pressure is uniformly distributed over all friction surfaces;

3) The average intensity of heat flux into disc on the contact area equals (Ling, 1973):

$$q_d(r,z,t)\big|_{z=\delta_d} = \gamma \frac{\phi_0}{2\pi} fp(t) r\omega(t), \quad (1)$$

$$r_p \le r \le R_p, 0 \le t \le t_s,$$

and into pad

$$q_p(r,z,t)\big|_{z=\delta_p} = (1-\gamma) fp(t) r\omega(t), \quad (2)$$

$$r_p \le r \le R_p, 0 \le t \le t_s,$$

where: γ is the heat partitioning factor, ϕ_0 is the cover angle of pad, f is the friction coefficient, p is the contact pressure, ω is the angular velocity, t is the time, t_s is the braking time, r is the radial coordinate, z is the axial coordinate, r_p and R_p are the internal and external radius of the pad. The subscripts p and d imply the pad and the disc respectively;

4) The heat partitioning factor representing the fraction of frictional heat flux entering the disc has the form (Blok, 1940):

$$\gamma = \frac{1}{1+\sqrt{\rho_p c_p K_p / \rho_d c_d K_d}}, \quad (3)$$

where ρ is the density, c is the specific heat and K is the thermal conductivity;

5) The frictional heat due to Newton law has been dissipated to atmosphere on the other surfaces. The heat transfer coefficient h is constant during braking process;
6) Because of short braking time and hence relatively low temperature the radiation is neglected.

Two types of single disc have been analyzed with its simplification to symmetrical problem. Therefore one side of the disc has been insulated in both types of the FE model.

In Type A the single surface of disc symmetry is insulated. Excluding both the surface of symmetry and the surface of sliding contact with the intensity of heat flux boundary condition, on all remaining surfaces the exchange of thermal energy by convection to atmosphere has been implied.

Furthermore in Type B the inner surface of disc was thermally insulated. On the area of sliding contact of disc brake surface intensity of the heat flux has been established. The frictional heat due to Newton law has been dissipated to atmosphere on the other surfaces.

In Type A the contact pressure p is given as follows

$$p = p_0, \quad (4)$$

and the angular velocity ω is linear in time t:

$$\omega(t) = \omega_0\left(1 - \frac{t}{t_s^0}\right), \quad 0 \le t \le t_s^0 \quad (5)$$

where: p_0 is the nominal pressure, ω_0 is the initial angular velocity, t_s^0 is the time of braking with constant deceleration.

The opposite approach is presented in Type B. It is assumed, that the pressure varies with time (Chichinadze et al., 1979)

$$p(t) = p_0\left(1 - e^{-\frac{t}{t_m}}\right), \quad 0 \le t \le t_s, \quad (6)$$

where: t_m is the growing time. The angular velocity corresponds to pressure (6) and is equal (Yevtushenko et al., 1999)

$$\omega(t) = \omega_0\left[1 - \frac{t}{t_s^0} + \frac{t_m}{t_s^0}\left(1 - e^{-\frac{t}{t_m}}\right)\right], \quad 0 \le t \le t_s, \quad (7)$$

4. MATHEMATICAL MODEL

To evaluate the contact temperature conditions, both analytical and numerical techniques have been developed. The starting point for the analysis of the temperature field in the disc volume is the parabolic heat conduction equation in the cylindrical coordinate system (r, θ, z) which is centered in the axis of disc and z points to its thickness (Nowacki, 1962)

$$\frac{\partial^2 T}{\partial r^2} + \frac{1}{r}\frac{\partial T}{\partial r} + \frac{1}{r^2}\frac{\partial^2 T}{\partial \theta^2} + \frac{\partial^2 T}{\partial z^2} = \frac{1}{k_d}\frac{\partial T}{\partial t}, r_d \le r \le R_d, \quad (8)$$

$$0 \le \theta \le 2\pi, 0 < z < \delta_d, t > 0$$

where k_d is the thermal diffusivity of the disc, r_d and R_d are he internal and external radius of the disc. In an automotive disc brakes the Peclet numbers almost always are in order 10^5. Hence the distribution of heat flow will be uniform in circumferential direction, which means that neither temperature nor heat flow will vary in θ direction and thus the heat conduction equation reduces to

$$\frac{\partial^2 T}{\partial r^2} + \frac{1}{r}\frac{\partial T}{\partial r} + \frac{\partial^2 T}{\partial z^2} = \frac{1}{k_d}\frac{\partial T}{\partial t}, r_d \le r \le R_d, 0 < z < \delta_d, t > 0, \quad (9)$$

The boundary and initial conditions are given as follows:
Type A

$$K_d \frac{\partial T}{\partial z}\bigg|_{z=\delta_d} = \begin{cases} h[T_a - T(r,\delta_d,t)], \ r_d \le r \le r_p, \ t \ge 0, \\ q_d(r,\delta_d,t), \ r_p \le r \le R_p, \ 0 \le t \le t_s, \end{cases} \quad (10)$$

where T_a is the ambient temperature.

$$K_d \frac{\partial T}{\partial r}\bigg|_{r=R_d} = h[T_a - T(R_d,z,t)], \ 0 \le z \le \delta_d, \ t \ge 0, \quad (11)$$

$$K_d \frac{\partial T}{\partial r}\bigg|_{r=r_d} = -h[T_a - T(r_d,z,t)], \ 0 \le z \le \delta_d, \ t \ge 0, \quad (12)$$

$$\frac{\partial T}{\partial z}\bigg|_{z=0} = 0, \ r_d \le r \le R_d, \ t \ge 0, \quad (13)$$

$$T(r,z,0) = T_0, \ r_d \le r \le R_d, \ 0 \le z \le \delta_d, \quad (14)$$

Type B

$$K_d \left.\frac{\partial T}{\partial z}\right|_{z=\delta_d} = \begin{cases} h[T_a - T(r,\delta_d,t)], \; r_d \le r \le r_p \wedge R_p \le r \le R_d, t \ge 0, \\ q_d(r,\delta_d,t), r_p \le r \le R_p, \; t \ge 0, \end{cases} \quad (15)$$

$$K_d \left.\frac{\partial T}{\partial r}\right|_{r=R_d} = h[T_a - T(R_d,z,t)], \;\; 0 \le z \le \delta_d \,,\; t \ge 0 \,, \quad (16)$$

$$\left.\frac{\partial T}{\partial r}\right|_{r=r_d} = 0 \,,\; 0 \le z \le \delta_d \,,\; t \ge 0 \,, \quad (17)$$

$$\left.\frac{\partial T}{\partial z}\right|_{z=0} = 0 \,,\; r_d \le r \le R_d \,,\; t \ge 0 \,, \quad (18)$$

$$T(r,z,0) = T_0 \,,\; r_d \le r \le R_d \,,\; 0 \le z \le \delta_d \,, \quad (19)$$

The above cases are two-dimensional problem for transient analysis. The boundary and initial conditions are specified for subsequent types of disc.

5. FE FORMULATION

The object of this section is to develop approximate time-stepping procedures for axisymmetrical transient governing equations. For this to happen, the following boundary and initial conditions are considered

$$T = T_p \text{ on } \Gamma_T \quad (20)$$

$$q = -h(T - T_a) \text{ on } \Gamma_h \quad (21)$$

$$q = q_d \text{ on } \Gamma_q \quad (22)$$

$$T = T_0 \text{ on at time } t = 0 \quad (23)$$

where T_p is the prescribed temperature, Γ_T, Γ_h, Γ_q, are arbitrary boundaries on which temperature, convection and heat flux are prescribed.

In order to obtain matrix form of Eq. (9) the application of standard Galerkin's approach was conducted (Lewis et al., 2004). The temperature was approximated over space as follows

$$T(r,z,t) = \sum_{i=1}^{n} N_i(r,z) T_i(t) \quad (24)$$

where: N_i are shape functions, n is the number of nodes in an element, $T_i(t)$ are time dependent nodal temperatures.

The standard Galerkin's approach of Eq. (9) leads to the following equation

$$\int_\Omega K_d N_i \left[\frac{\partial^2 T}{\partial r^2} + \frac{1}{r}\frac{\partial T}{\partial r} + \frac{\partial^2 T}{\partial z^2} - \rho_d c_d \frac{\partial T}{\partial t} \right] d\Omega = 0 \quad (25)$$

Using integration by parts of Eq. (25) we obtain

$$\begin{aligned} &-\int_\Omega K_d \left[\frac{\partial N_i}{\partial r}\frac{\partial T}{\partial r} + \frac{\partial N_i}{\partial z}\frac{\partial T}{\partial z} - \frac{N_i}{r}\frac{\partial T}{\partial r} + N_i \rho_d c_d \frac{\partial T}{\partial t} \right] d\Omega \\ &+ \int_\Gamma K_d N_i \frac{\partial T}{\partial r} l d\Gamma + \int_\Gamma K_d N_i \frac{\partial T}{\partial z} n d\Gamma = 0 \end{aligned} \quad (26)$$

Integral form of boundary conditions

$$\begin{aligned} &\int_\Gamma K_d N_i \frac{\partial T}{\partial r} l d\Gamma + \int_\Gamma K_d N_i \frac{\partial T}{\partial z} n d\Gamma \\ &= -\int_{\Gamma_q} N_i q_d d\Gamma_q - \int_{\Gamma_h} N_i h (T - T_a) d\Gamma_h \end{aligned} \quad (27)$$

Substituting Eq. (27) and spatial approximation Eq. (24) to Eq. (26) we obtain

$$\begin{aligned} &-\int_\Omega K_d \begin{bmatrix} \frac{\partial N_i}{\partial r}\frac{\partial N_j}{\partial r} + \frac{\partial N_i}{\partial z}\frac{\partial N_j}{\partial z} \\ -\frac{N_i}{r}\frac{\partial N_j}{\partial r} \end{bmatrix} T_j d\Omega \\ &-\int_\Omega \rho_d c_d N_i \frac{\partial N_j}{\partial t} T_j d\Omega - \int_{\Gamma_q} N_i q_d d\Gamma_q \\ &-\int_{\Gamma_h} N_i h (T - T_a) d\Gamma_h = 0 \end{aligned} \quad (28)$$

where i and j represent the nodes.
Equation (28) can be written in matrix form

$$[C]\left\{\frac{\partial T}{\partial t}\right\} + [K][T] = \{R\} \quad (29)$$

where $[C]$ is the heat capacity matrix, $[K]$ is the heat conductivity matrix, and $\{R\}$ is the thermal force matrix.
or

$$[C_{ij}]\left\{\frac{\partial T_j}{\partial t}\right\} + [K_{ij}][T_j] = \{R_i\} \quad (30)$$

where

$$[C_{ij}] = \int_\Omega \rho_d c_d N_i N_j d\Omega \quad (31)$$

$$\begin{aligned} [K_{ij}] &= \int_\Omega K_d \left(\frac{\partial N_i}{\partial r}\frac{\partial N_j}{\partial r}\{T_j\} + \frac{\partial N_i}{\partial z}\frac{\partial N_j}{\partial z}\{T_j\} - \frac{N_i}{r}\frac{\partial N_j}{\partial r}\{T_j\} \right) d\Omega \\ &+ \int_\Gamma h N_i N_j d\Gamma \end{aligned} \quad (32)$$

$$[R_i] = -\int_{\Gamma_q} q_d N_i d\Gamma_q + \int_{\Gamma_h} N_i h T_a d\Gamma_h \quad (33)$$

or in matrix form

$$[C] = \int_\Omega \rho_d c_d [N]^T [N] d\Omega \quad (34)$$

$$[K] = \int_\Omega [B]^T [D][B] d\Omega + \int_\Gamma h [N]^T [N] d\Gamma \quad (35)$$

$$\{R\} = -\int_{\Gamma_q} q_d [N]^T d\Gamma_q + \int_{\Gamma_h} h T_a [N]^T d\Gamma_h \quad (36)$$

In order to solve the ordinary differential equation (29) the direct integration method was used. Based on the assumption that temperature $\{T\}_t$ and $\{T\}_{t+\Delta t}$ at time t and $t+\Delta t$ respectively, the following relation is specified

$$\{T\}_{t+\Delta t} = \{T\}_t + \left[(1-\beta)\left\{\frac{\partial T}{\partial t}\right\}_t + \beta\left\{\frac{\partial T}{\partial t}\right\}_{t+\Delta t} \right] \Delta t \quad (37)$$

Substituting Eq. 37 to Eq. 29 we obtain the following implicit algebraic equation

$$\left([C]+\beta\Delta t[K]\right)\{T\}_{t+\Delta t}=\left([C]-(1-\beta)[K]\Delta t\right)\{T\}_t + (1-\beta)\Delta t\{R\}_t+\beta\Delta t\{R\}_{t+\Delta t} \quad (38)$$

where β is the factor which ranges from 0.5 to 1 and is given to determine an integration accuracy and stable scheme.

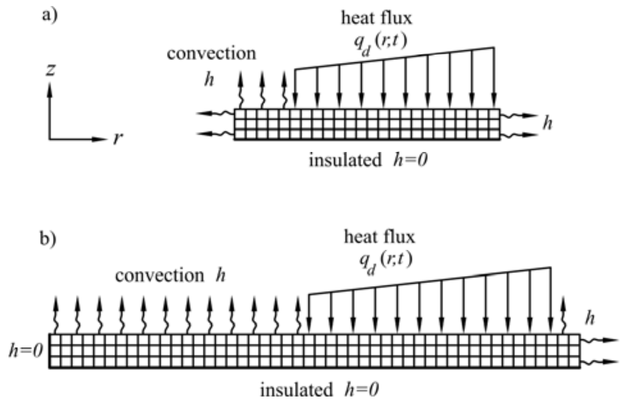

Fig. 3. FE models with boundary conditions for the transient analysis a) Type A, b) Type B

The finite element formulation of disc brakes with boundary conditions is shown in Fig. 3. Two FE models described below were analyzed using the MD Patran/MD Nastran software package (Reference Manual MD Nastran, 2008; Reference Manual MD Patran, 2008). In the thermal analysis of disc brakes an appropriate finite elements division is indispensable. In this paper eight-node quadratic elements were used for finite element analysis. Type A consists of 235 elements and 810 nodes and Type B 570 elements and 1913 nodes. High order of elements ensure appropriate numerical accuracy.

To avoid inaccurate or unstable results, a proper initial time step associated with spatial mesh size is essential (Reference Manual MD Nastran, 2008).

$$\Delta t=\Delta x^2\frac{\rho_d c_d}{10K_d} \quad (39)$$

where Δt is the time step, Δx is the mesh size (smallest element dimension). In this paper fixed Δt =0.005s time step was used.

6. RESULTS AND DISCUSSION

In this paper temperature distributions in disc brake model without pad have been investigated. It is connected with its sophisticated behaviour and importance of operation. Disc material is subjected to high temperatures action which may cause non-uniform pressure distribution, thermal distortions, low frequency vibrations. Both convection and conduction have been analyzed. Particularly conduction was considered to be the most important mode of heat transfer.

In order to validate proposed transient numerical analysis two different types of the FE model were investigated (Talati and Jalalifar, 2009; Gao and Lin, 2002). A transient solution for Type A was performed for operation conditions of constant contact pressure p_0=3.17MPa and initial angular velocity ω_0=88.46s^{-1} during 3.96s of braking process (Fig. 4a). Evolution of the pressure p and angular velocity of the disc ω for Type B is shown in Fig. 4b. Material properties and operation conditions adopted in the analysis for both types of disc numerical model are given in Tab. 1 and Tab. 2 respectively.

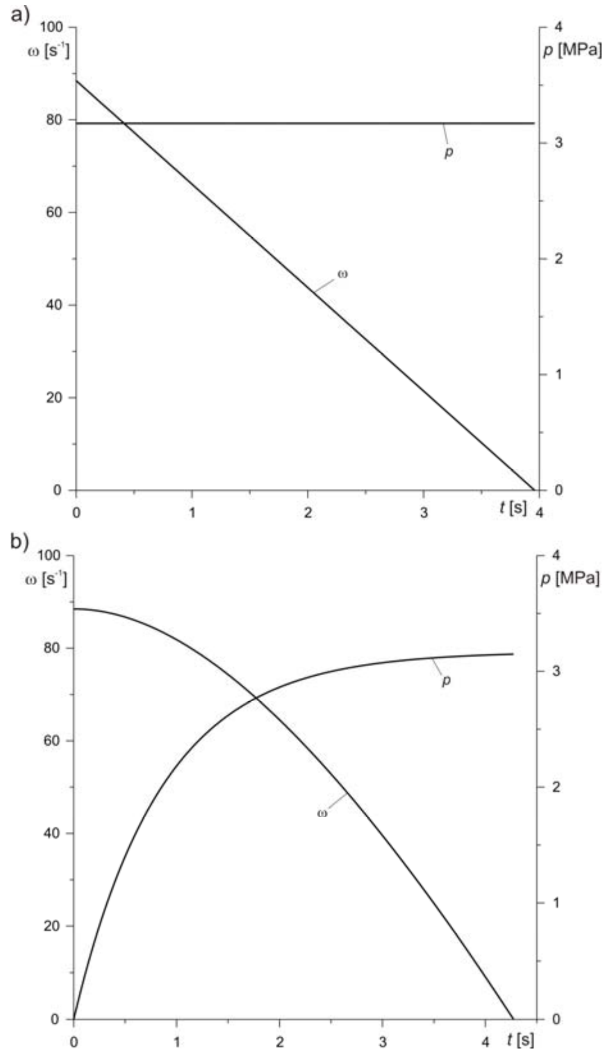

Fig. 4. Evolution of the pressure p and angular velocity ω during braking: a) Type A, b) Type B

Fig. 5a shows disc surface temperature distribution for transient numerical computation (Type A) at different radial distances. As it can be seen values of temperature increase with radial distances. The highest temperature of brake exert occurs at 113.5mm of radial position and t=3.025s of time. Temperature distribution corresponds intermediately to the intensity of heat flux, which rises with time until the value of velocity and pressure product attains highest, critical value. Hence temperature indirectly increases with time and decreases when the intensity of heat flux q_d descents. The slope $\partial T/\partial t$ of plots r=75.5mm, r=80mm, r=90mm, r=100mm, r=113.5mm decreases with time. It agree well with Talati and Jalalifar's paper (2009) with distinction to values of temperatures. In this paper the highest temperature of disc area, which occurs during emergency braking achieves 227.90^{0}C. Meanwhile maximum temperature obtained in Talati's model of disc brake is higher and equals approximately 300^{0}C.

Fig. 5b shows disc temperature surface variations along radial direction obtained in numerical computation for Type B. In opposite to constant pressure at the disc/pad interface, in this case pressure differs with time (Fig. 4b.). Also angular velocity has been assumed as a nonlinear. As it can be seen temperature at inner disc surface (r=52 mm) has a constant value 20^{0}C. It corresponds to boundary conditions, where surface was insulated. Maximum temperature rise up to 280.9^{0}C at 113mm of radial position and 3.49s of time.

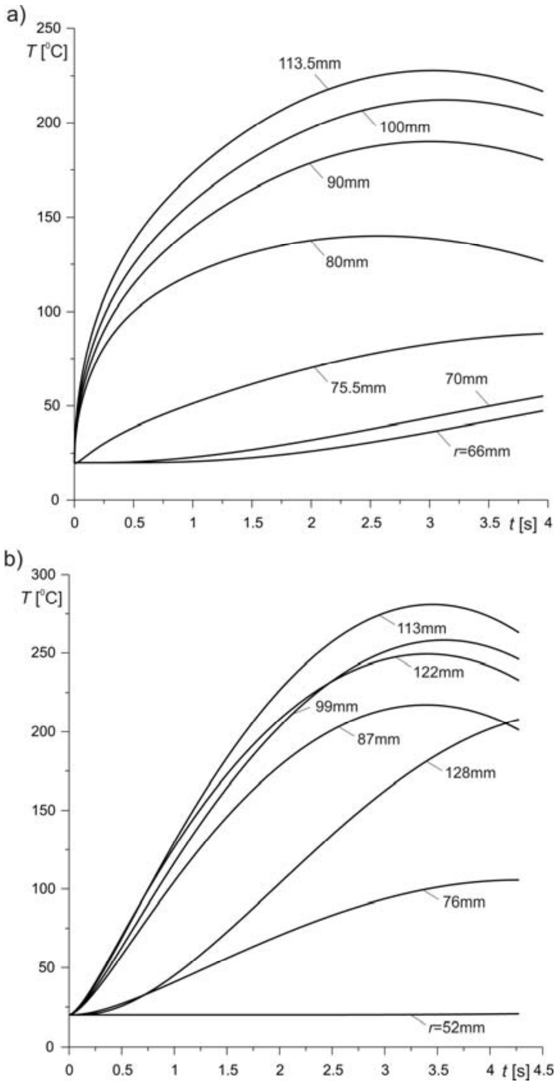

Fig. 5. Evolution of the disc temperature on the friction surface for different values of the radial position:
a) Type A, b) Type B

In Fig. 6a disc temperature in Type A at r=113.5mm and at different axial positions is illustrated. Symmetry in axial direction has been assumed. Hence plots from z=0mm to maximum thickness of the disc are shown. At the initial period of disc brake engagement maximum temperature distribution appears at the disc/pad interface (z=5.5mm). There is a tendency to convergence of temperature at different axial positions at the end of braking process. It is connected with alignment of temperatures in disc brake in subsequent stage of the process when the intensity of heat flux descents. Temperature of plots z=4.4mm, z=5.5mm rises with time to 3.47s and 3.025s respectively.

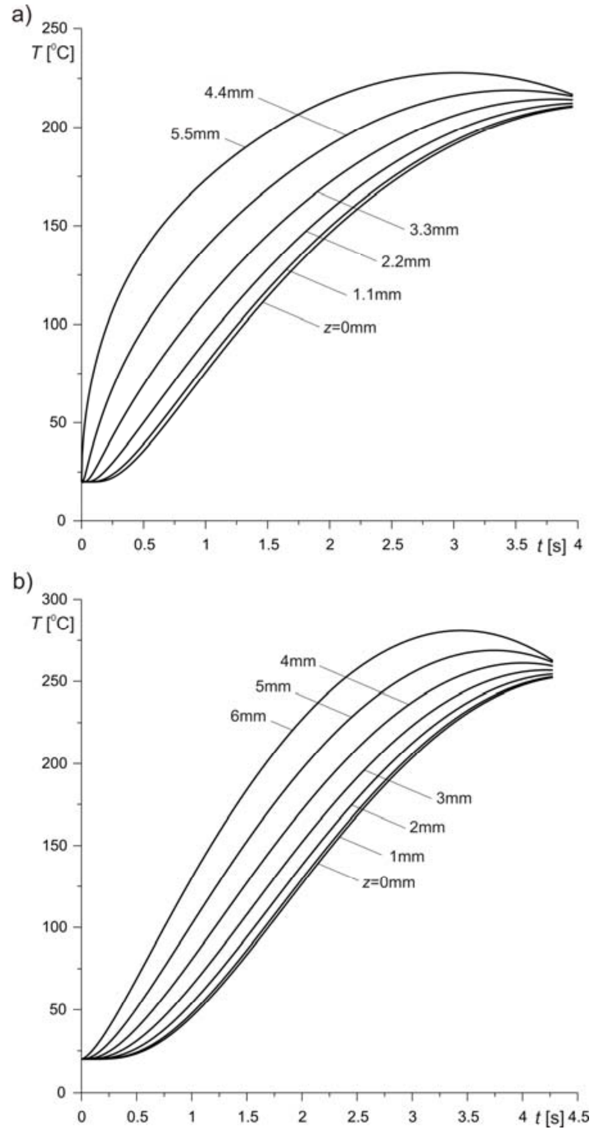

Fig. 6. Evolution of the disc temperature at different axial distances and at radial position:
a) r=113.5mm (Type A) b) r=113mm (Type B)

In Fig. 6b temperature distribution at r=113mm in different axial distances is shown. As it can be seen temperature of plots z=4mm, z=5mm, z=6mm increases with time to 4s, 3.74s and 3.44s respectively and then decreases while temperature of plots z=0mm, z=1mm, z=2mm, z=3mm constantly grows.

Tab. 1. Material properties used in finite element analysis

Thermo-physical properties	Type A [13]		Type B [3]	
	Disc	Pad	Disc	Pad
thermal conductivity, K_d [W/mK]	43	12	48.46	1.212
heat capacity, c_d [J/kgK]	445	900	419	1465
density, ρ_d [kg/m^3]	7850	2500	7228	2595

Tab. 2. Operation conditions for the transient numerical analysis

Items	Type A [13]		Type B [3]	
	Disc	Pad	Disc	Pad
inner radius, $r_{d,p}$[mm]	66	76.5	32.5	77
outer radius, $R_{d,p}$ [mm]	113.5		128	125
cover angle of pad, ϕ_0		64.5		64.5
disc thickness δ_d [mm]	5.5		6	
initial velocity ω_0 [s^{-1}]	88.46		88.46	
time of braking, t_s [s]	3.96		4.274	
pressure p_0 [MPa]	3.17		3.17	
coefficient of friction f	0.5		0.5	
heat transfer coefficient h [W/m^2K]	60		100	
initial temperature T_0 [^0C]	20		20	
ambient temperature T_a [^0C]	20		20	
time step Δt [s]	0.005		0.005	

7. CONCLUSION

In this paper transient thermal analysis of disc brakes in single brake application was performed. To obtain the numerical simulation parabolic heat conduction equation for two-dimensional model was used. The results show that both evolution of rotating speed of disc and contact pressure with specific material properties intensely effect disc brake temperature fields in the domain of time. Proposed transient FE modeling technique of two types of braking engagement model agrees well with papers Talati and Jalalifar (2009), Gao and Lin (2002). An instant pressure action of disc/pad interface (Type A) pronouncedly implies temperature growth at initial period of brake exert. More slightly temperature rise in Type B has been noticed. The highest temperature occurs approximately at 3s, 3.5s into the braking process for the period of 3.96s, 4.274s time in Type A and Type B respectively. The present paper is a preliminary of subsequent investigation with nonlinear variations of applied thermal characteristics.

REFERENCES

1. **Blok H.** (1940), Fundamental Mechanical Aspects in Boundary Lubrication, *SAE Trans*., Vol. 46, 54-68.
2. **Chichinadze A. V., Braun E. D., Ginsburg A. G. et al.** (1979), *Calculation, test and selection of frictional couples*, Science, Moscow *(in Russian).*
3. **Gao C. H., Lin X. Z.** (2002), Transient temperature field analysis of a brake in a non-axisymmetric three-dimensional model, *J. Mater. Proc. Technol.*, Vol. 129, No 1, 513–517.
4. **Grieve D. G., Barton D. C., Crolla D. A., Buckingham J. T.** (1998), Design of a lightweight automotive brake disc using finite element and Taguchi techniques, *Proc. Instn. Mech. Engrs.*, Vol. 212, No 4, 245-254.
5. **Lewis R. W., Nithiarasu P., Seetharamu K. N.** (2004), *Fundamentals of the finite element method for Heat and Fluid Flow*, John Wiley & Sons.
6. **Ling F. F.** (1973), *Surface mechanics*, John Wiley & Sons, New York.
7. **Nowacki W.** (1962), *Thermoelasticity*, Pergamon Press, Oxford.
8. **Ramachandra Rao V. T. V. S., Ramasubramanian H. and Seetharamu K. N.** (1989), Analysis of temperature field in brake disc for fade assessment, *Wärme- und Stoffübertragung*, Vol. 24, No 1, 9-17.
9. **Ścieszka S., Żołnierz M.** (2007), Wpływ cech konstrukcyjnych hamulca tarczowego maszyny wyciągowej na jego niestabilność termosprężystą. Część I. Budowa modelu MES i jego weryfikacja, *Zagadnienia Eksploatacji Maszyn*, Vol. 42, No 3, 111-124.
10. **Ścieszka S., Żołnierz M.** (2007), Wpływ cech konstrukcyjnych hamulca tarczowego maszyny wyciągowej na jego niestabilność termosprężystą. Część II. Badania symulacyjne, *Zagadnienia Eksploatacji Maszyn*, Vol. 42, No 4, 183-193.
11. **Taguchi G.** (1993), *Taguchi on Robust Technology Development*, ASME Press, New York.
12. **Talati F., Jalalifar S.** (2008), Investigation of heat transfer phenomena in a ventilated disk brake rotor with straight radial rounded vanes, *Journal of Applied Sciences*, Vol. 8, No 20, 3583-3592.
13. **Talati F., Jalalifar S.** (2009), Analysis of heat conduction in a disk brake system, *Heat Mass Transfer*, Vol. 45, No 8, 1047-1059.
14. **Yevtushenko A. A., Ivanyk E. G., Yevtushenko O. O.** (1999), Exact formulae for determination of the mean temperature and wear during braking. *Heat and Mass Transfer*, Vol. 35, No 2, 163–169.
15. **MSC.Software** (2008), *Reference Manual MD Nastran, Version r2.1.*
16. **MSC.Software** (2008), *Reference Manual MD Patran, Version r2.1*.

THE POSSIBILITY OF APPLICATION OF B-SPLINE FAMILY WAVELETS IN THE DIAGNOSTIC SIGNAL PROCESSING

Andrzej KATUNIN[*], Anna KORCZAK[**]

[*]Department of Fundamentals of Machinery Design, Faculty of Mechanical Engineering, Silesian University of Technology, ul. Konarskiego 18A, 44-100 Gliwice,

[**]Institute of Mathematics, Faculty of Mathematics and Physics, Silesian University of Technology, ul. Kaszubska 23, 44-100 Gliwice

andrzej.katunin@polsl.pl, annakor541@student.polsl.pl

Abstract: Nowadays, wavelets are widely used in many applications, e.g. signal processing. The application of wavelet transform allows to obtain considerably more information about technical state of machine (especially for non-stationary signals) than traditional methods, e.g. Fourier transform. The aim of the paper is to analyze the goodness of B-spline family wavelets in diagnostic signal processing. Three types of B-spline wavelets were investigated. Their applicability was verified using degree of scalogram density on synthetic and operational signals. Results of the analysis of B-spline family wavelets show that proposed approach gives more accurate results in comparison with other chosen wavelets and can be applied in industrial diagnostics.

1. INTRODUCTION

Wavelets are widely used in many branches such as molecular dynamics, astrophysics, medical sciences, image filtering, compression and recognition, signal processing, etc. They found the application thanks to their unique capabilities: limited duration, shifting and scaling. The wavelet transform (WT) in comparison with Fourier transform (FT) and short-time Fourier transform (STFT) has many advantages. First of all, it is the limited duration of support in contradistinction to the infinite support of FT and STFT. Wavelets are polymorphic: the shape of basic function one can define depending on the specific application and in the case of other above-mentioned transforms the basic function is always the harmonic one. Finally, FT has the constant resolution and WT allows the multiresolution analysis, which gives a possibility for simultaneous analysis of phenomena with significant lifetime. Using wavelet analysis there is an ability to perform the local analysis, i.e. it allows the use of long time intervals for more precise low frequency information and shorter regions for high frequency information (Misiti et al., 1996). Therefore, it can be a powerful tool for signal processing, especially for non-stationary signals.

There are many applications of WT in diagnostic signal processing with using different wavelets and wavelet families. For example, in (Timofiejczuk, 1999) was presented the application of WT for the fault detection in rotor machines using Haar, db4 and Morlet wavelets, Wysogląd proposed the method for faults identification in bearings (Wysogląd, 2009), Boczar used the high-order symlets for analyzing the acoustic emission pulses (Boczar, 2007).

The comparatively new wavelet family is the B-spline one, which is promising in usage to various applications. B-spline wavelets find an application in many different problems like local images filtering (Samavati and Mahdavi-Amiri, 2000), finite elements method (Jiawei et al., 2008), mammography (Arikidis et al., 2008), lie detectors (Abootalebi et al., 2009) and other. They can be useful according to their properties: simple analytical expressions of B-spline basic and scaling functions, symmetry and semi-orthogonality. To-date, in diagnostic signal processing B-spline wavelets were not applied.

In the paper authors want to introduce research on diagnostics signal processing using three types of B-spline wavelets – linear, quadratic and cubic (the second-, third- and fourth-order respectively). The first-order B-spline wavelet was not taken into consideration in this paper, because it is the Haar wavelet. The specific properties and exact definition of the wavelet basic functions will be formulated. Next, the capability of above-mentioned wavelets for the diagnostic signal processing will be provided using the degree of scalogram density introduced in Timofiejczuk, (1999, 2004). Then, the comparative study of B-spline wavelets and frequently-used wavelets in technical diagnostics will be carried out. Possibilities of faults detection using these wavelets will be presented.

2. PROBLEM FORMULATION

Let us consider the m-th order B-spline wavelet. The scaling function φ_m in the general case can be defined as (Ueda and Lodha, 1995):

$$\varphi_m(x) = \int_{-\infty}^{\infty} \varphi_{m-1}\varphi_1(t)dt \,, \tag{1}$$

where

$$\varphi_1(x)=\begin{cases}0 & \text{for } 0\le x<1\\ 1 & \text{otherwise}\end{cases}. \tag{2}$$

The properties of the B-spline scaling function are as follows (compact support, non-negativity, partition of unity and symmetry, respectively):

$$\begin{aligned}&1.\ \operatorname{sup}\varphi_m=[0,m]\\ &2.\ \varphi_m(x)>0 \text{ for } 0<x<m\\ &3.\ \sum_{k=-\infty}^{\infty}\varphi_m(x-k)=1\\ &4.\ \varphi_m\left(\frac{m}{2}+x\right)=\varphi_m\left(\frac{m}{2}-x\right)\quad x\in R\end{aligned} \tag{3}$$

The m-th order wavelet function ψ_m is given by

$$\psi_m(x)=\sum_{k=0}^{3m-2}q_k\varphi_m(2x-k), \tag{4}$$

where

$$q_k=(-1)^k 2^{1-m}\sum_{l=0}^{m}\binom{m}{l}\varphi_{2m}(k+1-l). \tag{5}$$

There are several properties of the B-spline basic function (compact support, symmetry and anti-symmetry and semi-orthogonality, respectively):

$$\begin{aligned}&1.\ \operatorname{sup}\psi_m=[0,2m-1]\\ &2.\ \psi_m(x)=(-1)^m\psi_m(2m-1-x)\\ &3.\ \begin{cases}\left\langle\psi_m\left(2^{j_1}x-k_1\right),\psi_m\left(2^{j_2}x-k_2\right)\right\rangle=0 \text{ if } j_1\ne j_2\\ \left\langle\psi_m\left(2^{j}x-k_1\right),\psi_m\left(2^{j}x-k_2\right)\right\rangle\ne 0 \quad \text{for } m\ne 1\end{cases}\end{aligned} \tag{6}$$

In available literature the evaluation of the goodness of wavelet approximation was not specified. For its evaluation the degree of scalogram density (DSD) was used, which must characterize the goodness of wavelet approximation considering next conditions (Timofiejczuk, 2004):

- to assume values from closed set, e.g. [0,1];
- to assume near-zero values for results of analysis, when neither component in the signal was not identified;
- to assume near-one values for results of analysis, when the component or components of the signal were identified interchangeably;
- to make possible the distinguishability between particular basic functions of wavelets.

DSD is the scalar parameter, which based on the calculations of wavelet coefficients with values greater than some non-zero threshold, determined empirically. The determination of DSD parameter consists the following steps:

- the evaluation of the maximum value in the set of wavelet coefficients;
- the normalization of the set of wavelet coefficients;
- the evaluation of the number of wavelet coefficients N, whose values are greater than the threshold value;
- the evaluation of DSD parameter using dependence (7).

$$DSD=1-\frac{N}{L}, \tag{7}$$

where L is the number of all wavelet coefficients.

3. CLOSED FORM OF THE SCALING AND BASIC FUNCTIONS FOR B-SPLINE WAVELETS

3.1. Linear B-spline wavelet

The scaling function φ_2 of the linear B-spline wavelet (LBSW) according to its recurrence definition can be expressed as (Ueda and Lodha, 1995):

$$\phi_2(x)=\begin{cases}x, & x\in[0,1)\\ 2-x, & x\in[1,2)\\ 0, & x\notin[0,2)\end{cases}, \tag{8}$$

and the basic function ψ_2 is presented by the expression:

$$\psi_2(x)=\frac{1}{6}\begin{cases}x, & x\in[0,0.5)\\ -7x+4, & x\in[0.5,1)\\ 16x-19, & x\in[1,1.5)\\ -16x+29, & x\in[1.5,2)\\ 7x-17, & x\in[2,2.5)\\ -x+3x, & x\in[2.5,3)\\ 0, & x\notin[0,3)\end{cases} \tag{9}$$

The scaling and basic functions of LBSW were presented in Fig. 1.

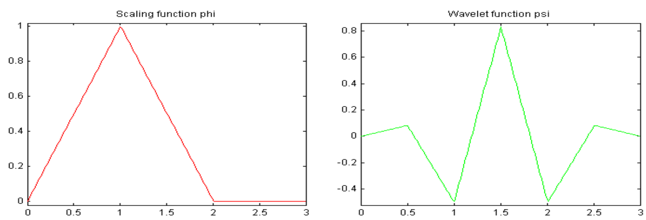

Fig. 1. The scaling and basic functions of linear B-spline wavelet

3.2. Quadratic B-spline wavelet

The scaling and basic functions of quadratic B-spline wavelet (QBSW) are presented by expressions (10) and (11) respectively. They are illustrated in Fig. 2.

$$\varphi_3(x)=\begin{cases}0.5x^2, & x\in[0,1)\\ 0.75-(x-1.5)^2, & x\in[1,2)\\ 0.5(x-3)^2, & x\in[2,3)\\ 0, & x\notin[0,3)\end{cases}, \tag{10}$$

$$\psi_3(x)=\frac{1}{240}\begin{cases} x^2, & x\in[0,0.5) \\ -8+32x-31x^2, & x\in[0.5,1) \\ 229-442x+206x^2, & x\in[1,1.5) \\ -1643+2054x-626x^2, & x\in[1.5,2) \\ 4\left(1695-1558x+352x^2\right), & x\in[2,2.5) \\ 4\left(-2705+1962x-352x^2\right), & x\in[2.5,3) \\ 7023-4206x+626x^2, & x\in[3,3.5) \\ -3169+1618x-206x^2, & x\in[3.5,4) \\ 623-278x+31x^2, & x\in[4,4.5) \\ -(-5+x)^2, & x\in[4.5,5) \\ 0, & x\notin[0,5) \end{cases}, \quad (11)$$

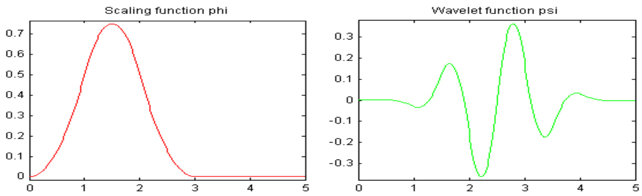

Fig. 2. The scaling and basic functions of quadratic B-spline wavelet

3.3. Cubic B-spline wavelet

The scaling and basic functions of the cubic B-spline wavelet (CBSW) are presented by expressions (12) and (13) respectively. They are illustrated in Fig. 3. In (13) the coefficients *a*, *b*, *c* and *d* are represented by Tab. 1.

Tab. 1. Coefficients for the fourth-order wavelet basic function

x	**[0,0.5)**	**[0.5,1)**	**[1,1.5)**
a	0	16/(6·7!)	721/(2·7!)
b	0	16/7!	2147/(2·7!)
c	0	32/7!	2115/(2·7!)
d	1/(6·7!)	127/(6·7!)	342/7!
x	**[1.5,2)**	**[2,2.5)**	**[2.5,3)**
a	16559/(2·7!)	145193/(2·7!)	648807/(2·7!)
b	32413/(2·7!)	210215/(2·7!)	742585/(2·7!)
c	20925/(2·7!)	100389/(2·7!)	280231/(2·7!)
d	2218/7!	15783/(2·7!)	35033/(2·7!)
x	**[3,3.5)**	**[3.5,4)**	**[4,4.5)**
a	2533050/(3·7!)	4096454/(3·7!)	1404894/7!
b	797461/7!	1096683/7!	981101/7!
c	249219/7!	291965/7!	227481/7!
d	77312/(3·7!)	77312/(3·7!)	35033/(2·7!)
x	**[4.5,5)**	**[5,5.5)**	**[5.5,6)**
a	910410/7!	706555/(2·7!)	145285/(2·7!)
b	562435/7!	391555/(2·7!)	73085/(2·7!)
c	115527/7!	72231/(2·7!)	12249/(2·7!)
d	15783/(2·7!)	2218/7!	342/7!
x	**[6,6.5)**	**[6.5,7)**	
a	11603/(2·7!)	343/(6·7!)	
b	5359/(2·7!)	49/(2·7!)	
c	825/(2·7!)	7/(2·7!)	
d	127/(6·7!)	1(6·7!)	

$$\varphi_4(x)=\frac{1}{6}\begin{cases} x^3, & x\in[0,1) \\ 4-12x+12x^2-3x^3, & x\in[1,2) \\ -44+60x-24x^2-3x^3, & x\in[2,3) \\ (4-x)^3, & x\in[3,4) \\ 0, & x\notin[0,4) \end{cases}, \quad (12)$$

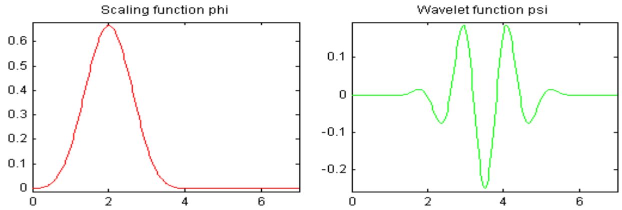

Fig. 3. The scaling and basic functions of cubic B-spline wavelet

$$\psi_4(x)=\begin{cases} dx^3, & x\in[0,0.5) \\ a-bx+cx^2-dx^3, & x\in[0.5,1) \\ -a+bx-cx^2+dx^3, & x\in[1,1.5) \\ a-bx+cx^2-dx^3, & x\in[1.5,2) \\ -a+bx-cx^2+dx^3, & x\in[2,2.5) \\ a-bx+cx^2-dx^3, & x\in[2.5,3) \\ a-bx+cx^2-dx^3, & x\in[3,3.5) \\ a-bx+cx^2-dx^3, & x\in[3.5,4) \\ -a+bx-cx^2+dx^3, & x\in[4,4.5) \\ a-bx+cx^2-dx^3, & x\in[4,5,5) \\ -a+bx-cx^2+dx^3, & x\in[5,5.5) \\ a-bx+cx^2-dx^3, & x\in[5.5,6) \\ -a+bx-cx^2+dx^3, & x\in[6,6.5) \\ -a+bx-cx^2+dx^3, & x\in[6.5,7) \\ 0, & x\notin[0,7) \end{cases}, \quad (13)$$

4. COMPARATIVE STUDY AND TESTING OF WAVELETS

4.1. Implementation of wavelets

For performing the analysis the LBSW, QBSW and CBSW obtained in closed form as piecewise expressions in Section 3. the MATLAB® Wavelet Toolbox® was used. Capabilities of this Toolbox allow to design and add own wavelets. For defining the new wavelet in MATLAB® the specific MATLAB® function must be defined. Moreover, for using the wavelet for approximation it must be added to list of available wavelets both for GUI and Command Line interfaces using Wavelet Manager functions

(Misiti M. et al., 1996). The wavelet full and short names, the wavelet type, the effective support, positions of wavelets in the family and the path to the executable function file must be defined.

In investigated cases the type 3 wavelets (wavelet with scaling function) were designed. The scaling and basic functions were implemented using expressions from Section 3. and the analysis environment was prepared.

4.2. Preliminary tests on synthetic signals

The goodness of signal component identification was evaluated using DSD. Three types of components were taken into consideration: the harmonic one, the harmonic with variable frequency (chirp) and the triangular pulse. Then, for chosen wavelets, including above discussed wavelets, DSD parameters were calculated. The threshold was set to 0.01. Results of analyses were tabulated in Tab. 2. Best results of DSD for each component were bolded. The exemplary continuous wavelet transform scalogram of synthetic signal with above-mentioned components using QBSW was presented in Fig. 4. The signal has the length of 2 seconds and the scalogram was constructed for scales parameter in the range 1÷256. As it can be noticed, all components are rather clearly detectable.

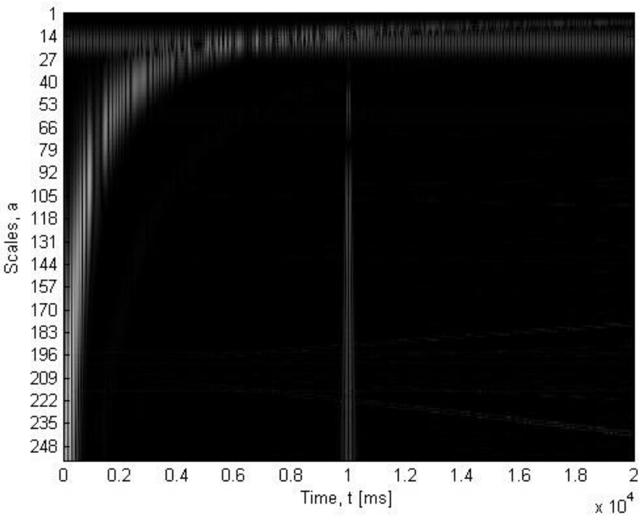

Fig. 4. Exemplary scalogram using quadratic B-spline wavelet

Tab. 2. Comparison of DSD parameters of chosen wavelets

Wavelet	Harmonic component	Pulse component	Harmonic with var. frequency
Haar	0.5903	**0.9966**	0.6651
Daubechies 4	0.8282	0.9871	0.9001
Symlet 6	0.8913	0.9838	0.9207
Meyer	0.8326	0.9733	0.8851
Gauss 1	0.8639	0.9860	0.9124
Gauss 5	0.8793	0.9835	0.9146
Gauss 6	0.8901	0.9833	0.9162
Mexican hat	0.8367	0.9876	0.8976
Morlet	0.8610	0.9837	0.8906
Linear B-spline	0.7811	0.9903	0.8802
Quadratic B-spline	0.8802	0.9895	0.9117
Cubic B-spline	**0.9000**	0.9866	**0.9211**

Analysing available literature, the group of wavelets used in the diagnostic signal processing was chosen (Tab. 2.). Gauss wavelets with different orders were chosen, because of geometrical similarity to investigated B-spline wavelets, which also presented in Tab. 2.

As it can be noticed, B-spline wavelets give good results in tests on synthetic signals. One should observe that LBSW is useful for pulse component identification and only Haar wavelet gives better result for this case. If we consider the harmonic component and the harmonic component with variable frequency best results were obtained for CBSW. QBSW also allows to rather accurate identification and can be applied for damped harmonic components considering to the geometrical similarity of their basic functions.

4.3. Application of cubic B-spline wavelet for faults identification of rolling bearings

According to passing preliminary tests by CBSW, it was applied for analysis of faults identification of rolling bearings. Analysed signals were measured and recorded on laboratory vibration stand with sampling rate 51.2 kHz. The bearing characteristic frequency for the rolling element defect equals 222 Hz (Wysogląd B., 2009). This frequency was identified using WT with different wavelets (Daubechies 4, Morlet and cubic B-spline). In Wysogląd (2009) the entropy-based approach of signal analysis was performed. In this work only continuous WT was applied to the signal processing. According to the value of the characteristic frequency the frequency range in WT analysis was limited to 300 Hz. The frequency range was defined due to the conversion to the scales parameter using the formula (Katunin and Moczulski, 2010):

$$f = \frac{5}{2\pi a}, \tag{14}$$

where a is the scales parameter.

Results of WT for the characteristic frequency identification were presented in Figs. 5-7.

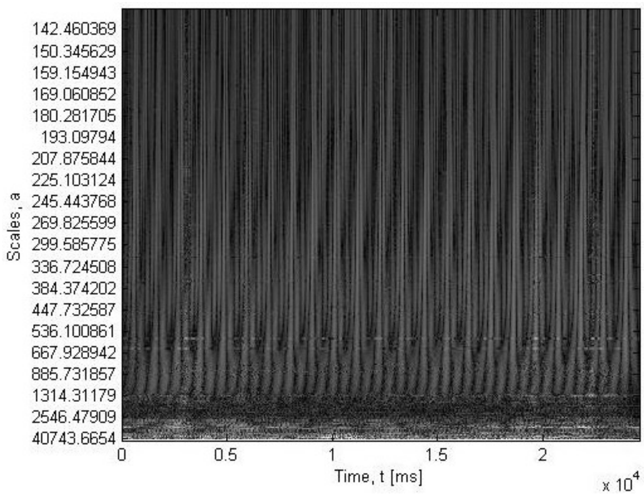

Fig. 5. Scalogram of the investigated signal using Daubechies 4 wavelet

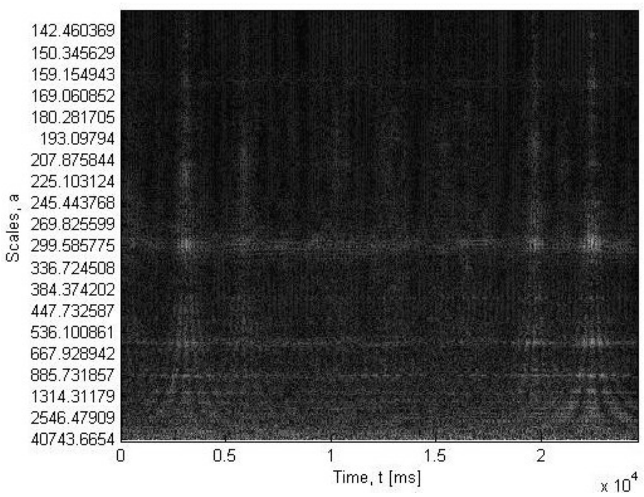

Fig. 6. Scalogram of the investigated signal using Morlet wavelet

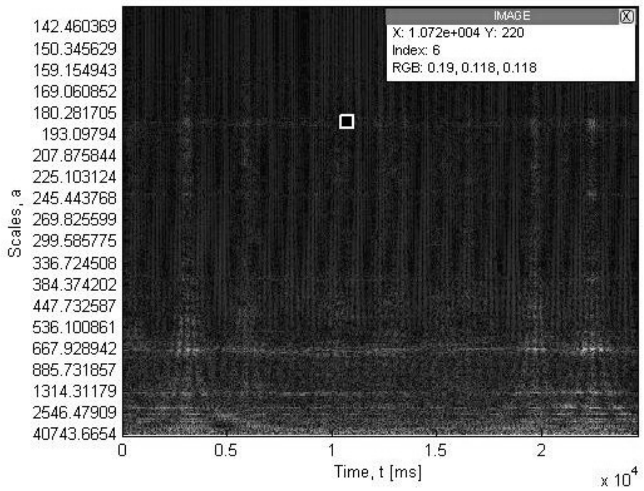

Fig. 7. Scalogram of the investigated signal using cubic B-spline wavelet

Continuous WT shows, that in the first case (using Daubechies 4 wavelet) the harmonic component we are interested in was not detected. When the Morlet wavelet was applied, harmonic and pulse components were detectable, but the characteristic frequency was almost not detectable. In the third case (when CBSW was applied) the characteristic frequency was identified. The cursor in Fig. 7 was set on the characteristic harmonic frequency and in the frame the Y value equals 220 Hz. The difference between the characteristic frequency value and obtained value can be explained by the conversion error of the scales parameter to the pseudo-frequency.

5. CONCLUSIONS AND FURTHER RESEARCH

B-spline family wavelets were investigated and possibility of their application to the diagnostic signal processing was discussed. Three cases of these wavelets were considered for the order $m = 2, 3, 4$ and the closed form scaling and basic functions was presented. For performing the analysis wavelets were implemented into MATLAB® Wavelet Toolbox®. Then, the preliminary tests were carried out for evaluating the goodness of the signal component identification using the degree of scalogram density. In tests most usable wavelets in the diagnostic signal processing were taken into consideration and compared with B-spline wavelets due to different signal components: the harmonic one, the pulse one and the harmonic with variable frequency. In the tests the continuous wavelet transform was carried out for synthetic signals. Results show, that linear
B-spline wavelet is applicable to the identification of pulse components in the signal (for other cases it gives rather poor results), the quadratic B-spline wavelet is characterised by high values of DSD and can be applied for damped harmonic components analysis according to the geometry of its basic function, and the cubic B-spline wavelet gives excellent results for harmonic components (also with variable frequency) and very good result for pulse components. Therefore, the cubic B-spline wavelet was chosen for application to the real operational signal for the faults identification problem. During continuous wavelet transform three types of wavelets were chosen for the predefined fault identification in the signal measured on the roller bearing. In the analysis only cubic B-spline wavelet identify the fault characteristic frequency with acceptable accuracy. Therefore, one can conclude, that B-spline wavelet can be a new tool in diagnostic signal processing.

In this work authors limited tests of B-spline wavelets for one case of application, which was made only for illustrating characteristics of above-discussed wavelets. In further works the application of the analysis of different types of signals will be carried out. According to the obtained results and tendency of better DSD parameters with growing the B-spline wavelet order it is planned to investigate B-spline wavelets with higher order. In present research only the continuous wavelet transform was carried out, but due to properties of B-spline wavelets they can be used also for the discrete wavelet transform and signal decomposition and reconstruction can be investigated. It gives a possibility of application of Mallat's multilevel decomposition and precise analysis on different levels of signal approximations and details.

REFERENCES

1. **Abootalebi V., Moradi M., Khalilzadeh M.** (2009), A new approach for EEG feature extraction in P300-based lie detection, *Computer Methods and Programs in Biomedicine*, 94, 1, 48-57.
2. **Arikidis N. S., Skiadopoulos S., Karahaliou A., Likaki E., Panayiotakis G., Gostaridou L.** (2008), B-spline active rays segmentation of microcalcifications in mammography, *Medical Physics*, 35, 11, 5161-5171.
3. **Boczar T.** (2007), Application of signal processing elements for the characteristics of acoustic emission pulses generated by partial discharges, *Physics and Chemistry of Solid State*, 8, 3, 610-617.
4. **Jiawei X., Xuefeng Ch., Zhengjia H., Yinghong Zh.** (2008), A new wavelet-based thin plate element using B-spline wavelet on the interval, *Computational Mechanics*, 41, 2, 243-255.

5. **Katunin A., Moczulski W.** (2010), Faults detection in layered composite structures using wavelet transform, to be published in *Diagnostyka*.

6. **Misiti M., Misiti Y., Oppenheim G., Poggi J.** (1996), *Wavelet Toolbox®. For use with MATLAB®*, The MathWorks Inc.
7. **Samavati F., Mahdavi-Amiri N.** (2000), A filtered B-spline models of scanned digital images, *Journal of Science*, 10, 4, 258-264.
8. **Timofiejczuk A.** (1999), *Methods of research of rotor machines in conditions of starting, running-up and halting*, Scientific Works of Silesian University of Technology, Mechanics, series 133, Gliwice [in Polish].
9. **Timofiejczuk A.** (2004), *Methods of analysis non-stationary signals*, Silesian University of Technology Publishing House, Gliwice [in Polish].
10. **Ueda M., Lodha S.** (1995), *Wavelets: an elementary introduction and examples*, University of California, Santa Cruz.
11. **Wysogląd B.** (2009), Application of entropy-based analysis of signals to identification rolling element bearing faults, *Diagnostyka*, 3(51), 65-68.

Authors would like to thank Dr Bogdan Wysogląd for his support.

YIELD POINT DETERMINATION BASED ON THERMOMECHANICAL BEHAVIOUR OF POLYCRYSTALLINE MATERIAL UNDER UNIAXIAL LOADING

Robert LITWINKO[*], Wiera OLIFERUK[*]

[*]Mechanical Engineering and Applied Computer Department, Bialystok Technical University,
45C Wiejska Street, 15-351 Bialystok, Poland

litwinko.r@gmail.com, wolif@ippt.gov.pl

Abstract: The paper is devoted to yield point determination based on the thermomechanical coupling that takes place in the material during its uniaxial tension. Experiments were performed on aluminum alloy and on austenitic steels. The stress value corresponding to the temperature minimum is treated as the critical resolved stress at which plastic deformation on the macroscopic scale begins. The obtained results are compared with values of stress which produces the irreversible strain equal to 0.2%. Such value of the stress is usually regarded as the yield point determined from the stress-strain curve. It is found that the values of yield point determined on the ground of the thermomechanical coupling are lower than these obtained from stress-strain curve.

1. INTRODUCTION

Some polycrystalline materials such as austenitic steels under uniaxial tension are characterized by the smooth stress-strain curve. Determination of the yield point for such materials is more difficult than for materials where the Lüders bands appear. The majority of methods applied for determining the onset of plastic deformation are based on the stress-strain curve. In tests of materials under uniaxial loading, three criteria of the initiation of yielding are used. They are: elasticity limit, proportionality limit and yield point. The elasticity limit is the greatest value of applied stress that the material can withstand without any measurable irreversible deformation. With an increase in sensitivity of strain measurement, a decrease in value of elasticity limit is obtained. Determination of the elasticity limit requires a continuous incremental loading-unloading procedure. For this reason the elasticity limit is often replaced by the proportionality one. The proportionality limit is the highest value of stress at which the applied stress is directly proportional to strain. Yield point is the stress necessary to obtain an assumed value of irreversible (plastic) strain. The assumed value is equal 0.2% (Beluch, 2002). The aim of this paper is to present the method of yield point determination that doesn't need the assumed value of irreversible strain that correspond to the yield point and to compare obtained results with the values of stress corresponding to 0.2% plastic strain. This method is based on thermomechanical coupling that takes place during unixial tension.

2. YIELD POINT DETERMINATION BASED ON THERMOMECHANICAL COUPLING

Deformation process always modifies the temperature field of a material. Under loading at adiabatic conditions temperature of sample changes. During elastic deformation of the material with positive coefficient of thermal expansion, its temperature decreases whereas during plastic deformation the temperature of tested material rises. These phenomena can be used for the determination of the yield point. Change in a material temperature during deformation is an example of a mutual conversion of the potential and kinetic energy of lattice atoms. That phenomenon of temperature variation accompanying the elastic deformation is named thermoelastic effect. This variation can be expressed by the Kelvin formula (Oliferuk, 1997):

$$\Delta T_s = -\alpha \frac{T \Delta \sigma_s}{c_\sigma}, \tag{1}$$

where: α – coefficient of linear thermal expansion, T – initial absolute temperature, c_σ – heat capacity per unit volume at constant stress, $\Delta\sigma_S$ – change of stress (change in the uniaxial Kirchoff stress tensor).

3. CONTACTLESS METHOD OF TEMPERATURE MEASUREMENT

Each body with an absolute temperature greater than 0^0K emits electromagnetic radiation in the infrared range. This radiation, named thermal one, was discovered in 1800 by Federic Herschel. Josef Stefan formulated a relation between temperature T of the black body and total radiation power of its surface as:

$$g(T) = \sigma T^4, \tag{2}$$

where σ=5.6703·10^{-8}W/m^{2}K is Stefan's constant and T is the absolute temperature of the black body (Jaworski and Piński, 1976). This result was also derived by Ludwig Boltzmann and now it is called Stefan-Boltzmann law. Note that the radiation power per unit area of the black body surface depends only on the its temperature and not on any other parameters of the object. It is a single-valued function of the temperature. Thus, the Stefan-Boltzmann law constitutes foundation of contactless methods of temperature measurement (Rudowski, 1978).

The radiation emitted by a surface of real object is dependent not only on its temperature but also on the feature of its surface. This feature is described by the quantity κ that called emissivity. Emissivity κ is the ratio of the radiation power of the real surface to the radiation power of the black body surface at the same temperature. Emissivity of the tested surface shows how much energy is emitted by the unit of the real surface during unit time period in comparison with the energy emitted by the unit of the black body surface during the same period and at the same temperature. Values of the emissivity are included in range from 0 to 1.

Thus Stefan-Boltzmann law for real surface has a form as follows (Jaworski and Piński,1976):

$$E = \kappa g\left(T\right) = \kappa\sigma T^4, \tag{3}$$

where E is radiation power emitted by unit surface of the κ emissivity at T temperature.

Infrared radiation is measured by an IR detector that is a main part of IR Thermographic System. The signal S on the IR Thermographic System out-put includes two parts: one is generated by IR radiation emitted by the tested object and another one caused by the surroundings IR radiation (Oliferuk, 2008):

$$S = \kappa f(T_0) + (1-\kappa) f(T_a), \tag{4}$$

where: T_a is the absolute ambient temperature, T_0 is the absolute object temperature, $(1\text{-}\kappa)f(T_a)$ is a signal as a function of an ambient temperature, $\kappa f(T_0)$ is a signal as a function of the object temperature.

The temperature of the tested surface can be measured when the value its emissivity, ambient temperature and calibration curve of IR Thermographic Systems are known. Usually the tested surface is covered with soot, because the emissivity of the soot is known and equals to 0.95.

Let us note that method of temperature measurement based on detection of IR radiation is non-destructive. Up-to-date IR Thermographic Systems enable to determine surface temperature distribution. A such kind of System was used in the presented work.

4. EXPERIMENT PROCEDURE AND RESULTS

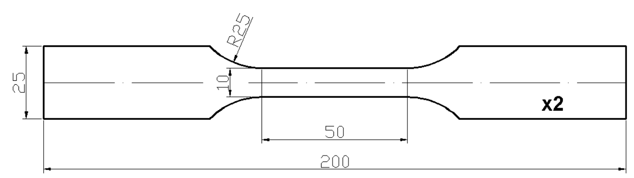

Fig. 1. Shape and dimensions of specimens

The experiments were performed on specimens made from austenitic steels and aluminum alloy (Tab. 1). The shape and dimensions of the specimens are shown in Fig. 1.

Tab. 1. Specimens used in experiments

Specimen	Material	Symbol	Chemical composition
1	austenitic steel	00H19N17 (304)	Cr19%Ni17%
2	austenitic steel	00H17N14M2 (316 L)	Cr17%Ni14%Mo2%
3	aluminium alloy		Si8%Cu3%

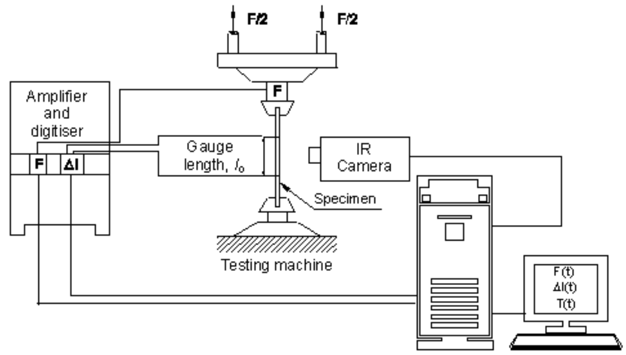

Fig. 2. Experimental set-up used for determination of yield point

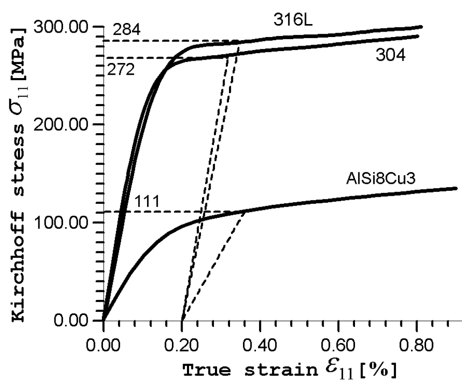

Fig. 3. Stress-strain curve for tested materials and procedure of the yield point determination

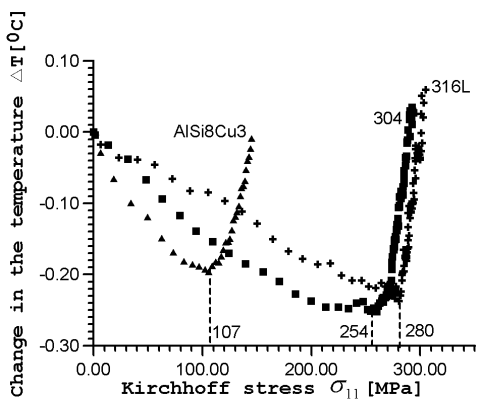

Fig. 4. The dependencies of the change in the specimen temperature versus stress in early stage of tension

All specimens were strained using the MTS testing machine with constant strain rate equal $5{\cdot}10^{-3}$ s^{-1}. During the tensile test the temperature distribution on the surface of the specimen was measured by IR camera. Simultaneously, the stress and strain were determined as a function of the deformation time.

In order to obtain an uniform emissivity of the tested specimen surface and to enhance method sensitivity the specimen surfaces were covered by the sooth.

Schematic diagram of the experimental set-up designed for determination of yield point is shown in Fig. 2.

The frequency of thermal image, stress and strain recording was equal 50 Hz.

Fig. 3 shows the typical stress-strain curves for the tested materials. From these stress-strain curves, the yield point as the stress corresponding to plastic strain ε_p=0.2% was determined for each material (Fig. 3).

On the basis of the stress and the temperature experimental data, the dependence of the change in the specimen temperature vs. stress was determined (Fig. 4).

It is seen that, with growing stress, the specimen temperature decreases, reaches minimum and then starts to rise rapidly. It can be assumed that the specimen heating due to micro-plastic deformation before the temperature minimum is negligible small. Consequently, the stress value corresponding to the temperature minimum can be treated as the critical resolved stress at which plastic deformation on the macroscopic scale begins (Fig. 4) (Kuo et al., 2005; Lee and Shaue, 1999).

5. CONCLUSIONS

The values of yield point determined by two different methods are shown in Tab. 2. It is seen that the values of yield point determined on the ground of the thermomechanical coupling are lower than these obtained from stress strain-curve (Tab. 2, Fig. 5, Fig. 6, Fig. 7). Method based on thermomechanical coupling is more precise.

Tab. 2. Yield point values obtained from thermomechanical coupling and from stress-strain curve.

Material	Yield points obtained from thermomechanical coupling analysis [MPa]	Yield points obtained from tress-strain curve [MPa]
304	254	272
316L	280	284
Al	107	111

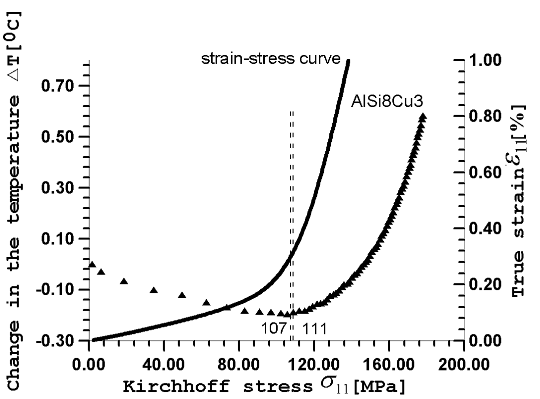

Fig. 5. Strain-stress curve and change in the temperature-stress for aluminum in early tension stage.

The method based on thermomechanical effect is especially useful for materials in which Lüders bands don't appear and for materials with non-linear elasticity. It should been emphasized that the instant at which the temperature reaches the minimum can be found more precisely than the point when the stress-strain curve ceases to be the straight-line. We can see it clearly in Fig. 5.

It should be noted that the presented method is based on physical phenomena connected with energy conversion in the deformed material. The method doesn't need the assumed value of plastic strain.

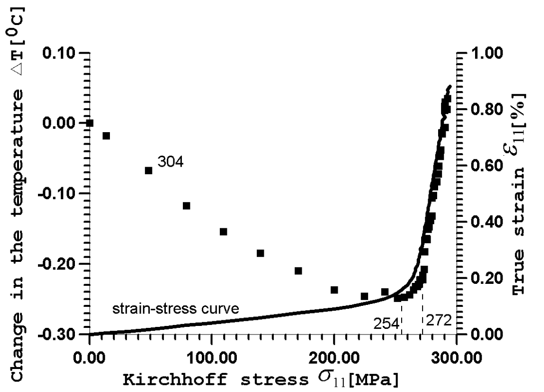

Fig. 6. Strain-stress curve and change in the temperature-stress for 304 steel in early tension stage

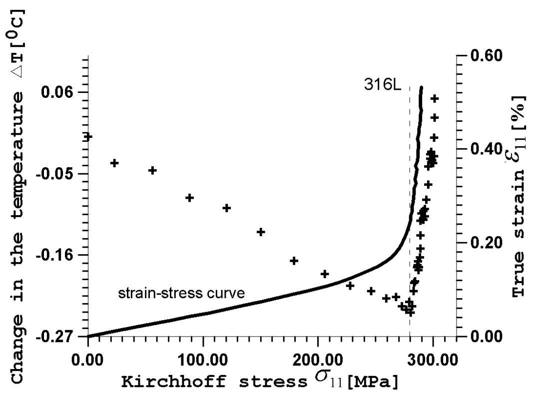

Fig. 7. Strain-stress curve and change in the temperature-stress for 316L steel in early tension stage

REFERENCES

1. **Beluch W.** (2002), *Laboratorium z wytrzymałości materiałów*, Editors: Tadeusz Burczyńsk, Witold Beluch, Antoni John Wydawnictwo Politechniki Śląskiej, Gliwice.
2. **Jaworski B. M. Piński A. A.** (1976), *Elementy fizyki* v1, PWN. Warszawa.
3. **Kuo T.Y., Lin H.S., Lee H.T.** (2005), *The relationship between of fracture behaviors and thermomechanicaleffects of alloy AA2024 of T3 and T81 temper designations using thecenter crack tensile test, Sci. Eng.*, A394 28-35.
4. **Lee H. T., Shaue G. H.** (1999), *The thermomechanical behavior for aluminum alloy under uniaxialtensile loading, Mater. Sci. Eng.*, A268 154-164.
5. **Oliferuk W.** (1997), *Proces magazynowania energii i jego strukturalny aspekt podczas jednoosiowego rozciągania stali austenitycznej*, Prace IPPT PAN, 17, Warszawa.
6. **Oliferuk W.** (2008), *Termografia podczerwieni w nieniszczących badaniach materiałów*, Wydawnictwo Gamma, Warszawa.
7. **Rudowski G.** (1978), *Termowizja i jej zastosowania*, WNT.

THE CONTROL SYSTEM OF THE FLYWHEEL ENERGY STORAGE

Stanisław PIRÓG*, Tomasz SIOSTRZONEK*, Marcin BASZYŃSKI*, Jarosław CZEKOŃSKI*

*AGH University of Science and Technology, Faculty of Electrical Engineering, Automatics, Computer Science and Electronics, Al. Mickiewicza 30, 30-059 Kraków, Poland

pirog@agh.edu.pl, tsios@agh.edu.pl, mbaszyn@agh.edu.pl, czekon@agh.edu.pl

Abstract: In this article authors described the control system for Flywheel Energy Storage. The device consists of the power electronic system and control system. The control system based on the FPGA. The power electronic system consists of the special rectifier and converter.

1. INTRODUCTION

The paper presents an experimental investigation of a flywheel energy storage system. The device is based on a flywheel concept and stores mechanical energy. This device contains a brushless DC motor supplied by an electronic commutator. A steel barrel performs the function of the flywheel. From the power network side this device is perceived as the unity power factor load. This is achieved owing to the use of the rectifier with sinusoidal source current. Energy storage is one of the main problems of contemporary technology. Currently, the following methods for energy storage are used:

– magnetic accumulator – the energy is kept in the magnetic field of a superconductive induktor;
– battery with supercapacitors – its disadvantage is the low voltage (1,8-2,4V);
– battery with lead-acid or alkaline cells; the disadvantage of this solution is a very low charging and discharging efficiency;
– electromechanical accumulator – flywheels store energy mechanically in the form of the kinetic energy.

2. FLYWHEEL ENERGY STORAGE

Stored energy, in Flywheel Energy Storage, depends on moment of inertia of the rotor and the square of the rotational speed of the flywheel. The moment of inertia depends on the radius, mass and height (length) of the rotor. Energy is transferred to the flywheel, when the machine operates as motor, charging the energy storage device. The flywheel is discharged when the electric machine regenerates through the drive.

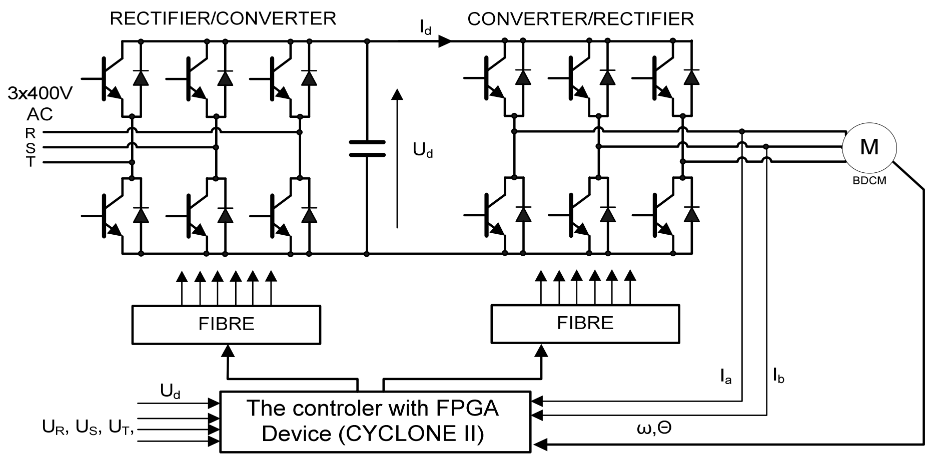

Fig. 1. The scheme of the FES supply system

3. POWER ELECTRONIC SYSTEM

Power electronic converters consist of two circuits: a control system (measuring sensors, controllers, PWM sections, dead time elements, contactors and pushbuttons control, protection algorithms, algorithms for the system control in specific operation modes, e.g. system starting) and a power circuit (power semiconductor devices, passive LC elements, contactors).

Three phase rectifier is a part of Power Electronic system for supply of brushless DC motor (BLDCM). In this device the three phase transistor converter which worked as a rectifier with sinusoidal source current was introduced. Additionally, bidirectional power flow (possibility of energy return from drive system to supply system) and DC voltage stabilization was possible. The converter, supplying the machine, was constructed on the basis on 3rd generation Intelligent Power Module (PM50RLA120) with integrated gate drive and brake-control. The PWM with unipolar voltage switching was used in inverter, which resulted in following advantages:

– reduction of the switching losses in the transistor;
– reduction of the ripple voltage with switching frequency.

The control system was constructed on the basis of a FPGA–CYCLONE II (Altera). In Fig 2 the realization of the switching transistors in converter is shown. The signals Sa, Sb, Sc are received from the Hall Sensors.

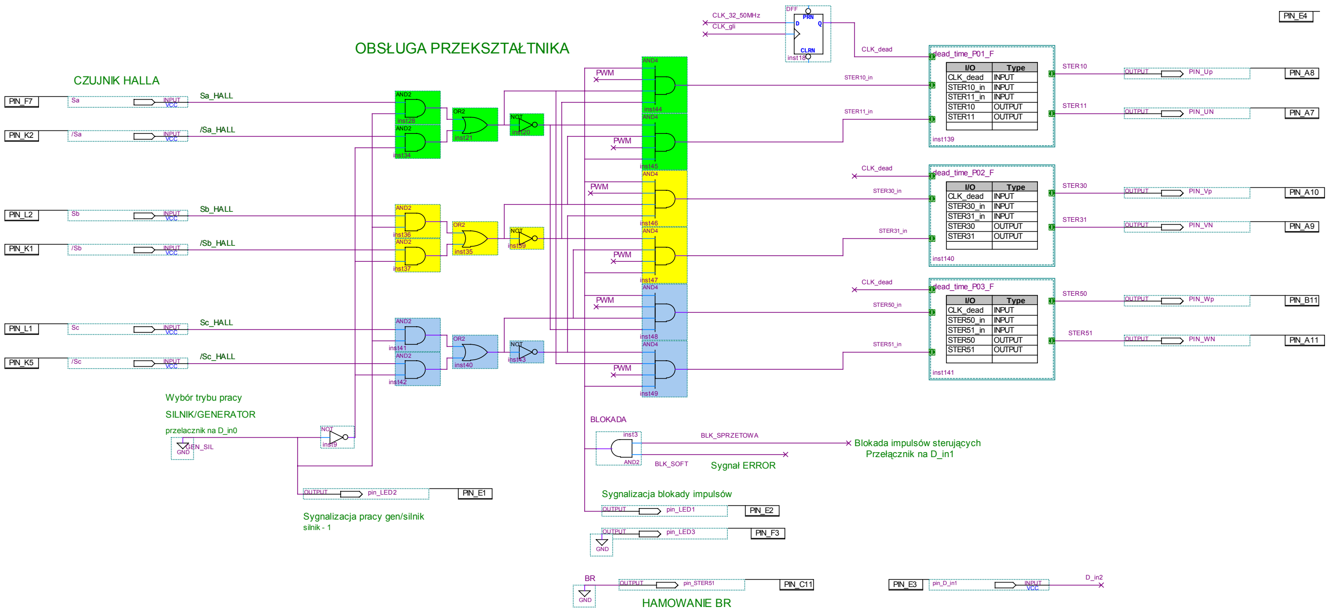

Fig. 2. The control system of the converter in Cyclone II (QUARTUS)

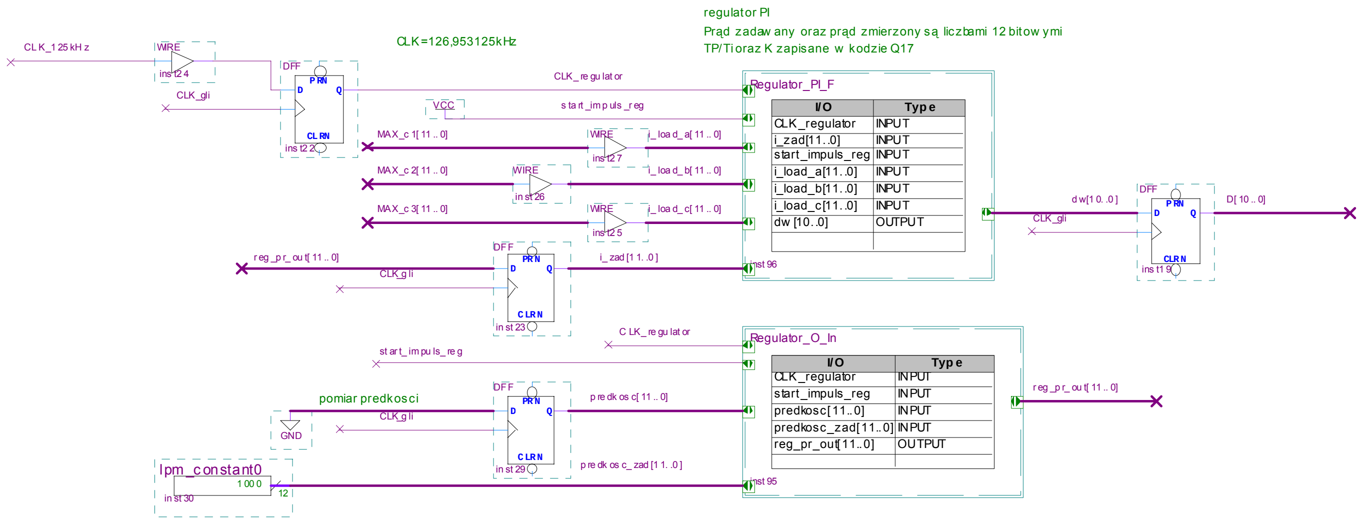

Fig. 3. The diagram of the control system in QUARTUS

Field Programmable Gate Arrays (FPGA) are now commonly applied to control and signal analysis systems. FPGAs hardware resources (logical elements, DSP modules, memories and PLLs) are used in building converter system elements capable of simultaneously executing several real-time algorithms. The paper presents FPGAs application opportunities, illustrated with actual applications in converter systems control. A method for real-time simulation of control systems implemented in FPGA elements, is also presented in this paper. The method utilizes the FPGA computing parallelism and is dedicated for rapid, safe and cheap prototyping of physical processes controllers, as well as control and protection algorithms, e.g. for power electronic converters.

CYCLONE II EP2C20:
Features:

The Cyclone II offers the following features:

- high-density architecture with 18,752 Les;
- M4K embedded memory blocks;
- 4,096 memory bits per block (4,608 bits per block including 512 parity bits);
- variable port configurations of ×1, ×2, ×4, ×8, ×9, ×16, ×18, ×32, and ×36;
- up to 260-MHz operations;
- embedded multipliers;
- 18- × 18-bit multipliers are each configurable as two independent 9- × 9-bit multipliers with up to 250-MHz performance;
- optional input and output registers;
- advanced I/O support;
- 315 I/O pins;
- single-ended I/O standard support, including 2.5-V and 1.8-V, SSTL class I and II, 1.8-V and 1.5-V HSTL class I and II, 3.3-V PCI and PCI-X 1.0, 3.3-, 2.5-, 1.8-, and 1.5-V LVCMOS, and 3.3-, 2.5-, and 1.8-V LVTTL;
- four PLLs per device provide clock multiplication and division, phase shifting, programmable duty cycle, and external clock outputs, allowing system-level clock management and skew control.

In Fig. 1 the diagram of power electronic system with control system is shown. The analog signals (current) were measured by LEM sensors. The analog signals were converted by fast 12-bits A/D converters. The MAX1309 is a 12-bit, analog-to-digital converters (ADCs) offer eight independent input channels. Independent track-and-hold (T/H) circuitry provides simultaneous sampling for each channel. The MAX1309 provide a ±5V input range with ±16.5V fault-tolerant inputs. ADCs convert two channels in 0.9µs, and up to eight channels in 1.98µs, with an 8-channel throughput of 456ksps per channel. Other features include a 20MHz T/H input bandwidth, internal clock, internal (+2.5V) or external (+2.0V to +3.0V) reference, and power-saving modes. A 20MHz, 12-bit, bidirectional parallel data bus provides the conversion results and accepts digital inputs that activate each channel individually. All devices operate from a +4.75V to +5.25V analog supply and a +2.7V to +5.25V digital supply and consume 57mA total supply current when fully operational.

Most computations (the rotor position, actual speed, current error, regulators) are carried out by CYCLONE II. Output data, in the form of transistor's driving pulses, are fed back to the FPGA structure, where control logic was generated allowing for safe switching of transistors in the inverter's branch. The current regulation of BLDC motor can be worked out in the same way as for classic DC machine with separately excited, by means of PI controller. The feedback signal for PI controller is a signal, which is proportional to current wave (absolute value Id) of DC source.

This signal can be received:

a) directly from DC current sensor (as absolute value of DC source current);
b) as signal proportional to the sum of module of load phase AC current.

The control algorithm is implemented in CYCLONE II. In Fig. 3 the scheme of the control system, where the signal in control loop is proportional to the sum of absolute value of load phase AC current, was shown.

4. THE PRACTICAL RESULTS

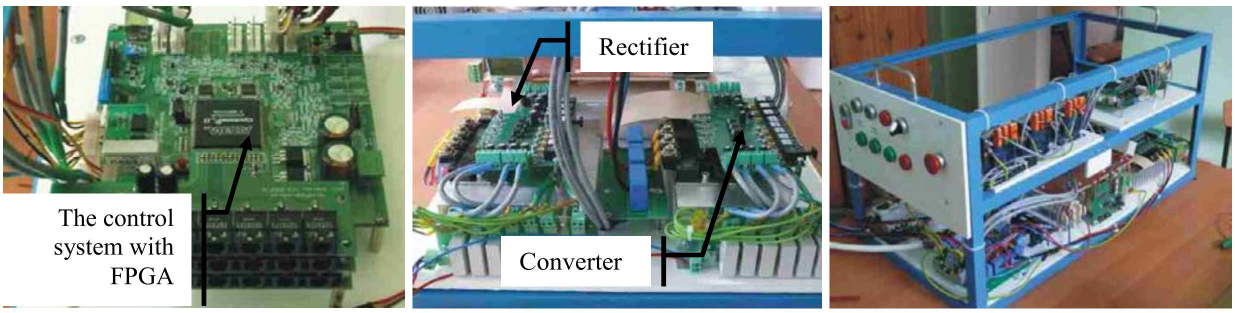

Fig. 4. The appearance of supply and control system of FES

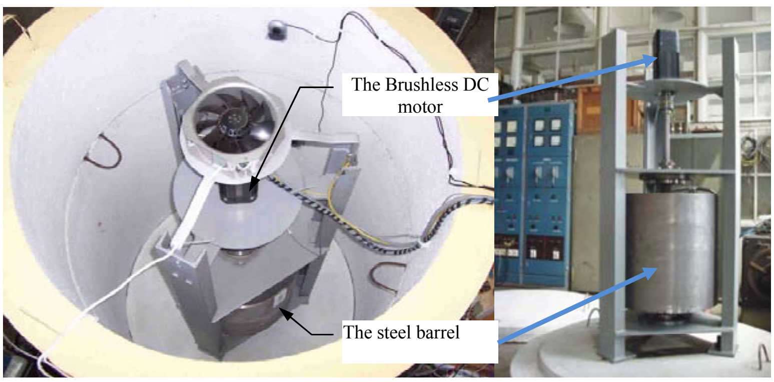

Fig. 5. The appearance of the FES

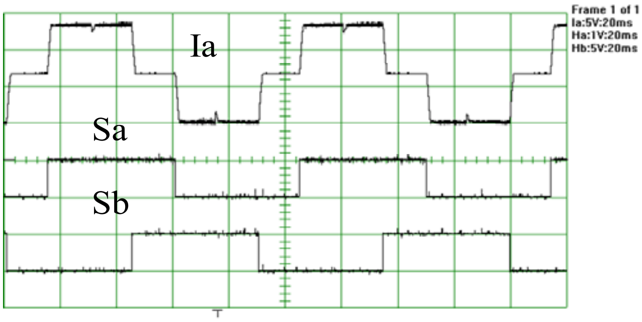

Fig. 6. The phase current and the Hall sensors signals

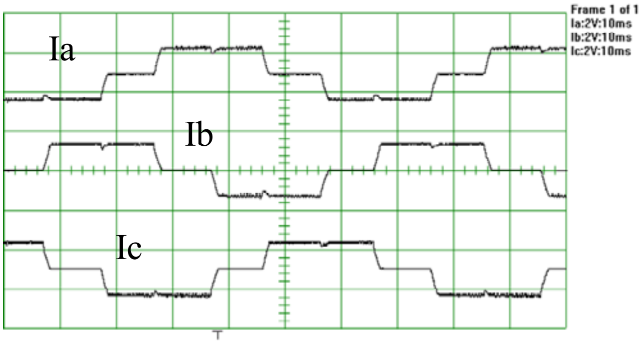

Fig. 7. The waves of phases current

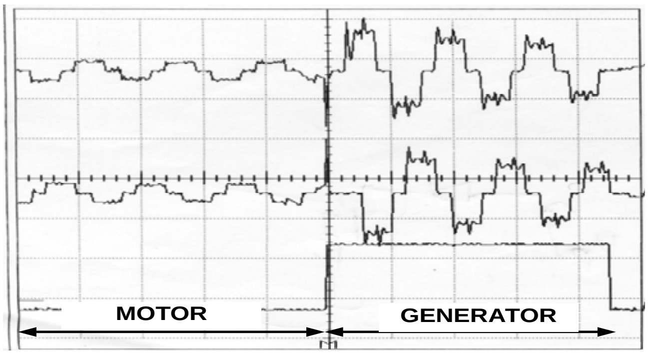

Fig. 8. The phase current waves. Motor and generator work

In Fig. 7 the waves of phases in the BLDC motor are shown. The rotor position is calculated on the basis of Hall sensors signals. In the Fig. 6 the signals from Hall sensors and phase current are shown. Above figures illustrate relationship between these waves. In the Fig. 8 the work as generator and motor work are shown (charging and discharging of FES).

5. CONCLUSION

Description and practical test results of the Flywheel Energy Storage System were presented. The system was developed on the basis of two power electronic devices: the rectifier with sinusoidal source current and the power electronic commutator for the brushless DC motor. The research on the Flywheel Energy Storage has proved that energy storage in the form of kinetic energy is highly efficient. The maximum speed of the barrel used in this research is limited. The current waves in real circuit are of better quality than the simulation results. The future research will concentrate on the control system based on FPGA only. The IPM of 5th generation with lower losses will be used in the inverter.

REFERENCES

1. **Chen H. C., Liaw C. M** (2002), Current-Mode Control for Sensorless BDCM Drive With Intelligent Commutation Tuning, *IEEE Trans. on Power Electronics*, Vol. 17, No. 5, 747-756.
2. **Dixon J. W., Leal I. A.** (2002), Current control strategy for brushless DC motors based on a common DC signal, *IEEE Trans. on Power Electronics*, Vol. 17, No. 2, 232-240.
3. **Lai Y., Shyu F., Tseng S.** (2003), New initial position detection technique for three-phase brushless DC motor without position and current sensors, *IEEE Trans. on Industry Application*, Vol. 39, No. 2, 485-491.
4. **Piróg S., Siostrzonek T.** (2004), *Current Control of Sensorless Brushless DC Motor on the Basis of a Common DC Signal – Computer Simulation Results*, EPE-PEMC, Riga.

Acknowledgement: This work is supported by Polish Ministry of Science and Information Society Technologies under project PBZ-KBN-109/T10/2004 in period 2006-2009.

DETERMINING THE UNCERTAINTY OF THE OBJECT COORDINATE SYSTEM POSITION IN COORDINATE MEASUREMENTS OF FREE-FORM SURFACES

Małgorzata PONIATOWSKA*

*Faculty of Mechanical Engineering, Bialystok Technical University, ul. Wiejska 45 C, 15-351 Bialystok

mponiat@pb.edu.pl

Abstract: Coordinate measurements are a source of digital data in the form of coordinates of measurement points with a discrete distribution on the measured surface. Geometric deviations of free-form surfaces are determined at each point as normal deviations of these points from the nominal surface (a CAD model). The calculations are preceded by fitting the measurement data to the CAD model. The relations between the object coordinate system and the coordinate system of the machine are described by the transformation parameters. This paper presents the idea of the process of data fitting with the use of the least square algorithm method as well as the way of determining the uncertainty on the assumption that transformation parameters are subject to a multivariate normal probability distribution. The theoretical issues were verified by experiments carried out on a free-form surface obtained in the milling process and characterised by random geometric deviations.

1. INTRODUCTION

Computer-aided measurement techniques tend to dominate in measuring geometric dimensions connected with machine parts. These techniques involve determining the coordinate values of measurement points situated (using a touch or non-touch system) on the object surface. As the result of the measurement, a set of discrete data is obtained. From the point of view of CAD/CAM techniques, the most important feature of coordinate measurements is providing data concerning the object in the digital form.

A typical machine part geometry is described with simple geometric shapes: straight lines, planes, circles, cylinders, etc. In coordinate measurements, macroinstructions built in software are used; on the basis of the coordinates of measurement points, first geometric associated features, and later their dimensions and shape and location deviations, are determined. The accuracy inspection is reduced to comparing the determined dimensions with the data contained in construction drawings.

Growing demands concerning product functionality, ergonomics, and aesthetics, force creating machine parts composed of 3D curvilinear surfaces. Such parts are shaped by surfaces which cannot be described with simple mathematical equations. The accuracy inspection involves digitalising the measured object (coordinate measuring with the use of the scanning method) and later comparing the ob-tained measurement points coordinates to the CAD design (model). At each measurement point, geometric deviations, or the distances of these points from their projections on the nominal surface, are determined. The processing accuracy inspection results may be presented in the form of a three-dimensional plot or a deviation map.

The majority of problems in the coordinate measurement technique theory results from the discrete character of measurement data. These problems might be divided into two categories:

- different calculation algorithms produce different measurement results for the same set of data;
- different sampling strategies (number and location of measurement points) provide different measurement results for the same surface regardless of applying the same calculation method.

The latter problem category is connected to the fact of measuring a finite number of discrete points on the measured surface described actually with an infinite number of points. Since geometric deviations are different at each point, measurement results depend on the number and location of these points. For the same reason, the number and location of points influence determining geometric features which form the basis of the object coordinate system (Feng et al., 2007; Dhanish and Mathew, 2006; Yau, 1998; Rajamohan et al., 2007). The surface geometric deviations variability is therefore the source of uncertainty in determining the object coordinate system. Consequently, the values of measurement points coordinates determined in this system (and thus the values of geometric deviations) are also characterised by this uncertainty.

Before determining geometric deviations of regular surfaces it is necessary to determine an associated feature from the obtained data. In measuring such surfaces composed of typical geometric features (circles, cylinders, cones, etc.), one of the four methods of determining associated features might be applied (Ratajczyk, 2005). However, it is not possible to determine nominal shapes of curves and free-form surfaces out of measurement data. Processing and measuring these types of surfaces are performed on numerical control devices, using the information on nominal shapes, included in the imported CAD model, to create controlling programmes. For the above mentioned reasons, software of coordinate measurement machines best-fits obtained data to the nominal surface (CAD model), and the least square method is the most often used method here (Yau and Menq, 1996). The idea of this process is described in Chapter 2.

This paper presents the idea of determining the limits of the uncertainty of the coordinate system location of a object determined in the process of fitting data to the nominal surface with the least square method. The experiments were performed on a free-form surface characterised by random geometric deviations.

The experiments were carried out with the use of a MISTRAL STANDARD 070705 coordinate measuring machine equipped with a Renishaw TP200 touch trigger probe with a stylus of 20mm in length, with a ball tip of 2mm in diameter, MPE_E=2,5+L/250.

2. IDEA OF FITTING MEASUREMENT DATA

An ideal (nominal) shape of a surface part might be described with the *N(p)* shape function, where *p* is the set of parameters describing the surface. After the object has been made, its real shape might be described as follows:

$$M(p) = N(p) + \varepsilon(p) \tag{1}$$

where: *M(p)* – the real shape of a surface part, *ε(p)* – geometric deviations.

In coordinate measurements, the coordinates of measurement points are determined on the real surface in the machine coordinate system. The determined coordinates of the *i*-th point on the *M(p)* surface might be described as follows:

$$X_i = T(t)M_i(p) + e_i \tag{2}$$

where: *T(t)* – transformation matrix between the object coordinate system and the machine coordinate system, *t* – transformation, rotation and translation parameters, e_i – measurement error.

If the measurement errors are small when compared to the geometric deviations of the measured object surface, the geometric deviation at each measurement point might be calculated from the following dependence (3):

$$\varepsilon_i(t) = X_i - T(t)N_i(p) \tag{3}$$

where: $\varepsilon_i(t)$ – geometric deviations in the machine coordinate system, $N_i(p)$ – the X_i measurement point projection on the *N(p)* nominal surface in the machine coordinate system.

As it was already mentioned, in measurements performed in the CAD environment, best-fit algorithms of coordinate measuring machines software carry out the operation of fitting the measurement data to the nominal surface (CAD model), or:

$$\varepsilon_i(p) = T^{-1}(t)X_i - N_i(p) \tag{4}$$

where: $T^{1}(t)X_i$ – measurement point coordinates in the object system, $N_i(p)$ – the $T^{-1}(t)X_i$ transformed point projection on the nominal surface, $\varepsilon_i(p)$ – geometric deviation at the measurement point, determined in the object coordinate system.

Before determining geometric deviations it is necessary to establish the transformation matrix which is a function of a three-dimensional rotation and translation (Kiciak, 2000; Yau and Menq, 1996). When applying the least square method to data fitting, the following function *F* should be minimised:

$$F = \sum_{i=1}^{m} \varepsilon_i(p)^2 = \sum_{i=1}^{m} \left| T^{-1}(t)X_i - N_i(p) \right|^2 \tag{5}$$

where: *m* – the number of measurement points.

The fitting effect depends on each of the points selected to establish the transformation matrix. Because of the presence of geometric deviations at each point, different numbers and locations of points result in different fitting effects and thus different locations of the object coordinate system, which means they influence the relations between the object coordinate system and the machine coordinate system (the transformation matrix). Consequently, different values of geometric deviations at each measurement point are obtained for different sampling strategies. This is illustrated in Fig. 1 which shows the outlines of geometric deviations of the milled free-form surface for three different sets of data used to perform the process of fitting the measurement data to the CAD model. As the result of surface scanning, coordinates of 1500 measurement points were obtained. From the scanned data set, three sets of points of different numbers and locations were selected. After having performed the process of fitting these points to the CAD model, the surface geometric deviations were determined. The differences in the deviations values and their distribution contours on the surface are clearly visible.

Minimising the *F* function, the *T(t)* transformation matrix between the object coordinate systems and the machine coordinate systems is determined according to the dependence (5). This is a 4 x 4 matrix in the form (Yau and Menq, 1996; Kiciak, 2000):

$$T(t) = \begin{bmatrix} & R & & \vec{P} \\ 0 & 0 & 0 & 1 \end{bmatrix} \tag{6}$$

where: *T(t)* – transformation matrix between the object and the machine coordinate systems, *t* – transformation, rotation and translation parameters vector, *R* – 3 x 3 rotation matrix, $R(t\alpha, t\beta, t\gamma)$, $t\alpha$, $t\beta$, $t\gamma$ axis rotation angles, $\vec{P}$ – translation vector between the origins, $\vec{P} = [tx, ty, tz]^T$.

A transformation matrix (6) is a combination of rotation and translation, and in general case it has six degrees of freedom, and the transformation parameters set (vector) can be described as $t=[tx,ty,tz,t\alpha,t\beta,t\gamma]$. For 3D axis-symmetrical surfaces the number of parameters is smaller. For example, for a cylinder and a cone it amounts to 5 (three translation vector components and two rotation vector components). In the case of a 2D surface there are two translation components and one rotation angle. In the specific case of a 2D circle (an axis-symmetrical shape), the transformation parameters vector has two components (these of translation).

a)

b)

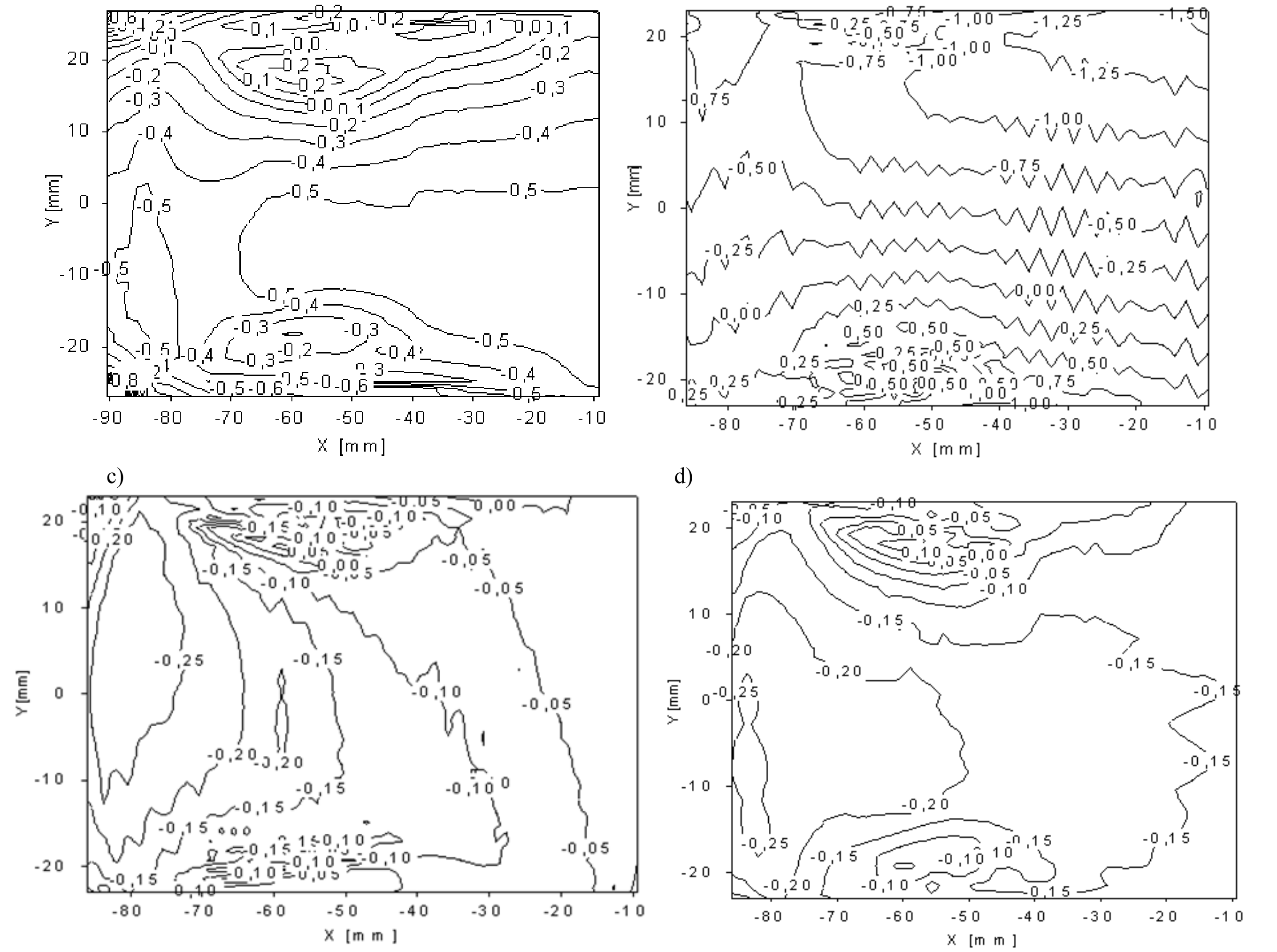

Fig. 1. Contour graphs of geometric deviations: a) before best fitting, b) after best fitting of 15 points, c) after best fitting 108 points, d) after best fitting 1500 points

3. TRANSFORMATION PARAMETERS DISTRIBUTION

The location and orientation of the object coordinate system in relation to the machine coordinate system is described with the *T(t)* transformation matrix. The object coordinate system location is obtained after applying the procedure of fitting the scanned measurement data to the nominal surface. Different sampling strategies result in scattering of the object coordinate system location and orientation, and in variability of transformation matrix parameters, or fitting uncertainty. Fitting uncertainty is therefore inseparably connected with the values and distribution of the object processing errors as well as with the number of measurement points.

Surface geometric deviations are attributed to many factors. Different sources of errors in the production process leave traces on the surface, and deviations are the cumulative effect of the influence of these sources. Geometric deviations may be divided into three components: shape deviations, waviness, and roughness. Components connected with shape deviations and waviness are strongly correlated and are usually deterministic in character. Surface roughness means irregularities of great frequency; in the context of the distance between measurement points it might be assumed that they are random in character. The share of random phenomena on a surface depends on the machining type. The literature shows that after precision milling, values of random geometric deviations of the surface are greater than these of deterministic deviations.

If random surface geometric deviations have normal distribution, for a big enough number of measurement points assumed as the transformation base, it can be assumed that the transformation parameters are random variables of normal distribution. In a border situation, for an infinite number of measurement points, the expected values of transformation parameters describing the location of the coordinate system of the specific measured surface will be obtained. Consequently, the distributions of transformation parameters deviations from the expected values are also normal (Chapter 5).

In general case, the multivariate normal distribution of many variables has the following form (Kotulski and Szczepiński, 2004):

$$f(x_1,...,x_n) = \frac{1}{\sqrt{(2\pi)^n \det[\lambda]}} \exp\left[-0{,}5(x-\mu)^T \lambda^{-1}(x-\mu)\right] \quad (7)$$

where: λ – n x n covariance matrix, $x=[x_1 ,..., x_n]$ – the independent random variables vector of normal distributions, $\mu=[\mu_1,..., \mu_n]^T$ – the expected values vector.

For the case of analysing the joint distribution $f(\Delta t)$ of the vector of transformation parameters deviations centred around the expected values ($\mu = 0$), the above dependence (7) can be illustrated as follows:

$$f(\Delta t) = \frac{1}{\sqrt{(2\pi)^n \det[\lambda]}} \exp\left[-0{,}5(\Delta t)^T \lambda^{-1}(\Delta t)\right] \qquad (8)$$

where: λ – 6 x 6 covariance matrix, $\Delta t= [dx,dy,dz,ax,ay,az]$ – the vector of transformation parameters deviations from their expected values.

Variability of the parameters deviations vector is connected with equal probability (probability concentration) surfaces described by equation (9):

$$(\Delta t)^T \lambda^{-1}(\Delta t)=\eta^2 \qquad (9)$$

where: η – the constant dependent on the assumed probability.

These surfaces have the shapes of hyperellipsoids whose centres are determined by the expected values vector.

The directions of the hyperellipsoids axes determine eigen (unit) vectors of the covariance matrix, and the squared lengths of the semi-axes – the corresponding eigen values of the covariance matrix.

The eigen vectors and values of a covariance matrix might be obtained by decomposing this matrix (10) (matrix properties allow for this).

$$\lambda = U\Lambda U^T \qquad (10)$$

where: U – matrix whose columns are the covariance matrix eigen vectors, Λ – diagonal matrix of the covariance matrix eigen values.

The hyperellipsoid size is dependent on the assumed probability, and the constant η value is determined from the chi-square distribution, in this case for six degrees of freedom (Kotulski and Szczepiński, 2004).

The aim of the procedure is to determine the fitting uncertainty, or the scatter limits of the Δt transformation parameters deviations vector from the expected values of these parameters vector for a specific probability. The limits are in the shape of hyperellipsoids contours whose centres are located in the point determined by the expected values vector; the object coordinate system origin (transformation parameter vector) will be found in the space limited by them with the assumed probability.

4. MEASURED SURFACE CHARACTERISTICS

The experiments were performed on a free-form surface obtained in a three-stage milling process. In the last stage (profiling), the following parameters were applied: a ball-end mill of 6 mm in diameter, rotational speed equal to 7500 rev/min, working feed 300 mm/min and zig-zag cutting path in the XY plane

The surface was subsequently scanned with the UV method, 2500 (50 rows and 50 columns) uniformly distributed measurement points were scanned from the surface (Fig. 2), and the process of fitting the data to the nominal surface was then carried out in which the least square method was applied and all the measurement points were used.

Geometric deviations of a free-form surface, or normal deviations of measurement points from the nominal surface, might be calculated after previously determining the deviations components in the x,y,z directions (Werner A., Poniatowska M., 2006). Coordinate measuring machines software automatically performs such calculations for each measurement point in the UV scanning option.

The first stage consisted of making a detailed characteristics of the measured surface which meant determining the values and character of the obtained deviations ε. The surface was characterised by deviations whose statistical parameters shows Tab. 1 and map is illustrated in Fig. 3, and the standard deviation of the geometric deviations from the nominal surface amounted to 0.0047 mm. Fig. 4 shows the geometric deviations probability distribution. It can be assumed that the values of geometric deviations undergoes a normal probability distribution.

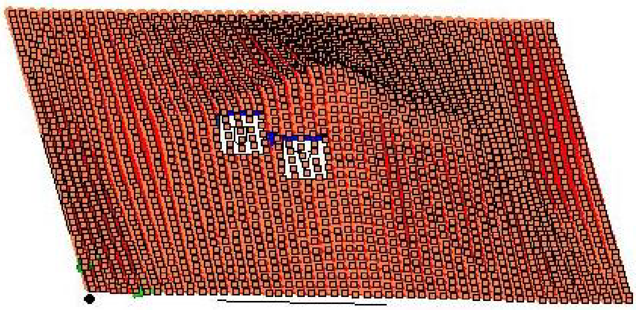

Fig. 2. Measurement points distribution on CAD model (CMM software)

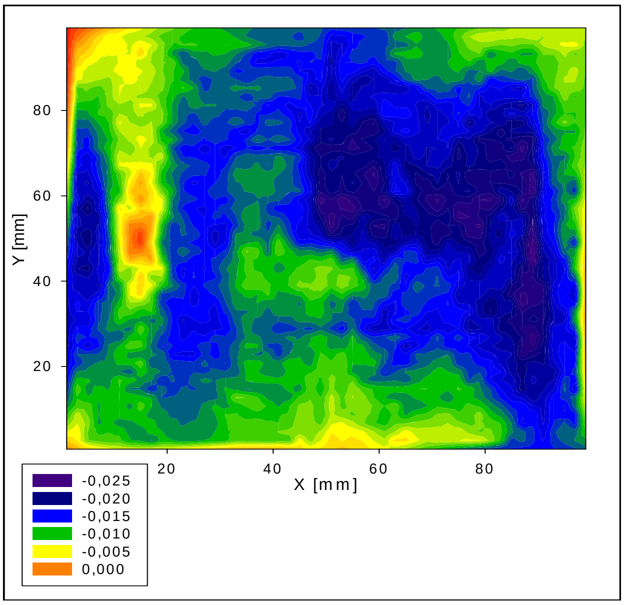

Fig. 3. Map of geometric deviations

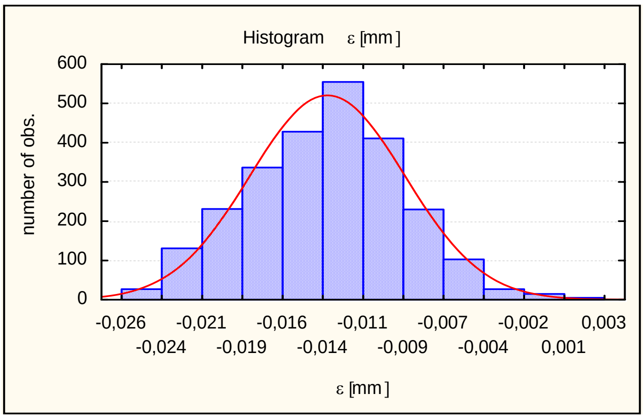

Fig. 4. Geometric deviations probability distribution

Tab. 1. Statistical parameters of ε sample (in mm)

	geometric dev. ε	component x	component y	component z
mean	-0.0137	-0.0006	-0.0001	-0.0141
std. dev.	0.0047	0.0092	0.0055	0.0057
min.	-0.0263	-0.0316	-0.0167	-0.0108
max	0.0034	0.0299	0.0227	0.0330

5. DETERMINING FITTING UNCERTAINTY

In the next stage, groups of 50 measurement points were randomly selected out of the scanned 2500 points fifty times in order to perform the fitting. 50 sets of transformation parameters deviations from their expected values, or the values obtained in the process of fitting on the basis of all the scanned points, were obtained. Standard deviations of parameters are presented in Tab. 2. The normalities of the transformation parameters deviations (*dx, dy, dz, ax, ay, az*) distributions were checked graphically. Probabi-lity distribution of all transformation parameters were quasi-normal. An example distribution for the parameter deviation *dx* is shown in Fig. 5. As the result, the joint distribution

of the vector of transformation parameters deviations was also normal.

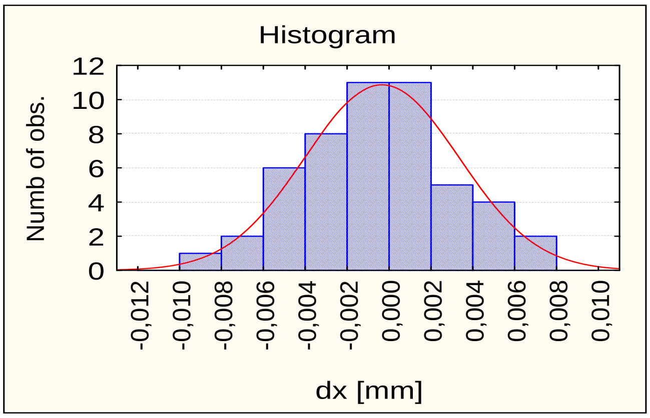

Fig. 5. Probability distribution of the transformation parameter deviation *dx*

Tab. 2. Standard deviations of transformation parameters

	parameter *dx* [mm]	parameter *dy* [mm]	parameter *dz* [mm]	parameter *ax*[deg]	parameter *ay* [deg]	parameter *az* [deg]
std. dev.	0.0036	0.0011	0.0025	0.003	0.002	0.002

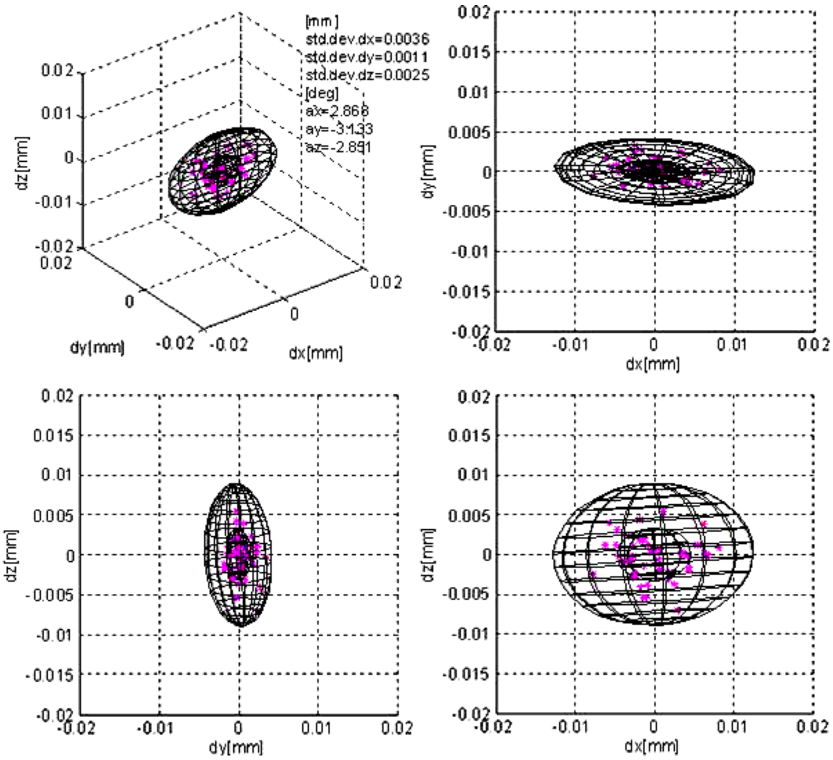

Fig. 6. Uncertainty contours and theirs projections on the coordinate system main planes

Assuming the P=0.95 ($\eta^2=\chi^2_{0.95}$) (6)=12.59 probability for the upper limit of the possible scatter range of the coordinate transformation and P=0.05 ($\eta^2=\chi^2_{0.05}$) (6)=1.63 for the lower limit from the (9) dependence, the equal probability hyperellipsoids limiting the (uncertainty) space were established. The computations and graphical illustration (Fig. 6) of the results were performed in the Matlab programme. The asterisks represent the transformation vector deviations scatter. It can be observed that the deviations of the transformation vector from their expected value, obtained in the experiment, are in the space within the uncertainty contours.

The origin of object coordinate system was located in the space limited by the obtained uncertainty contour with the probability P=0.95. Uncertainty of the object coordinate system was transferred to the uncertainty of each point determined in this system (and obviously, each geometric deviation). The contour dimensions were approx. 0.0252x0.0078x0.0176 mm. A symptom of the fact that the *X*-axis of the hyperellipsoid was greater size from two others (semi-axis is approx. 0.0126 mm) was caused by the greatest scatter of the component x of geometric deviations ε (Tab. 1).

6. CONCLUSION

In coordinate measurements, before determining the geometric deviations of a 3D surface, the process of fitting the measurement data to the nominal surface (CAD model) is performed. The transformation (rotation and translation) parameters describing the relation between the object coordinate system and the machine coordinate system are determined that way. The fitting effect is dependent on the number and location of the measurement points because of the occurrence of geometric deviations in producing particular surfaces in technology processes.

This paper presents the idea of fitting the measurement data to the CAD model with the use of the least square method, as well as the idea of determining the uncertainty contours at the assumption that the six transformation parameters are subject to a multivariate normal probability distribution. These equal probability contours are in a shape of hyperellipsoids determined from the multivariate normal distribution of six transformation parameters for the assumed confidence level.

The theoretical issues were verified by the experiments carried out on a free-form surface obtained in the milling process and characterised by random geometric deviations. Experimental values of the transformation parameters vector are located in the space limited by theoretically determined uncertainty contours which were determined and presented graphically. Scatters of translation parameters *dx, dy, dz* were approx. 3 times smaller then scatters of *x, y, z* components of geometric deviations. Dimensions of uncertainty hyperellipsoid centered around the expected values were 0.0252x0.0078x0.0176 mm.

REFERENCES

1. **Dhanish P. B., Mathew J**. (2006), Effects of CMM point coordinate uncertainty on uncertainties in determination of circular features, *Measurement*, Vol. 39, 522-531.
2. **Feng C. H. J., Saal A. L., Salsbury J. G., Ness A. R., Lin G. C. S.** (2007)**,** Design and analysis of experiments in CMM measurement uncertainty study*, Precision Engineering*, Vol. 31, 94-101.
3. **Kiciak P**. (2000), *The basis of modelling the curves and the surfaces*, WNT, Warsaw (in Polish).
4. **Kotulski, Z., Szczepiński W.** (2004), *Error Analysis with Applications In Engineering*, WNT, Warsaw (in Polish).
5. **Rajamohan G., Shunmugam M. S., Samuel G. L.** (2007), Sampling strategies for verification of freeform profiles using coordinate measuring machines, *9th International Symposium on Measurement and Quality Control*, Madras, India, 135-140.
6. **Ratajczyk E**. (2005), *Coordinate Measurement Technique*. OWPW, Warsaw (in Polish).
7. **Werner A., Poniatowska M**. (2006), Determining errors in complex surfaces machining with the use of CNC machine tools, *Archives of Mechanical Technology and Automation*, Vol. 26, No. 2, 211-217.
8. **Yau H. T**. (1998), Uncertainty analysis in geometric best fit, *Int. J. Mach. Tools Manuf*, Vol. 38, 1323-1342.
9. **Yau H. T., Menq C. H**. (1996), A unified least-square approach to the evaluation of geometric errors using discrete measurement data, *Int. J. Mach. Tools Manuf*, Vol. 36, No. 11, 1269-1290.

The work is supported by Polish Ministry of Science and Higher Education under the research project No. N N503 326235

PARAMETERS IDENTIFICATION OF BODNER-PARTOM MODEL FOR FLUID IN MR DAMPER

Paweł SKALSKI[*,*] , Krzysztof WOŹNICA[**] , Jerzy BAJKOWSKI[***]**

[*]Institute PRISME, University of Orleans, France
[**]Institute PRISME, Bourges Higher National School of Engineering, France, 88 Boulevard Lahitolle, 18020 Bourges
[***]Institute MDF, Faculty of Automotive and Construction Machinery, Warsaw University of Technology, Narbutta 84, 02-524 Warszawa

p.skalski@azspw.pl, krzysztof.woznica@ensi-bourges.fr, jba@simr.pw.edu.pl

Abstract: This paper presents an approach to describe a dynamic behaviour of magnetorheological damper by the Bodner-Partom constitutive law. The B-P equations usually used for metals are presented for shear stresses to express viscoplastic proprieties of MR fluid. Material parameters for the B-P law for fluid in the LORD RD 1005-3 damper are determined. Experimental results are compared with numerical results.

1. INTRODUCTION

Magnetorheological (MR) fluids like electrorheological (ER) fluids are a kind of smart material whose rheological properties may be rapidly varied by application of a magnetic field. This material typically consists of micron-sized ferrous particles dispersed in a fluid. When MR fluid is exposed to a magnetic field, the liquid state may be changed to semi-liquid or extremely to a solid state. When the magnetic field is removed, the state may recover to liquid. The speed of changes of rheological properties are an order of milliseconds. Controlled by computer and modern control methods, magnetorheological fluid can be used in all kinds of dampers (Carlton and Jolly, 2000; Spencer et al., 1996). Dampers with MR fluids may offer an improved control of vibrations in airplanes upon landing, and in cars, mechanical devices, and industrial machinery.

The main aim of this paper is to present a preliminary approach to parameters identification of the B-P law for fluid in the MR damper. The Bodner-Partom equations (Boder et al., 1979) usually used for metals are presented for shear stresses to express the viscoplastic proprieties of MR fluid.

2. EXPERIMENTS

Experiments have been conducted at a vertical stand for MR dampers with the forced kinematical movement, at Warsaw University of Technology. Installed sensors allowed to measure and record values of damping forces, and displacement of the piston rod during movement. The scheme of the stand was described in Bajkowski (2005) and is neglected here.

The research schedule included series of tests with one value of current I=1A with the different speed of forced kinematic movements n_1=100rpm, n_2=200rpm, n_3=400rpm. All experiments were carried out with the Rheonetic RD 1005-3 damper from Lord Corporation (Jimenez and Alvarez-Icaza, 2005).

3. MODEL AND PARAMETERS IDENTIFICATION

Results of the test for three different shear rates are the basis for the determination of parameters. During tests, values of displacements x, force F, and time t were recorded. Afterwards, the shear stress τ, the shear strain strain γ, the inelastic shear strain γ^I and the inelastic shear rate $\dot{\gamma}^{\mathrm{I}}$ can be calculated respectively:

$$\tau = \frac{F}{A}, \gamma = \frac{\Delta x}{h}, \gamma^{\mathrm{I}} = \gamma - \frac{\tau}{G}, \tag{1}$$

$$\dot{\gamma}^{\mathrm{I}} = \frac{\mathrm{d}\gamma^{\mathrm{I}}}{\mathrm{d}t} = \dot{\gamma} - \frac{1}{G}\frac{\mathrm{d}\tau}{\mathrm{d}\gamma}\dot{\gamma}, \tag{2}$$

where A and h stand for the working interface area and the gap size, and G is the shear modulus. Fig. 1 presents the shear strain-shear stress relation for three different shear rates. These relations served for the identification of the Bodner-Partom model.

In this case of neglecting the recovery effects, the constitutive formulation of Bodner-Partom can be expressed in the following form (Woźnica et al., 2001):

$$\dot{\gamma}^{\mathrm{I}} = 2D_0 \exp\left[-\frac{1}{2}\left(\frac{R+D}{\sqrt{3}\tau}\right)^{2\mathrm{n}}\frac{n+1}{n}\right]\mathrm{sgn}(\tau), \tag{3}$$

$$R = R_1\left[1 - \exp\left(-m_1 W^{\mathrm{I}}\right)\right] + R_0 \exp\left(-m_1 W^{\mathrm{I}}\right),$$

$$D = D_1\left[1 - \exp\left(-m_2 W^{\mathrm{I}}\right)\right], \tag{4}$$

where R represents the isotropic hardening, D is the function associated to the kinematic hardening. The parameter D_0, that designates the maximal value of the shear rate, can be chosen arbitrarily. In almost static problems, one admits $D_0=10^4 s^{-1}$ (Chan et al., 1998). D_1, R_0, R_1, m_1, m_2, n are the parameters to be identified and $\dot{W}^{I}=\tau\dot{\gamma}^{I}$ is the inelastic work rate. The relation (3) can be written as a functional relationship between the shear stress, the inelastic shear rate and the hardening variables,

$$\frac{\tau}{R+D}=f\left(\dot{\gamma}^{I}\right). \tag{5}$$

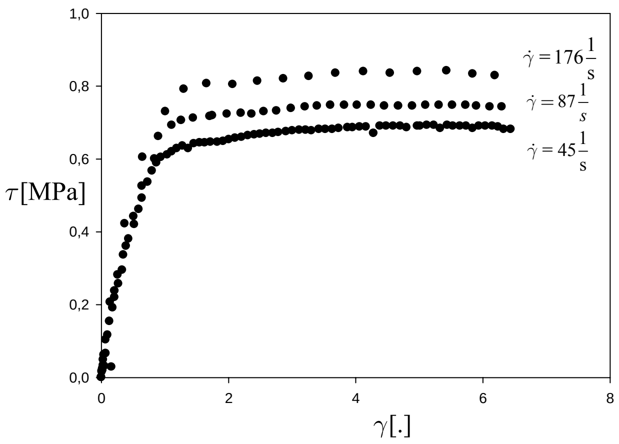

Fig. 1. Shear stress as a shear strain function-experimental data for three different shear rates

The identification of n and R_0 parameters can be carried out from Eqs. (5), expressed for small values of inelastic shear strain (e.g., γ^I=0,2%), for several different shear rates. When the material enters in the plastic domain, one can consider that the isotropic hardening is equal to its initial value $R=R_0$, and the kinematic hardening is negligible. The initial yield stress function of the shear rates is written according to (3):

$$\tau_{02}=\frac{R_0}{\left[\frac{2n}{n+1}\ln\left(\frac{2D_0}{\sqrt{3}\dot{\gamma}^{I}}\right)\right]^{\frac{1}{2n}}}. \tag{6}$$

Having several values of τ_{02} for different shear rates, the diagram $\tau_{02}\left(\dot{\gamma}^{I}\right)$ can be drawn (Fig. 2) and by the least squares method non linear regression, n and R_0 values can be determined.

Subsequently, the inelastic shear strain γ^I, Eq. (1), is calculated to construct the curve $\tau(\gamma^I)$ for every test, and this curve can be approximated by the multi parameter exponential function (Fig. 3):

$$\tau=a\left(\gamma^{I}\right)^{b}\exp\left(c\gamma^{I}\right)+d, \tag{7}$$

where coefficients a, b, c and d can be determined by the Marquardt-Levenberg regression. It permits of the derivative:

$$\frac{d\tau}{d\gamma^{I}}=a\left(\frac{b}{\gamma^{I}}+c\right)\left(\gamma^{I}\right)^{d}\exp\left(c\gamma^{I}\right), \tag{8}$$

which is used to draw the function of the work hardening rate ψ, Fig. 5:

$$\psi=\frac{d\tau}{dW^{I}}=\frac{d\tau}{d\gamma^{I}}\cdot\frac{1}{\tau}; \quad dW^{I}=\tau\cdot d\gamma^{I}. \tag{9}$$

Taking into account formulas (3-6), the hardening work rate function (9) can be written in the following form:

$$\psi=\frac{\tau_0}{R_0}\left[m_1\left(R_1-R\right)+m_2(D_1-D)\right]. \tag{10}$$

Supposing for the small inelastic shear strains $R=R_0$ (Border et al., 1979), and using (3) and (6), formula (10) becomes:

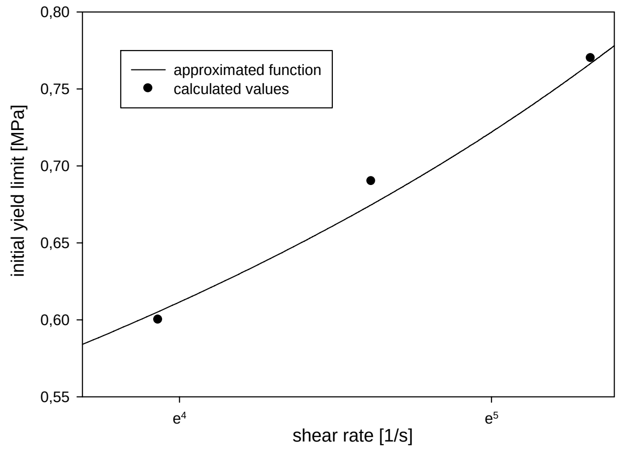

Fig. 2. Conventional yield limit for the B-P model as a function of strain rate

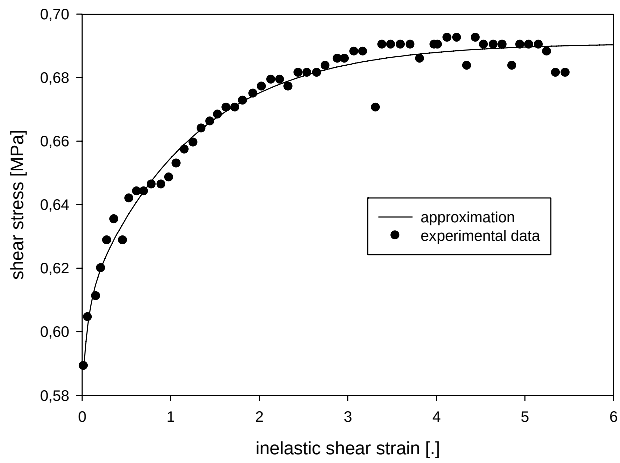

Fig. 3. Shear stress-inelastic shear strain plot, and a numerical approximation

$$\psi=\frac{\tau_0}{R_0}\left[m_1\left(R_1-R_0\right)+m_2(R_0+D_1)\right]-m_2\tau. \tag{11}$$

The expression (11) shows that, for small inelastic shear strains, the graph $\psi(\tau)$ must be linear with a slope m_2.

For the larger shear strains, the kinematic hardening is rapidly saturated, so $D \approx D_1$. Equations (3), (6), (10) then give:

$$\psi = \frac{\tau_0}{R_0} m_1 (R_1 + D_1) - m_1 \tau \,. \tag{12}$$

The formula (12) indicates that for higher shear strains, the function $\psi(\tau)$ becomes linear again with a slope m_1.

To determine parameters m_1 and m_2, it is sufficient to calculate two slopes on both extremities of the curve $\psi(\tau)$ (Fig. 5) and according to (11), (12) the values of ψ_s and τ_s can be found:

$$\psi_s = \frac{\tau_0}{R_0}\left[m_1 \left(R_1 - R_0 \right) + m_2 (R_0 + D_1) \right], \tau_s = \frac{\tau_0}{R_0}\left(R_1 - D_1 \right) \tag{13}$$

Equations (13) permit parameters D_1 and R_1 to be obtained. In the next part of this work we present the numerical solutions for obtained parameters.

4. NUMERICAL SOLUTION

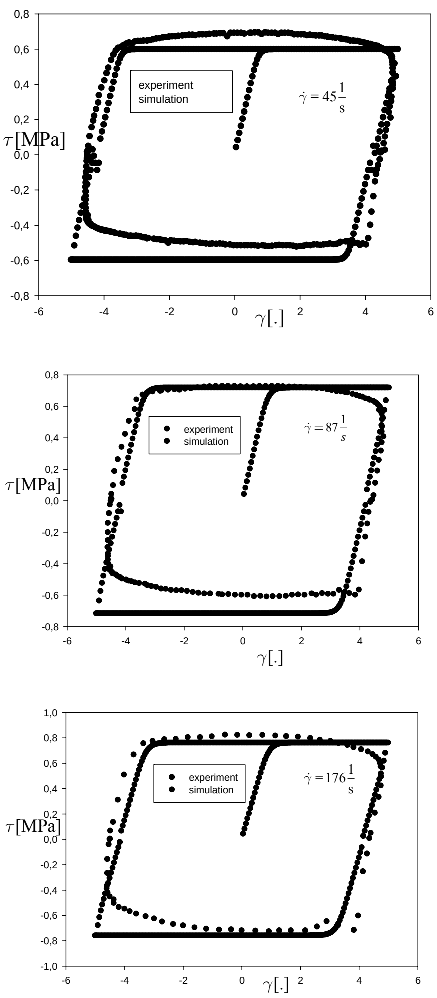

Fig. 4. Comparison of the experimental data and obtained results from numerical solutions by the Bodner-Partom law, for three different shear strain rates: $\dot{\gamma} = 45\frac{1}{s}, \dot{\gamma} = 87\frac{1}{s}, \dot{\gamma} = 176\frac{1}{s}$

Relations of shear strain-shear stress for three different shear rates (Fig.1) served for the identification of the Bodner-Partom model. Received parameters were used to numerical simulation. The calculation was made in the Excel program. The Euler's method was used to solve the equation (3). Numerically obtained results are compared with the experimental data for three different values
of the shear strain rate. We observe a good concordance between the experimental data with the numerical solution of Bodner-Partom model (Fig. 4).

5. CONCLUSIONS

In this paper, the constutive equations of the Bodner-Partom model are used for magnetorheological fluid in the damper. Conducted experiments on the Lord RD 1005-3 damper served for the identification of parameters of the B-P law. Experiments and the numerical results for three different values of shear strain rate validate the B-P model. The numerical model shows a good level of accuracy between the experimental and calculated data. It shows that the Bodner-Partom law, first allocated for metals, permits to describe the behaviour of magnetorheological fluid in the damper.

More research is being conducted in order to improve the model behaviour, especially to accommodate the values of current in a coil.

REFERENCES

1. **Bajkowski J.** (2005), Stanowisko badawczo dydaktyczne do wyznaczania wybranych charakterystyk tłumika lub amortyzatora magnetoreologicznego, *XXII Sympozjon PKM*, Gdynia-Jurata.
2. **Boder S. R., Partom I., Partom Y.** (1979), Uniaxial Cyclic Loading of Elastic-Viscoplastic Materials, *Journal of Applied Mechanics*, Vol. 46.
3. **Carlson J. D., Jolly M. R.,** (2000)**,** MR fluid, foam and elastomer devices, *Mechatronics*, 10, 555-569.
4. **Chan K. S., Bodner S. R., Lindholm U. S**. (1998), Phenomenological Modeling of Hardening and Thermal Recovery in Metals, *Journal of Engineering Materials and Technology*, Vol. 110.
5. **Jimenez R., Alvarez-Icaza L**. (2005), *LuGre friction model for a magnetorheological damper*, Structural Control and Health Monitoring, Mexico.
6. **Spencer B. F., Dyke S. J., Sain M. K., Carslon J. D.** (1996), Phenomenological Model of a Magnetorheological Damper, *ASCE Journal of Engineering Mechanics*.
7. **Woźnica K., Pennetier O., Renard J.** (2001), Experiments and Numerical Simulations on Thin Metallic Plates Subjected to an Explosion, J*ournal of Engineering Materials and Technology*, Vol.123, 203-209.

A BIOMECHANICAL MODEL OF OPERATED ACHILLES TENDON

Vasiliy STAVROV*, Vladimir LASHKOVSKI, Anatoly SVIRIDENOK*****

*Belorussian State Technological University. Sverdlov str., 13A, 220630 Minsk, Belarus
**City Clinical Hospital of the First MedicalAid, Pogranichnikov str., 115, 230027, Grodno, Belarus
***The State Scientific Institution «The Research Center of Resources Saving Problems
of the National Academy of Sciences of Belarus» Tyzengauz sq., 7, 230023, Grodno, Belarus

vpstavrov@user.unibel.by, lvv52@mail.ru, resource@mail.grodno.by

Abstract: The paper discusses a biomechanical model reflecting deformation and tear of a tendon part, namely, ellipric in cross-section strand formed by stochastically located collagen fibers whose strain to stress relation obeys the exponential law. Recovery of the tendon by a plastic reinforcement is shown to result in elevated rigidity and shorter limiting elongation of the strand proportionally to the reinforced portion length, the strength of the restored strand being preserved almost fully. The limiting deformation of the recovered strand made with incisions for adaptation of the ends increases the more the deeper are the incisions, their number and the total length of the areas being adapted. This, nevertheless, decreases essentially the breaking load during further loading.

1. STRUCTURE

The Achilles tendon consists of three or four parts each being linked to a certain group of muscles, namely, the internal and external gastrocnemius muscles and the soleus one (Sitnik, 2003; Medical Encyclopedia). The given work studies the model of only one part of the tendon called a strand.

It is anticipated that the bundles of collagen fibers are stochastically positioned over the strand cross-section (Fig. 1).

To distribute the sectional area of the fibers we have accepted Weibull's law with a mean value 0.2 mm^2 and variation factor ~0.4. The total sectional area of the fibers in a strand makes up $Ac \cong 40$ mm^2, the number of the fibers in a model strand is 250.

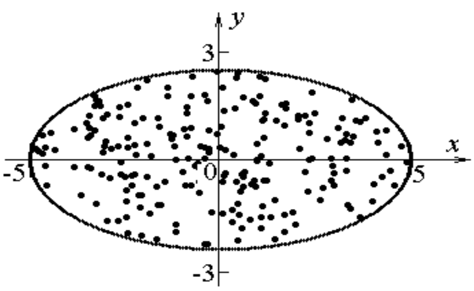

Fig. 1. A cross-sectional model of a strand

2. DEFORMABILITY AND STRENGTH OF THE FIBERS

The deformation law of the collagen fibers is accepted in the following form as an exponential function

$$\sigma(\varepsilon) = c_n \varepsilon^n, \qquad (1)$$

where c_n – elasticity modulus; n – power exponent (not obligatory an integer number).

The elasticity modulus and exponent in Eq. (1) are dependent on a patient's individual features. In further calculations we have taken that $c_n = 10$ Gpa.

We presumed that tear of the collagen fibers occurs after reaching some limiting strain without plastic flow

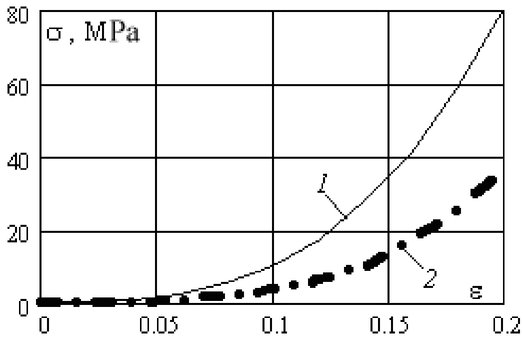

Fig. 2. Diagrams of fiber deformation at n = 3 (1) and n = 3.5 (2)

The limiting strain of the fibers was presented by a random value obeing a normal law of distribution with parameters $M\varepsilon$ and $s\varepsilon$. Along with above named, we have introduced a scale factor, which is a dependence of the limiting strain on sectional area A of the fibers in the form of an exponential function

$$k(A) = (Ac/A)^m, \qquad (2)$$

where Ac – mean sectional area of the fibers in a strand; m – an index accounting for the the degree of dependence of the limiting strain on dimensions.

The mean limiting strain value of a model bundle of fibers is $\varepsilon c = 0.208$, the variation factor is $V\varepsilon = 0.19$, which surpasses much the initial value $s\varepsilon/M\varepsilon = 0.125$ due to a size scatter of the fiber sections in a bundle.

At $M\varepsilon = 0.2$, $s\varepsilon = 0.025$ and $m = 0.2$, which is reflected in a histogram shown in Fig. 3.

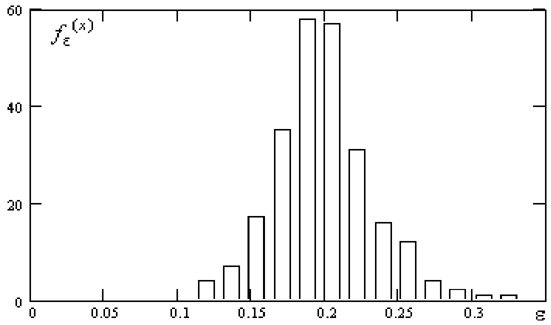

Fig. 3. Distribution histogram of limiting strains of collagen fibers

3. DEFORMABILITY AND STRENGTH OF A STRAND

The diagram for deformation of a strand (Fig. 4) was constructed by giving a sequential series of strains with account of the bearing capacity (stress multiplied by sectional area) of those fibers whose limiting strains exceed the given one.

$$F(\varepsilon) = \sum_{i`} \sigma_i`(\varepsilon) \cdot A_i` \quad (3)$$

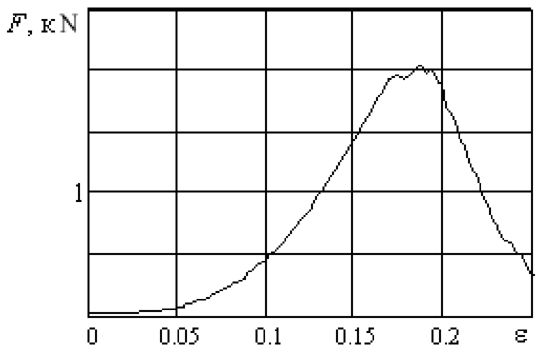

Fig. 4. Deformation diagram of a strand

The breaking force of 2 kN obtained by calculations is close to the values typical for the parts of Achilles tendon (Bergel, 1971). The deformation corresponding to a maximum load constitutes 18%, which also fits the range of observed during the experiment values. The descending branch indicates lowering of the bearing capacity of the strand after reaching some limiting load.

It is also noted in a number of works on pathogenesis and recovery of Achilles tendon that tear of a tendon is preceded by a gradual accumulation of degeneratyive dystrophic changes in the tissues and membrane of the tendon. This occurs most often during tedious and intensive physical exercises typical for sportsmen and ballet dancers (Aiuyb, 1997).

The degree of microdamage of the strand as a share of fibers breaking under loading F (Stavrov, 2008) was estimated by the formula

$$Q(F) = 1 - \frac{1}{As} \sum_{i`} A_i(F)`, \quad (4)$$

where $A_i(F)`$ – area of the fiber keeping its strength under load F on the strand; As – total (initial) cross-section area of strand fibers.

Proceeding from Eq. (4), we have constructed a diagram of fiber microdamage in a loaded strand (Fig. 5).

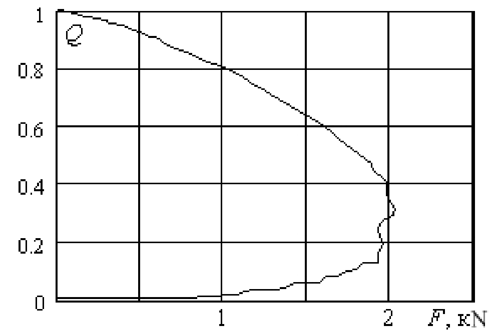

Fig. 5. Diagram of microdamage of the strand

The diagram visualizes that noticeable damages of the fibers are observed already under the loads twice as low as the limiting ones. This complies with available data on investigations of Achilles tendom failure.

The calculation results presented in Fig. 5 prove that the limiting load corresponds to rather large share of the damaged fibers reaching 30%. Apparently, under repeated loads approaching the limiting ones microdamages are to be observed systematically, while their healing will lead to variations in the mechanical properties of the tendon. This is why, estimation of the microdamage degree of the tendon fibers gives important data for prophylactics and curing of tendon tear.

The position of the foot effects the strained length of the strand and load distribution between the strands as parts of the tendon. The length of a random fiber in a strand was estimated roughly with account of deviations of the foot by the relation

$$L = lo - l`/\cos\phi + \Delta L \;, \quad (5)$$

where lo – length of a straight line part; $l`$ – length in the zone of fixing to the muscles and calcanean tuber; φ – angle of deviation of the fixed fiber part; ΔL – length variation due to deviation of the foot from the normal position.

The length of the linear portion of the fibers was taken equal to 80-100 mm, the length in the zone of fixing was also 80-100 mm and distribution of angle φ was taken close to the normal law.

Variations in the fiber length at deviation of the foot from the horizontal position are not large and do not surpass 10^o, so far the corresponding changes in the fiber length are negligible. A larger deviation of the foot is in the vertical plane during the plantar and backside flexure.

In this case, $\Delta L \cong xo\ \Delta\theta$, where xo is distance over the contour line from the point of revolution of a subtalar articulation till the tendon; $\Delta\theta$ – plantar bend angle (counted from a normal position of the planta). By taking that xo = 40 mm, we obtain an increment of the fiber length as a function of the foot flexure.

The mean limiting deformation value of the fibers somewhat increases by means of increasing fiber length during backside foot flexure, whereas the limiting deformation distribution shifts to the side of higher values. The threshold load on the strand augments too (Fig. 6).

The character of these changes with increasing foot bend angle is analogous to that presented in Fig. 6, and its force is independent in the muscles stretching the Achilles tendon (Bergel, 1971). Evidently, above regularity reflects a natural adaptation of the tendon to a growing load in the course
of backside flexure of the foot.

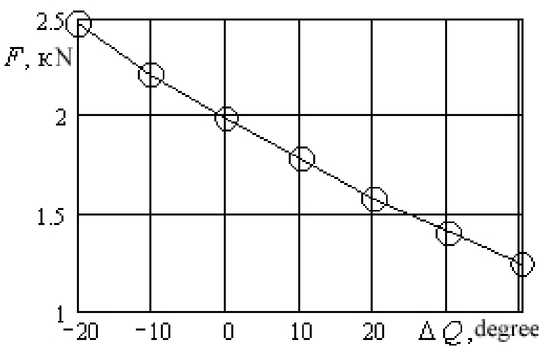

Fig. 6. Limiting load on strand versus foot bend angle

The level of microdamage corresponding to the fracture load on the strand during backside flexure of the foot cedes the one at plantar flexure (Fig. 7).

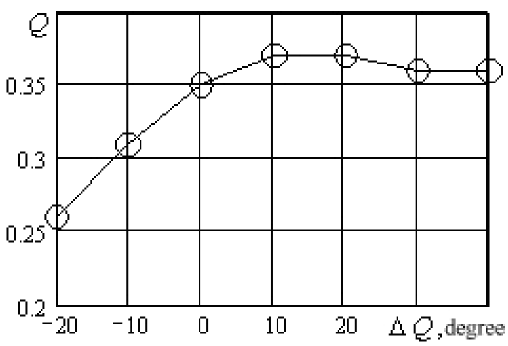

Fig. 7. Dependence of fiber microdamage under threshold load on strand upon plantar bend angle

Above dependence can be actually explained by the increasing mean value and the root mean square deviation of the fiber length.

4. PLASTIC REINFORCEMENT EFFECT

One of most accustomed methods of operative rehabilitation of the Achilles tendons tear is the plastic reinforcement of the initial suture with a patch of the gastronomies muscle, aponeurosis of the tendons or synthetic implants (Sitnik, 2003). Each of named cases leads to widening of the tendons cross-section area along with variation of its deformability in the zone of plastic reinforcement.

To estimate the effect of the plastic reinforcement on the tendon strength we have accepted that its reinforcement leads to variations in fiber deformability. The parameters of the law of deformation change too (1). The deformation diagram of the strand over the area of reinforcement is characterized by the relation

$$F``(\varepsilon) = As\, c_n``\varepsilon^{n``}, \tag{6}$$

where As – nominal sectional area of the strand; $c_n``$ and $n``$ – stiffness parameters of the strand.

The length of the fibers on undamaged portions $L`$ reduces by a length of plastic reinforcement $L``$. Their limiting deformations change correspondingly.

Elongation of the recovered strand under load F and deformation of the fibers ε are found by the formula

$$\Delta L(\varepsilon) = \varepsilon\, L` + \left(\frac{F(\varepsilon)}{c_n``As}\right)^{1/n``} L``. \tag{7}$$

The deformation diagram of the recovered strand has been constructed proceeding from the relationship between the load and elongation given by formula (7).

It was found out that as a result of plastic reinforcement the tendon acquires elevated rigidity at $c_n``$=20GPa and $n``$=2, the limiting load being kept however, at the previous level.

With lengthening of the reinforced portion (under invariable stiffness parameters) the limiting elongation, which corresponds to the breaking looad, reduces almost linearly (Fig. 8). The relative increment of the limiting elongation is not, nevertheless, large either.

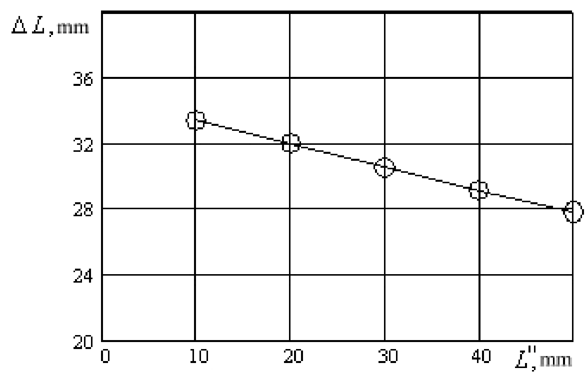

Fig. 8. Limiting elongation of recovered strand versus reinforcement portion length

Above described character of the plastic reinforcement effect is because the structure and properties of the undamaged portion remain invariable, while rigidity increases inversely proportional to the length of the reinforced area for the variant under consideration. Evidently, this effect will be different for a reinforcement portion with some other properties.

5. EFFECT OF INCISIONS

Incisions of the strand made for adapting the ends of the damaged tendon result in variations of its rigidity as well. Here, the incision depth h (and, respectively, angle a\`), width $la$\`\` (and angle β) and the number of incisions may vary (Fig. 9).

The incision depth influences the part of the fibers cut and the share of undamaged sectional area. The main parameters are interrelated by the following dependencies

$$\alpha`(h) = \arccos(1 - h/a);\ x(\alpha`) = a \cdot \cos(\alpha`);$$
$$A(h) = \frac{ab}{2}(2\alpha`(h)\text{-}\sin(2\alpha`(h)), \quad (8)$$

where a and b – ellipse semiaxes (Fig. 9).

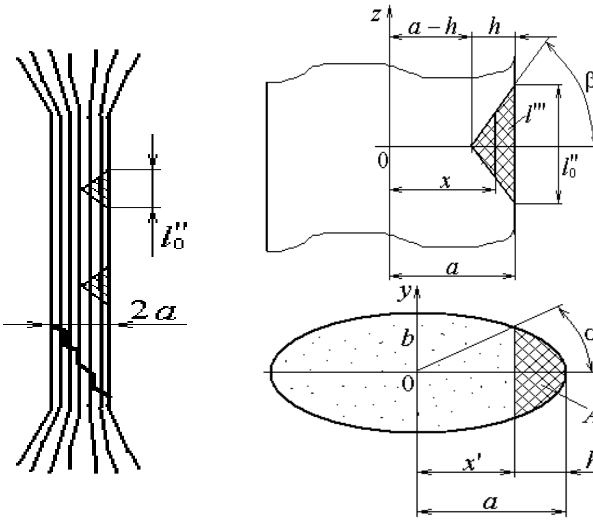

Fig. 9. A scheme of incisions on elliptical in incross-section strand during operation

The initial bearing capacity is preserved only by the fibers located on the sectional area $x < x(\alpha`)$. The limiting strain of the cut-off fibers (at $x > x(\alpha`)$) decreases inversly proportional to the recovered length

$$L``(h) = 2h\ k\ \text{tg}\ \beta, \quad (9)$$

where k – number of incisions of depth h and angle β.

So, elongation of the fiber is

$$\Delta L(\varepsilon) = \varepsilon\, L` + \varepsilon^{n/n``} L``(h) \quad (10)$$

Distribution of the limiting strains of the fibers was determined with account of above relations. The distribution curve of the limiting strain of the fibers in the recovered strand shifts to the region of low values the more the deeper are the incisions and the more is their number.

Reduction of the level of limiting strains results in a lowered rigidity of the strand and decreased threshold force the recovered strand can withstand during further loading (Fig. 10).

Thus obtained regularities are because in part this model neglects the peculiar load transfer features in the zone of recovery. They can be accounted for if the respective information on mechanical properties of the recovered portions of the tendon is available.

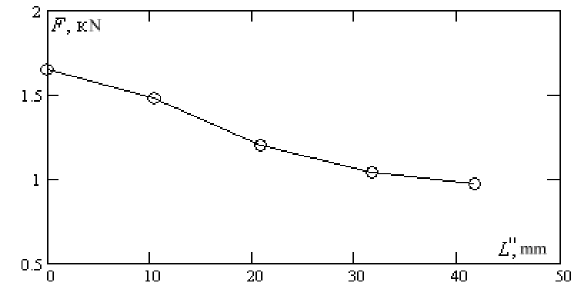

Fig. 10. Threshold load on recovered strand versus total length of incisions

6. CONCLUSIONS

A biomechanical model has been studied for the deformation and failure of one of the parts of a strand tendon of elliptical cross-section formed by stochastically located collagen fibers whose strains and stresses are found in an exponential dependence. The model accounts for the scatter of sectional areas and the length of collagen fibers. Named conditions promote almost linear strength reduction of the strand with increasing bend angle of the plantar, although the share of teared fibers under the maxumal load on the tendon varies insignificantly.

The model of the operated tendon in the form of sequentially linked undamaged and recovered portions has visualized that rehabilitation of the tendon by a plastic reinforcement leads to a raised rigidity and reduced limiting elongation almost proportional to the reinforcing portion length, in which conditions the recovered strand strength is preserved practically fully. The threshold deformation of the recovered strand in which incisions were made to adapt its ends grows and is the higher the deeper are the incisions and the more is their number and the total length of the adapted portions. This, however, leads to a considerable reduction of the breaking strength under further loading.

The present results can be used for selection of the optimal strategy of surgical rehabilitation and treatment of damaged Achilles tendons with allowance for anthropological features of the patient and the character of damage.

REFERENCES

1. **Aiuyb H. M.** (1997), *Physical rehabilitation of sportsmen after surgical treatment of Achilles tendon tear*, Cand. Sci. Thesis, 13.00.04б 14.00.12, Moscow, /bestdisser.com/see/dis_226732.html.
2. **Bergel, D. H.** (1971), The static elastic properties of arterial wall, *J. Physiol.*, Vol. 156, 445–457.
3. **Sitnik A. A.** (2003), Subcutaneous tear of Achilles tendon: pathogenesis – diagnostics and curing, *BMJ*, Vol. 5, No. 3, 12.
4. **Stavrov V. P.** (2008), *Mechanics of composite materials*, Textbook, Minsk, BGTU, 262.
5. Medical Encyklopedia, Damage of Achilles Tendon http://medarticle.moslek.ru.

PREMISES OF OPERATIONAL METHOD OF CALCULATION OF RELIABILITY OF MACHINES ON THE BASE OF PARAMETRIC AND MOMENTARY SYMPTOMS OF DAMAGE

Tomasz SUDAKOWSKI[*]

[*]Department of Automation and Robotics, Faculty of Mechanical Engineering, Białystok Technical University, ul. Wiejska 45C, 15-351 Białystok

sudak@plusnet.pl

Abstract: In the article presented was the practical method of calculation of standard reliability characteristics of technical objects of unchanging and changeable structure during their work, based only on parametric and momentary symptoms of damage, the method of determination of symptoms of parametric damage on the base of diagnostic and momentary information and on the base of information about the state of adjustment of the object.

1. INTRODUCTION

In the process of use of an operational technical object arise randomly defects (catastrophic, parametric and momentary), which cause that the object changes its state from operational to inoperable.

Catastrophic defects are sudden and total defects. They cause immediate and total loss of object's ability to correct work. Among this kind of defects are: break, deformation, notch, burning or melting of individual elements.

Parametric defects lead to partial and removable damage of some elements. In the initial phase they cause increasing deterioration of quality of their functioning. These defects can have conventional character (e.g. exceeding of acceptable value of adjustment quality ratio).

Momentary defects are characterised by the fact that they can disappear automatically without interference of an operator after disappearing of cause, which generated them. The causes of this kind of damage are e.g. occasional variations of temperature, humidity, accelerations and vibrations.

These defects are the base for to calculation of reliability characteristics. The serious problem is the appearance of catastrophic damage. Therefore continuous efforts are aimed at development of new effective methods of calculation of reliability on the base of only relatively harmless parametric and momentary defects.

2. CENTRAL REMARKS CONCERNING METHODS OF CALCULATION OF RELIABILITY

During calculation of reliability of any complex object it is necessary to determine the probability of appearance of its damage. The calculation should consider three types of damage: catastrophic, parametric and momentary. Additionally, it is assumed usually that appearing defects are independent events, then (Lindstedt and Sudakowski, 2007b; Sotskow, 1973):

$$R(t)=R_a(t)R_b(t)R_c(t) \tag{1}$$

$R(t)$ – probability of correct operation in view to all appearing defects, $R_a(t)$ – probability of correct operation in view to catastrophic damage, $R_b(t)$ – probability of correct operation in view to parametric damage, $R_c(t)$ – probability of correct operation in view to momentary damage.

Probability of correct operation in view to momentary damage depends on a variety of factors, which are difficult to consider during calculation. Therefore the probability $R_c(t)$ is determined experimentally or assumed as equal to 1.

Parametric defects (R_b) are the defects, which do not stop operation of the object but its parameters are beyond admissible limits. These defects can be caused by excessively big dispersion of technical parameters of object elements (Lindstedt and Sudakowski, 2007b; Sotskow, 1973). May be designated the density function changes diagnostic parameter (Tomaszek et al., 2008)

However, we deal with catastrophic damage (R_a), when the object does not work at all, i.e. does not fulfil its function. This damage can be caused by defects of object structure (Lindstedt and Sudakowski, 2007b; Sotskow, 1973).

2.1. Reliability of objects of unchangeable structure in the process of operation

In the case of objects of unchangeable structure the probability of correct operation is defined with the formula:

$$R(t) = R_a(t)R_b(t) \tag{2}$$

where: $R_a(t)$ – probability of correct (failure-free) operation in view to total damage (catastrophic), causing total damage to the element, $R_b(t)$ – probability of correct (failure-free) operation in view to partial damage (parametic), changing the parameter of an element beyond admissible limits.

Probability of correct operation defined as the reliability characteristic of the object depends on probability of correct operation of elements, fulfilling basic functions in the course of operation of given object. Other elements fulfilling secondary role are so-called auxiliary elements, e.g. elements of control system, protective elements etc., which influence the reliability of the object to small extent only. Damage to auxiliary elements can cause certain insignificant changes of parameters and operational conditions of basic elements.

The course of method of determination of probability of correct operation of the object of unchangeable structure is as follows (Sotskow, 1973):

1. Determination of basic part of the object, which fulfils its preset functions.
2. Determination of technical parameters of basic elements of the object.
3. Determination of changes of parameters of entire object and its basic elements resulting from damage to auxiliary elements:
   a) in the case of total damage (catastrophic) e.g. short circuits or breaks;
   b) in the case of partial damage (parametric) consisting in change of parameters of auxiliary elements beyond admissible limits.
4. Definition of intervals of physical and physicochemical variations of external factors during operation:
   a) temperature;
   b) humidity;
   c) accelerations and impacts;
   d) vibrations;
   e) air pressure;
   f) composition and quantity of active additives in surrounding atmosphere;
   g) radioactive radiation.
5. Determination of value of reliability of each basic element in relation to total (catastrophic) damage.

$$R_a = e^{-(\lambda+\lambda' f)T} \tag{3}$$

The values of damage intensity λ and λ' should be selected with consideration of technical parameters and operational conditions of individual elements. For this purpose λ and λ' in normal conditions and at nominal technical parameters (values of current, voltage, power, frequency, phase) should be replaced with values corresponding to real technical parameters in real operational conditions.

The operational reliability of an element R_{ai} should consider the probability of damage of type break F_0 and of type short circuit F_z.

$$R_{ai} = 1 - F = 1 - \left(F_0 + F_z\right) \tag{4}$$

6. Determination of reliability of individual elements in relation to partial damage (parametric) F_{bi}, which can be caused by changes of:
   a) properties of an element itself;
   b) parameters of power supply of an element (voltage, current, power, frequency, phase);
   c) operational conditions of an element (temperature, humidity, vibrations, accelerations).
7. Calculation of reliability of operation for individual elements:

$$R_i = R_{ai} R_{bi} \tag{5}$$

8. Calculation of reliability of operation for the object:

$$R(t) = R_\Sigma = \prod_{i=1}^{n} R_i \tag{6}$$

where: **n** – number of Basic elements.

$$R(t) = R_\Sigma = \prod_{i=1}^{n} R_{ai} \prod_{i=1}^{n} R_{bi} = R_{a\Sigma} R_{b\Sigma} \tag{7}$$

In given case it is assumed that the probability of absence of momentary damage R_c=1.

2.2. Reliability of objects of changing structure in the process of operation

Calculation of reliability of objects of changing structure i.e. such objects, in which during their operation in various moments of time work various elements, has certain metodological curiosities:

a) the entire cycle of operation is divided into steps corresponding to individual operational states,
b) for each step of operation prepared is the scheme containing all elements working during given step,
c) determined are parameters of power supply for elements during individual steps of operation.

Next determined is the reliability of operation of the object $R_{\tau x}$ or intensity of damage $\lambda_{\tau x}$ corresponding to individual steps of operation.

In general case, where considered are total and partial damage, the reliabilities during individual steps of operation can be described with formulas:

$$R_{\tau 1} = R_{tb_1} e^{-\lambda_{\tau 1} t_{01}}, R_{\tau 2} = R_{tb_2} e^{-\lambda_{\tau 2} t_{02}}, \ldots, R_{\tau k} = R_{tb_k} e^{-\lambda_{\tau k} t_{0k}} \tag{8}$$

where: R_{tb1}, R_{tb2},…, R_{tbk} – values of reliability in relation to partial damage corresponding to individual steps of operation.

Total reliability corresponding to one operational cycle is equal to:

$$R = R_{tb_1} R_{tb_2} \ldots R_{tb_k} e^{-(\lambda_{\tau 1} t_{01} + \lambda_{\tau 2} t_{02} + \ldots + \lambda_{\tau k} t_{0k})} = \prod_{x=1}^{k} R_{tb_x} e^{-\lambda_{\tau x} t_{0x}} \tag{9}$$

Reliability of operation during N occurring repeatedly cycles:

$$R_N = R_b^N R_a^N = \prod_{x=1}^{k} R_{tb_x}^N \left[e^{-\lambda_{\tau x} t_{0x}} \right]^N \tag{10}$$

It is necessary to consider that the intensity of damage λ is not a constant value, but has certain dispersion around average value λ, defined usually with normal or log-normal distribution. This dispersion for various elements can be characterised with variation coefficient, which in the case of normal distribution is equal to $\chi = \frac{\sigma_\lambda}{\lambda}$, and in the case of log-normal distribution amounts to $\chi_{\ln\lambda} = \frac{\sigma_{\ln\lambda}}{\ln\lambda}$.

3. CALCULATION OF RELIABILITY CHARACTERISTICS IN THE PROCESS OF OPERATION ON THE BASIS OF PARAMETRIC AND MOMENTARY DAMAGE

The basis for calculation of *R(t)* are three basic types of damage: catastrophic (R_a), parametric (R_b) and momentary (R_c) (Bobrowski, 1985; Lindstedt, 2006; Lindstedt and Sudakowski, 2008; Sotskow, 1973; Tomaszek et al., 2008; Zamojski, 1981).

The fundamental task of maintenance is elimination of causes of catastrophic defects *(Ra(t)=1)*. Thus, the reliability characteristics can be determined only on the basis of parametric and momentary defects, which are hard to degfine:

$$R(t)= R_b(t)R_c(t) \tag{11}$$

It has been observed that the basic knowledge about parametric and momentary defects can be achieved through observation of changes of technical condition parameter „a_{Rb}“ and adjustment state parameter „a_{Rc}” determined during diagnostic and adjustment of the object (Lindstedt et al., 2003; Paton et al., 1989).

4. SYMPTOMS OF KNOWLEDGE ABORT PARAMETRIC AND MOMENTARY DEFECTS

Basic knowledge about parametric defects (R_b) can be achieved through observation of changes of technical condition parameter „a_{Rb}“ determined during diagnostic of the object. To calculate the parameter „a_{Rb}“ we use the equation of state:

$$\frac{dD_K}{d\Theta} = a_{R_b} D_K + b_{R_b} U \tag{12}$$

where: D_K – variable of technical condition, U – variable of adjustment state (utility signal), a_{Rc} – parameter of adjustment state, b_{Rb} – parameter of technical condition (influence of environment).

The equation of state connecting dynamics of given process $dD_K/d\Theta$ with his process D_K and its environment U is applied in automation, diagnostics and reliability depending on needs occurring in these autonomous subjects (Ashby, 1963; Girtler, 2003; Lindstedt and Sudakowski, 2007a).

According to principles of static and dynamic identification (Söderström i Stoica, 1997) from the equation (12) we obtain:

$$D_K = \left(-\frac{b_{R_b}}{a_{R_b}}\right) U = \hat{a}_{R_b} U \tag{13}$$

$$\hat{a}_{R_b} = \frac{\Sigma D_{Ki} U_i}{\Sigma U_i^2} \tag{14}$$

and

$$\frac{\Delta D_K}{\Delta\Theta} = a_{R_b} D_K + a_{R_b} \hat{a}_{R_b} U = a_{R_b}\left(D_K + \hat{a}_{R_b} U\right) \tag{15}$$

$$a_{R_b} = \frac{\Delta D_K}{\Delta\Theta\left(D_K + \hat{a}_{R_b} U\right)} \tag{16}$$

Determined parameters in turn negative $\hat{a}_{Rb}$ (static identification $\dot{D}_K = 0$), and then „a_{Rb}“ (dynamic identification) and „b_{Rb}“ allow assessment of technical condition of the object „a_{Rb}“ and its relationship with environment „b_{Rb}“. It has been observed that the parameter of change of technical condition can be connected with parametric damage, thus, it is the symptom of parametric defects.

To calculate the parameter of adjustment state „a_{Rc}“ we use the equation of state:

$$\frac{dU}{d\Theta} = a_{R_c} U + b_{R_c} D_K \tag{17}$$

where: U – variable of adjustment state (utility signal), D_K variable of technical condition, a_{Rc} – parameter of adjustment state, b_{Rb} – parameter of technical condition (influence of environment) (Ashby, 1963; Girtler, 2003; Lindstedt and Sudakowski, 2007a).

According to principles of static and dynamic identification from the equation (17) we obtain:

$$U = \left(-\frac{b_{R_c}}{a_{R_c}}\right) D_K = \hat{a}_{R_c} D_K \tag{18}$$

$$\hat{a}_{R_c} = \frac{\Sigma D_{Ki} U_i}{\Sigma D_{Ki}^2} \tag{19}$$

and

$$\frac{\Delta U}{\Delta\Theta} = a_{R_c} U + a_{R_c} \hat{a}_{R_c} D_K = a_{R_c}\left(U + \hat{a}_{R_c} D_K\right) \tag{20}$$

$$a_{R_c} = \frac{\Delta U}{\Delta\Theta\left(U + \hat{a}_{R_c} D_K\right)} \tag{21}$$

Determined parameters in turn negative $\hat{a}_{Rc}$, and then „a_{Rc}“ (dynamic identification) and „b_{Rc}“ allow assessment of adjustment state of the object „a_{Rc}“ and its relationship with environment „b_{Rc}“. It has been observed that the parameter of change of adjustment state can be connected with momentary damage, thus, it is the symptom of momentary defects.

5. ASSESSMENT OF RELIABILITY OF A PUMP UNIT ON THE BASIS OF DIAGNOSTIC AND ADJUSTMENT INFORMATION

5.1. Structure and operation of a pump unit

In the course of operation of the object realised are periodical examinations consisting in measurement of following values: A (vibration amplitude), V (vibration velocity), f (variation frequency), I (current), p (pressure). Results of examination are shown in Tab. 1.

Tab. 1 proves that measured values are of various physical nature.

It is hard to make use of these values in equations (12) and (17) (in equations used are two values, and in the table there are five measured values).

Hence appears the need of reduction of all signals to consistent form, e.g. number of exceedings of statistic thresholds for individual values (Fig. 2).

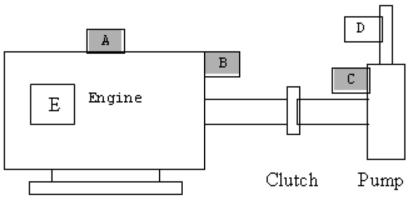

Fig. 1. Structure of a pump unit (A, B, C – points of installation of vibration accelerometers, D – manometer (pressure measurement), E – amperemeter (current measurement))

Tab. 1. Results of measurements characterising the state of pump unit

Working time	*A*	*V*	*f*	*I*	*p*
[h]	[m/s2]	[mm/s]	[1/s = Hz]	[A]	[MPa]
8329	48.000	24.000	0.64303	124	0.30
8354	40.500	20.500	0.60997	89	0.30
8401	45.000	25.000	0.56401	59	0.28
8442	24.000	17.000	0.43420	63	0.30
8487	45.000	26.000	0.54208	137	0.29
8496	42.000	18.500	0.69954	112	0.24
8531	42.000	21.500	0.60307	105	0.24
8578	39.000	19.000	0.63829	122	0.29
8602	39.000	19.250	0.64146	111	0.29
8648	30.000	14.000	0.69233	59	0.30
8675	30.000	18.000	0.53004	87	0.29
8699	24.000	17.000	0.43420	67	0.29
8744	25.500	22.000	0.35321	73	0.29
8769	30.000	18.500	0.52179	79	0.30
8819	24.000	19.000	0.38917	78	0.30
8838	31.500	17.000	0.39308	55	0.29
8861	24.000	15.500	0.49312	73	0.30
8909	33.000	25.500	0.41792	140	0.30
8937	33.000	25.500	0.41792	155	0.30
8982	39.000	19.000	0.63829	129	0.29
9006	34.500	17.500	0.63931	78	0.30
9029	42.000	21.500	0.60307	100	0.30
9079	30.000	19.000	0.51092	90	0.30
9097	42.000	20.500	0.64264	105	0.29
9121	34.500	17.500	0.63931	78	0.30
9235	24.000	15.500	0.49312	70	0.30
9256	24.000	15.500	0.49312	65	0.30
9278	33.000	17.750	0.59790	79	0.30
9322	39.000	19.000	0.63829	123	0.30
9333	31.500	17.000	0.60224	55	0.30

To reduce all signals to consistent form i.e. number of exceedings of statistic thresholds we use the formulas (22), (23):

$$S_1 = \sigma\sigma_t, N = \frac{S}{S_1} \tag{22}$$

$$N_{D_K} = \sqrt{N_A^2 + N_V^2 + N_f^2}, N_U = \sqrt{N_I^2 + N_p^2} \tag{23}$$

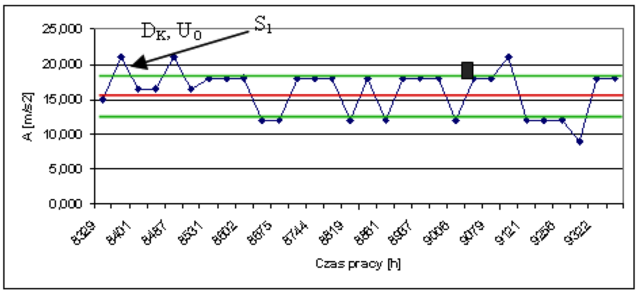

Fig. 2. Method of reduction of signals to the form of number of exceedings of statistic thresholds

Tab. 2. Numbers of exceedings of statistic thresholds

Work time	Vibration amplitude	Vibration velocity	Vibration frequency	Motor current	Pumping pressure	Complex diagnostic	Environment
Θ	n_{D_A}	n_{D_V}	n_{D_f}	n_{U_I}	n_{U_p}	N_{DK}	N_U
8329	**0.03065**	**0.00063**	0.00000	0.00000	0.00000	**0.03065**	0.00000
8354	0.00000	0.00000	0.00000	0.00000	0.00000	0.00000	0.00000
8401	**0.00701**	**0.01519**	0.00000	**0.17986**	0.00000	**0.01672**	**0.17986**
8442	**0.00584**	0.00000	**0.03160**	0.00000	0.00000	**0.03213**	0.00000
8487	**0.01051**	**0.02531**	0.00000	**0.26979**	0.00000	**0.02741**	**0.26979**
8496	0.00000	0.00000	**0.02565**	0.00000	**0.10461**	**0.02565**	**0.10461**
8531	0.00000	0.00000	0.00000	0.00000	**0.10461**	0.00000	**0.10461**
8578	0.00000	0.00000	0.00000	0.00000	0.00000	0.00000	0.00000
8602	**0.00467**	0.00000	**0.02816**	0.00000	0.00000	**0.02854**	0.00000
8648	0.00000	**0.01519**	**0.04324**	**0.04496**	0.00000	**0.04583**	**0.04496**
8675	0.00000	0.00000	0.00000	0.00000	0.00000	0.00000	0.00000
8699	**0.01751**	0.00000	0.00000	0.00000	0.00000	**0.01751**	0.00000
8744	**0.19848**	**0.24588**	**0.08548**	0.00000	0.00000	**0.32735**	0.00000
8769	0.00000	0.00000	**0.07040**	0.00000	0.00000	**0.07040**	0.00000
8819	**0.00701**	0.00289	**0.14733**	0.00000	0.00000	**0.14753**	0.00000
8838	**0.01637**	0.00000	**0.09251**	**0.21697**	0.00000	**0.09395**	**0.21697**
8861	**0.02447**	**0.00726**	0.00000	0.00000	0.00000	**0.02552**	0.00000
8909	0.00000	**0.06415**	**0.04412**	**0.20602**	0.00000	**0.07786**	**0.20602**
8937	0.00000	**0.05830**	0.00000	**0.12656**	0.00000	**0.05830**	**0.12656**
8982	0.00000	0.00000	0.00000	0.00000	0.00000	0.00000	0.00000
9006	**0.00567**	**0.00134**	0.00000	0.00000	0.00000	**0.00583**	0.00000
9029	0.00000	0.00000	0.00000	0.00000	0.00000	0.00000	0.00000
9079	0.00000	0.00000	0.00000	0.00000	0.00000	0.00000	0.00000
9097	0.00000	0.00000	0.00000	0.00000	0.00000	0.00000	0.00000
9121	**0.02149**	**0.01118**	0.00000	0.00000	0.00000	**0.02423**	0.00000
9235	**0.06075**	**0.02959**	0.00000	0.00000	0.00000	**0.06758**	0.00000
9256	**0.03875**	**0.01840**	**0.05274**	0.00000	0.00000	**0.06798**	0.00000
9278	0.00000	0.00000	**0.05208**	0.00000	0.00000	**0.05208**	0.00000
9322	0.00000	0.00000	0.00000	0.00000	0.00000	0.00000	0.00000
9333	**0.00154**	0.00000	**0.01140**	**0.00771**	0.00000	**0.01150**	**0.00771**

5.2. Assessment of reliability of a pump unit on the basis of parametric defects

Tab. 3. Values of the parameter „a_{Rb}“ as symptoms of parametric defects

Working time	Complex diagnostic	Environment	$\hat{a}_{R_b}$	a_{R_b}
Θ [h]	D_K	U		
8329	0.03065	0.00000	-0.80973	0.00012
8354	0.03065	0.00000	-0.80973	0.00000
8401	0.04738	0.17986	-0.80973	-0.00002
8442	0.07951	0.17986	-0.80973	-0.00006
8487	0.10691	0.44965	-0.80973	-0.00001
8496	0.13256	0.55426	-0.80973	-0.00001
8531	0.13256	0.65887	-0.80973	0.00000
8578	0.13256	0.65887	-0.80973	0.00000
8602	0.16110	0.65887	-0.80973	-0.00001
8648	0.20694	0.70383	-0.80973	-0.00001
8675	0.20694	0.70383	-0.80973	0.00000
8699	0.22445	0.70383	-0.80973	-0.00001
8744	0.55180	0.70383	-0.80973	-0.00207
8769	0.62220	0.70383	-0.80973	0.00015
8819	0.76973	0.70383	-0.80973	0.00008
8838	0.86368	0.92080	-0.80973	0.00009
8861	0.88920	0.92080	-0.80973	0.00002
8909	0.96705	1.12682	-0.80973	0.00016
8937	1.02536	1.25338	-0.80973	0.00062
8982	1.02536	1.25338	-0.80973	0.00000
9006	1.03118	1.25338	-0.80973	0.00004
9029	1.03118	1.25338	-0.80973	0.00000
9079	1.03118	1.25338	-0.80973	0.00000
9097	1.03118	1.25338	-0.80973	0.00000
9121	1.05541	1.25338	-0.80973	0.00007
9235	1.12299	1.25338	-0.80973	0.00007
9256	1.19097	1.25338	-0.80973	0.00004
9278	1.24305	1.25338	-0.80973	0.00002
9322	1.24305	1.25338	-0.80973	0.00000
9333	1.25455	1.26109	-0.80973	0.00001

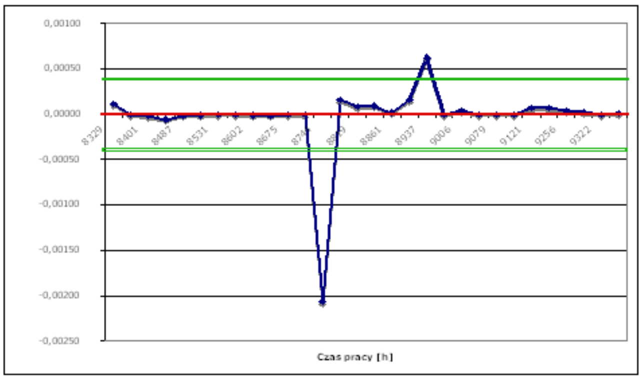

Fig. 3. Variation of the parameter „a_{Rb}“ (red line – average, green line – standard deviation)

Using the relation (16) and results of measurements shown in the table we have determined the parameter of technical condition a_{Rb}, which can be determined as the symptom of parametric defects. Values of the parameter a_{Rb} are shown in Tab. 3.

Regarding the exceeding of statistic threshold as the symptom of parametric damage we can determine the estimators of reliability function R_b^*.

Tab. 4. Values of estimators of reliability and fallibility functions for $\mu + \sigma$ (n – number of measurements (30 for 1000 hrs, then 300 for 10000 hrs)

Working time	a_{R_b}	$n_{Rb}(t)$	n	$P_b^*(t)$	$R_b^*(t)$
Θ [h]		number of symptoms			
8329	0.00012	0	300	0.00000	1.00000
8354	0.00000	0	300	0.00000	1.00000
8401	-0.00002	0	300	0.00000	1.00000
8442	-0.00006	0	300	0.00000	1.00000
8487	-0.00001	0	300	0.00000	1.00000
8496	-0.00001	0	300	0.00000	1.00000
8531	0.00000	0	300	0.00000	1.00000
8578	0.00000	0	300	0.00000	1.00000
8602	-0.00001	0	300	0.00000	1.00000
8648	-0.00001	0	300	0.00000	1.00000
8675	0.00000	0	300	0.00000	1.00000
8699	-0.00001	0	300	0.00000	1.00000
8744	-0.00207	1	300	0.00333	0.99667
8769	0.00015	1	300	0.00333	0.99667
8819	0.00008	1	300	0.00333	0.99667
8838	0.00009	1	300	0.00333	0.99667
8861	0.00002	1	300	0.00333	0.99667
8909	0.00016	1	300	0.00333	0.99667
8937	0.00062	2	300	0.00667	0.99333
8982	0.00000	2	300	0.00667	0.99333
9006	0.00004	2	300	0.00667	0.99333
9029	0.00000	2	300	0.00667	0.99333
9079	0.00000	2	300	0.00667	0.99333
9097	0.00000	2	300	0.00667	0.99333
9121	0.00007	2	300	0.00667	0.99333
9235	0.00007	2	300	0.00667	0.99333
9256	0.00004	2	300	0.00667	0.99333
9278	0.00002	2	300	0.00667	0.99333
9322	0.00000	2	300	0.00667	0.99333
9333	0.00001	2	300	0.00667	0.99333

5.3. Assessment of reliability of a pump unit on the basis of momentary defects

Using the relation (21) and results of measurements shown in the table we have determined the parameter of adjustment state a_{Rc}, which can be determined as the symptom of momentary defects. Values of parameter a_{Rc} are shown in Tab. 5.

Regarding the exceeding of statistic threshold as the symptom of parametric damage we can determine the estimators of reliability function R_c^*.

Tab. 5. Values of the parameter „a_{Rc}“ as symptom sof momentary defects

Working time	Complex diagnostic	Environment	a_{R_c}	a_{R_c}
Θ [h]	D_K	U		
8329	0.03065	0.00000	-0.80973	-0.00015
8354	0.03065	0.00000	-0.80973	0.00000
8401	0.04738	0.17986	-0.80973	0.00001
8442	0.07951	0.17986	-0.80973	0.00003
8487	0.10691	0.44965	-0.80973	0.00001
8496	0.13256	0.55426	-0.80973	0.00001
8531	0.13256	0.65887	-0.80973	0.00000
8578	0.13256	0.65887	-0.80973	0.00000
8602	0.16110	0.65887	-0.80973	0.00001
8648	0.20694	0.70383	-0.80973	0.00001
8675	0.20694	0.70383	-0.80973	0.00000
8699	0.22445	0.70383	-0.80973	0.00000
8744	0.55180	0.70383	-0.80973	0.00015
8769	0.62220	0.70383	-0.80973	0.00004
8819	0.76973	0.70383	-0.80973	0.00021
8838	0.86368	0.92080	-0.80973	0.00005
8861	0.88920	0.92080	-0.80973	0.00001
8909	0.96705	1.12682	-0.80973	0.00003
8937	1.02536	1.25338	-0.80973	0.00002
8982	1.02536	1.25338	-0.80973	0.00000
9006	1.03118	1.25338	-0.80973	0.00000
9029	1.03118	1.25338	-0.80973	0.00000
9079	1.03118	1.25338	-0.80973	0.00000
9097	1.03118	1.25338	-0.80973	0.00000
9121	1.05541	1.25338	-0.80973	0.00001
9235	1.12299	1.25338	-0.80973	0.00002
9256	1.19097	1.25338	-0.80973	0.00003
9278	1.24305	1.25338	-0.80973	0.00002
9322	1.24305	1.25338	-0.80973	0.00000
9333	1.25455	1.26109	-0.80973	0.00001

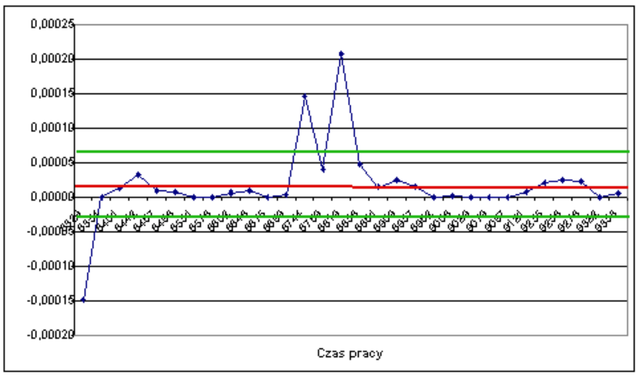

Fig. 4. Variation of the parameter „a_{Rc}“ (red line – average, green line –standard deviation)

Tab. 6. Values of estimators of reliability and fallibility functions for $\mu + \sigma$

Working time	a_{R_b}	$n_{Rb}(t)$	n	P_c*(t)	R_c*(t)
Θ [h]		number of symptoms			
8329	-0.00015	1	300	0.00333	0.99667
8354	0.00000	1	300	0.00333	0.99667
8401	0.00001	1	300	0.00333	0.99667
8442	0.00003	1	300	0.00333	0.99667
8487	0.00001	1	300	0.00333	0.99667
8496	0.00001	1	300	0.00333	0.99667
8531	0.00000	1	300	0.00333	0.99667
8578	0.00000	1	300	0.00333	0.99667
8602	0.00001	1	300	0.00333	0.99667
8648	0.00001	1	300	0.00333	0.99667
8675	0.00000	1	300	0.00333	0.99667
8699	0.00000	1	300	0.00333	0.99667
8744	0.00015	2	300	0.00667	0.99333
8769	0.00004	2	300	0.00667	0.99333
8819	0.00021	3	300	0.01000	0.99000
8838	0.00005	3	300	0.01000	0.99000
8861	0.00001	3	300	0.01000	0.99000
8909	0.00003	3	300	0.01000	0.99000
8937	0.00002	3	300	0.01000	0.99000
8982	0.00000	3	300	0.01000	0.99000
9006	0.00000	3	300	0.01000	0.99000
9029	0.00000	3	300	0.01000	0.99000
9079	0.00000	3	300	0.01000	0.99000
9097	0.00000	3	300	0.01000	0.99000
9121	0.00001	3	300	0.01000	0.99000
9235	0.00002	3	300	0.01000	0.99000
9256	0.00003	3	300	0.01000	0.99000
9278	0.00002	3	300	0.01000	0.99000
9322	0.00000	3	300	0.01000	0.99000
9333	0.00001	3	300	0.01000	0.99000

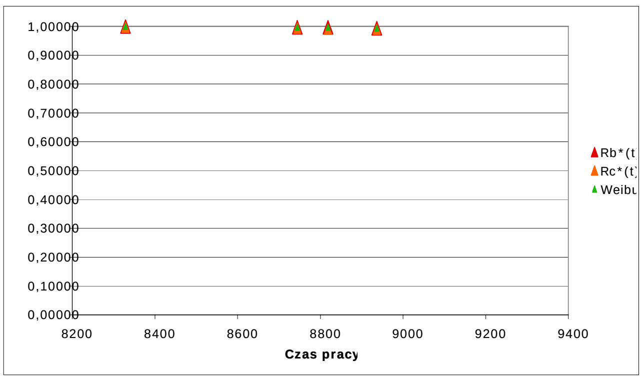

Fig. 5. Variation of estimators reliability $R(t)$ function and Weibull distribution $R(t)=e^{-at^b}$, where a=1 and b=1 with consideration of parametric defects and standard deviation for $\mu+\sigma$

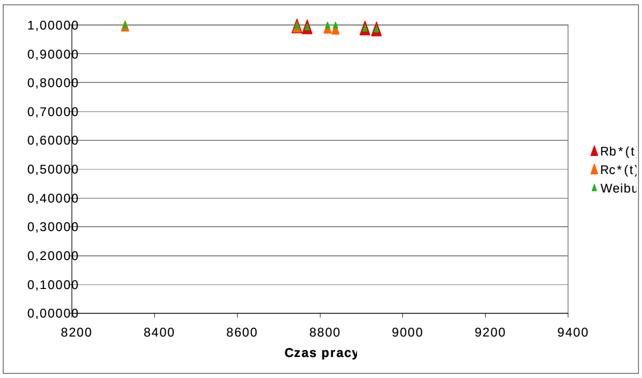

Fig. 6. Variation of estimators reliability $R(t)$ function and Weibull distribution $R(t)=e^{-at^b}$, where a=1 and b=1 with consideration of parametric defects and standard deviation for μ+0.5σ

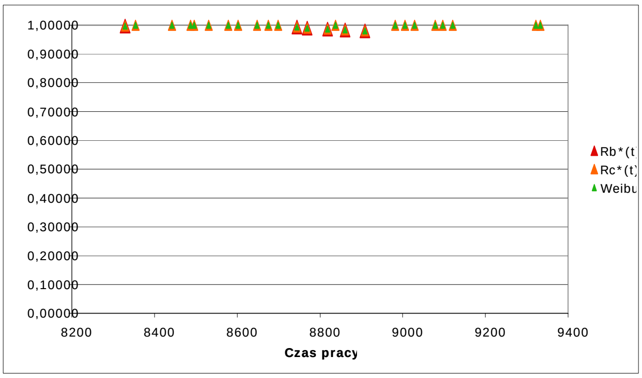

Fig. 7. Variation of estimators reliability R(t) function and Weibull distribution $R(t)=e^{-at^b}$, where a=1 and b=1 with consideration of parametric defects and standard deviation for μ+0.25

6. SUMMARY

The reliability characteristics are very important information determining the state of applicability of the object. The method of their determination is still an open problem, especially when the maintenance crew has no full information abort catastrophic, parametric and momentary defects. In the article presented is the innovative method of utilisation of operational information (presented in the form of numbers of exceedings of statistic thresholds" of utility, environment and accompanied signals) for determination of reliability characteristics. Presented method is very practical because allows verification of reliability characteristics without information about occurring catastrophic defects, which cannot occur in their pure form in the process of operation. Determined reliability characteristics should be analysed according to principles of diagnostics i.e. in connection with past characteristics of given object and with reliability characteristics of other objects of the same type.

REFERENCES

1. **Ashby R. V.** (1963), *Wstęp do cybernetyki*,. Warszawa.
2. **Bobrowski D.** (1985), *Modele i metody matematyczne teorii niezawodności w przykładach i zadaniach*, Warszawa.
3. **Girtler J.** (2003), Aspekty tworzenia modeli do prognozowania niezawodności systemów technicznych, Metody prognozowania w inżynierii niezawodności, *XXXI zimowa szkoła niezawodności*. Sekcja Podstaw Eksploatacji Komitetu Budowy Maszyn PAN, Szczyrk.
4. **Lindstedt P.** (2006), Kompleksowa diagnostyka w procesie oceny jekości użytkowania silnika śmigłowcowego w inżynieryjno – lotniczym otoczeniu, *Diagnostyka*, 3(39).
5. **Lindstedt P., Borowczyk H., Magier J.** (2003), Badanie możliwości kompleksowego diagnozowania układu łożyskowania na podstawie informacji uzyskanej z metod funkcjonalnej, tribologicznej i wibroakustycznej, *Projekt badawczy KBN Nr 5T12D01122*, sprawozdanie ITW nr 1371/50, Wyd. ITWL, Warszawa.
6. **Lindstedt P., Sudakowski T.** (2007a), Possibilities of assessment of reliability of an anthropotechnical system, *JVE Journal Of Vibroengineering*, Vol. 9, Issue 4.
7. **Lindstedt P., Sudakowski T.** (2007b), Prediction the bearing reliability on basis diagnostic information, *International Journal Of KONBiN*, 1(3).
8. **Lindstedt P., Sudakowski T.** (2008), Metod of prediction of realibility charakteristics of a pumping stadion on the base of diagnostic information, *Journal Of KONBiN*, 2(5), Vol. 2, Warsaw.
9. **Paton R., Frank P., Clark R.** (1989), *Fault diagnostic in dynamic systems. Theory and applications*, Cambridge University Press, London.
10. **Söderström T., Stoica P.** (1997), *Identyfikacja systemów*, PWN, Warszawa.
11. **Sotskow B. S.** (1973), *Niezawodność elementów i urządzeń automatyki*, WNT, Warszawa.
12. **Staniszewski R.** (1980), *Sterowanie zespołów napędowych.* WKŁ, Warszawa..
13. **Tomaszek H., Żurek J., Jasztal M.** (2008), *Prognozowanie uszkodzeń grożących bezpieczeństwu lotów statków powietrznych*, Wydawnictwo Naukowe Instytutu Technologii Eksploatacji – PIB, Warszawa.
14. **Zamojski W.** (1981), *Niezawodność i eksploatacja systemów*, Politechnika Wrocławska, Wrocław.
15. vlsi.imio.pw.edu.pl/pmk_W8_1.html

SELF-REGULAR STRESS INTEGRAL EQUATIONS METHOD FOR AXISYMMETRIC ELASTICITY

Heorhiy SULYM*, Iaroslav PASTERNAK**

* Mechanical Engineering and Applied Computer Department, Bialystok Technical University, 45C Wiejska Street, 15-351 Bialystok, Poland
**Lutsk National Technical University, Lvivska St., 75, 43018, Lutsk, Ukraine

sulym@pb.edu.pl, pasternak@ukrpost.ua

Abstract: The stress hypersingular integral equations of axisymmetric elasticity are considered. The singular and hypersingular integrals are regularized using the imposition of auxiliary polynomial solution, and self-regular integral equations are obtained for bounded and unbounded domains. The stress-BEM formulation is considered basing on the proposed equations. Considered numerical examples show high efficiency of the proposed approach. New problem for inclusion in finite cylinder is considered.

1. INTRODUCTION

The pioneering work concerning regularization of hypersingular stress integral equations for the axisymmetric elasticity was that by de Lacerda and Wrobel (2001). The further researches and a new more convenient solution strategy of the hypersingular equations with their previous regularization was presented by Mukherjee (2002). The last paper also presents practically full review of the major works concerning the boundary element method (BEM) and the integral equations for the axisymmetric elasticity.

The main aim of the above mentioned papers was the application of hypersingular integral equation as a basic one for the numerical scheme of BEM, therefore its regularization is not complete and still there are singular integrals, which principal values are to be evaluated using special techniques. Therefore, the regularization approaches of Mukherjee (2002); de Lacerda and Wrobel (2001) are actually unsuitable for calculation of stresses in the whole domain continuously up to the boundary, because of the boundary layer effect, which arise due to the numerical integration of nearly-singular integrals (Cruse, 1969). For this purpose, it is necessary to provide full regularization of both singular and hypersingular integrals.

2. FORMULATION AND SOLUTION OF THE PROBLEM

Consider the linear elastic isotropic solid B bounded by the surface ∂B. Assume that B is axially symmetric and symmetrically loaded with the respect to the axis of symmetry Oz. The integral equation for determination of stresses in an internal source point $\boldsymbol{\xi} \in B, \boldsymbol{\xi} \notin \partial B$ according to (de Lacerda and Wrobel, 2001) can be written as:

$$\sigma_{ij}(\boldsymbol{\xi}) = \\ = \int_{\Gamma} \alpha(\mathbf{x}) \left[D_{ijk}(\boldsymbol{\xi},\mathbf{x}) t_k(\mathbf{x}) - S_{ijk}(\boldsymbol{\xi},\mathbf{x}) u_k(\mathbf{x}) \right] d\Gamma(\mathbf{x}), \quad (1)$$

where i, j, k = r, z; $\boldsymbol{\sigma}$, $\mathbf{t}$, $\mathbf{u}$ are the stress tensor, traction and displacement vectors, respectively; $\alpha(\mathbf{x})=2\pi r(\mathbf{x})$; Γ is a curve formed by the intersection of the boundary ∂B with an axial plane; $r(\mathbf{x})$ is the distance between point x and axis Oz. Kernels D_{ijk} and S_{ijk} are discussed and explicitly written in (de Lacerda and Wrobel, 2001).

When the source point $\boldsymbol{\xi} \in B$ limits some boundary point $\mathbf{x} \in \partial B$, that is when $\|\mathbf{x} - \boldsymbol{\xi}\| \to 0$, the kernel function $\mathbf{D}$ becomes singular of a type $O(1/\|\mathbf{x} - \boldsymbol{\xi}\|)$, and a kernel function $\mathbf{S}$ hypersingular of a type $O(1/\|\mathbf{x} - \boldsymbol{\xi}\|)^2$ (de Lacerda and Wrobel, 2001). Thus, when calculating stresses or deformations in a point, which is placed close enough to the boundary, the integrand in the equation (1) will intensively change in the neighborhood of the point $\mathbf{x}$=$\mathbf{y}$, where $\mathbf{y} \in \Gamma$ is the nearest to $\boldsymbol{\xi}$ boundary point. The analytical calculation of integral (1) is not affected by this behavior of the integrand, so the correct result is obtained (the value of stress tensor). Nevertheless, in BEM the integral (1) is calculated numerically and the intensive variation of the integrand essentially reduces the accuracy of numerical integration. Thus, the boundary layer effect is observed: the error of stress or deformation calculations is intolerable in the points that are very close to the boundary. To eliminate the boundary layer effect, as it was shown for the 2D elastic problems in (Richardson and Cruse, 1999), it is necessary to use the self-regular boundary integral equations, so the full regularization is to be provided.

According to Mukherjee (2000, 2002) when $\boldsymbol{\xi} \to \mathbf{y} \in \Gamma$ the equation (1) can be rewritten as:

$$\sigma_{ij}(\mathbf{y}) + A_{ijk}u_k(\mathbf{y}) - C_{ijkp}u_{k,p}(\mathbf{y}) = \\ = \int_\Gamma \alpha(\mathbf{x}) D_{ijk}(\mathbf{y},\mathbf{x})\left[\sigma_{kp}(\mathbf{x}) - \sigma_{kp}(\mathbf{y})\right] n_p(\mathbf{x})\, d\Gamma(\mathbf{x}) - \\ - \int_\Gamma \alpha(\mathbf{x}) S_{ijk}(\mathbf{y},\mathbf{x})\left[u_k(\mathbf{x}) - u_k(\mathbf{y}) - \right. \\ \left. - u_{k,p}(\mathbf{y})\left(x_p - y_p\right)\right] d\Gamma(\mathbf{x}). \tag{2}$$

Here

$$A_{ijk} = \lim_{\xi \to \mathbf{y}} \int_\Gamma \alpha(\mathbf{x}) S_{ijk}(\xi,\mathbf{x})\, d\Gamma(\mathbf{x}), \\ C_{ijkp} = \lim_{\xi \to \mathbf{y}} \int_\Gamma \alpha(\mathbf{x})\left[E_{mlkp} D_{ijm}(\xi,\mathbf{x}) n_l(\mathbf{x}) - \right. \\ \left. - S_{ijk}(\xi,\mathbf{x})\left(x_p - \xi_p\right)\right] d\Gamma(\mathbf{x}) \tag{3}$$

are hypersingular and singular integrals respectively (according to the definition of (Mukherjee, 2000; Lin'kov 1999); the components of tensor **E** are defined by the expression $\sigma_{ij}=E_{ijkm}u_{k,m}$. Integrals in the right hand side of (2), according to Mukherjee (2000) and Lin'kov (1999), are regular. The presented in (Mukherjee, 2002; de Lacerda and Wrobel, 2001) approaches are engaged in calculation of integrals (3).

To withdraw the evaluation of singular and hypersingular integrals another regularization approach for equation (1) should be used. If such auxiliary solution of axisymmetric elasticity can be found that its superposition with (1) gives zero values of $u_k(\mathbf{y})$ and $u_{k,p}(\mathbf{y}$ in boundary point $\mathbf{y}$, then in expression (2) the terms with tensors A_{ijk} and C_{ijkp} vanishes. Moreover, when the source point ξ is located close to $\mathbf{y} \in \Gamma$, such representation, according to (Richardson and Cruse, 1999), will eliminate the boundary layer effect.

The auxiliary solution $\mathbf{u}^*(\xi, \mathbf{y})$ must satisfy the partial differential equations of the problem (e.g. see Timošenko, 1972)

$$\frac{1}{1-2\nu}\frac{\partial}{\partial r}\left(\frac{\partial u_r}{\partial r} + \frac{\partial u_z}{\partial z} + \frac{u_r}{r}\right) + \frac{\partial^2 u_r}{\partial z^2} + \frac{\partial}{\partial r}\left(\frac{\partial u_r}{\partial r} + \frac{u_r}{r}\right) = 0; \\ \frac{1}{1-2\nu}\frac{\partial}{\partial z}\left(\frac{\partial u_r}{\partial r} + \frac{\partial u_z}{\partial z} + \frac{u_r}{r}\right) + \frac{\partial^2 u_z}{\partial z^2} + \frac{\partial^2 u_z}{\partial r^2} + \frac{1}{r}\frac{\partial u_z}{\partial r} = 0, \tag{4}$$

and the displacements u^*_i along with their partial derivatives $u^*_{i,k}$ in a point $\mathbf{y}$ are to be equal to the corresponding values of the considered problem (1). The simplest way to obtain this auxiliary solution is to use the polynomial one. It is easy to verify by direct substitution, that the displacement field with the following structure

$$u_r^* = C_1 r + C_2 rz + C_3 r^3, \\ u_z^* = C_4 + C_5 z + C_6\left[z^2(1-2\nu) - r^2(1-\nu)\right] - \frac{0.5 C_2 r^2}{1-2\nu} - \\ - \frac{1}{1-2\nu}\left[8C_3 z\left(r^2\left(1-3\nu+2\nu^2\right) - \frac{1}{3}z^2(1-2\nu)^2\right)\right] \tag{5}$$

satisfies the partial differential equations (4) and consequently can be used as an elementary solution for imposition. Here ν is a Poisson ratio.

The factors C_k can be determined using the mentioned above conditions:

$$u_i^*(\mathbf{y}) = u_i(\mathbf{y}); \; u_{i,j}^*(\mathbf{y}) = u_{i,j}(\mathbf{y}). \tag{6}$$

By substitution of equations (5) in (6) and solution of the resulting system of linear algebraic equations, the explicit expressions for the factors C_k can be obtained:

$$C_1 = \left(3u_r - 2u_{r,z}z - u_{r,r}r\right)/(2r), \\ C_2 = u_{r,z}/r, \; C_3 = \left(u_{r,r}r - u_r\right)/\left(2r^3\right), \\ C_4 = u_z - u_{z,z}z - \left(u_{r,z}z^2 + \left(\alpha z^2 + \beta r^2\right)u_{z,r}\right)/(2r\beta) + \\ + 4z\left(\alpha z^2 + 3\beta r^2\right)\left(u_r - u_{r,r}r\right)/\left(3r^3\right), \\ C_5 = u_{z,z} + z\left(u_{r,z} + \alpha u_{z,r}\right)/(r\beta) - \\ - 4\left(\alpha z^2 + \beta r^2\right)\left(u_r - u_{r,r}r\right)/r^3, \\ C_6 = 4z\left(u_r - u_{r,r}r\right)/r^3 - \left(u_{r,z} + \alpha u_{z,r}\right)/(2r\alpha\beta), \tag{7}$$

where $r=r(\mathbf{y})$, $z=z(\mathbf{y})$, $u_i= u_i(\mathbf{y})$, $u_{i,j}= u_{i,j}(\mathbf{y})$, α=1-2ν, β=1-ν.

It should be mentioned that conditions (6) are insufficient for determination of C_k, when the regularization point $\mathbf{y}$ is placed on the axis of symmetry Oz. In this case, taking into account that for r=0 nonzero are only u_z, $u_{z,z}$, $u_{r,r}$, the factors C_k can be defined as follows:

$$C_2 = C_3 = C_6 = 0; \; C_1 = u_{r,r}(\mathbf{y}); \\ C_4 = u_z(\mathbf{y}) - z(\mathbf{y})u_{z,z}(\mathbf{y}); \; C_5 = u_{z,z}(\mathbf{y}). \tag{8}$$

This choice satisfies conditions (6) with the reference that the regularization point $\mathbf{y}$ is placed on the symmetry axis Oz.

In terms of (1), the stresses, which are induced by the elastic displacements (5), equal

$$\sigma_{ij}^*(\xi) = \\ = \int_\Gamma \alpha(\mathbf{x})\left[D_{ijk}(\xi,\mathbf{x}) t_k^*(\mathbf{x}) - S_{ijk}(\xi,\mathbf{x}) u_k^*(\mathbf{x})\right] d\Gamma(\mathbf{x}). \tag{9}$$

Subtracting equation (9) from (1), the following stress integral equation is obtained:

$$\sigma_{ij}(\xi) = \sigma_{ij}^*(\xi) + \\ + \int_\Gamma \alpha(\mathbf{x}) D_{ijk}(\xi,\mathbf{x})\left[t_k(\mathbf{x}) - t_k^*(\mathbf{x})\right] d\Gamma(\mathbf{x}) - \\ - \int_\Gamma \alpha(\mathbf{x}) S_{ijk}(\xi,\mathbf{x})\left[u_k(\mathbf{x}) - u_k^*(\mathbf{x})\right] d\Gamma(\mathbf{x}). \tag{10}$$

Considering (6) and the Hook's law it follows that $t_k(\mathbf{y})-t_k^*(\mathbf{y})=0$. Also from (6) it directly follows that $u_k(\mathbf{y})-u_k^*(\mathbf{y})=0$ and $u_{k,p}(\mathbf{y})-u_{k,p}^*(\mathbf{y})=0$. Thus the representation (10), according to (Mukherjee, 2000; Lin'kov, 1999), completely regularize singular and hypersingular integrals which arise in (1) when the source point $\xi \in B$ limits point $\mathbf{y}$ on boundary ∂B. Besides, the self-regular integral equation (10) makes it possible to eliminate the boundary layer effect and to calculate stresses extremely close to the boundary of a solid and even on it. Equation (10) can be also used as the basic integral equation for the numerical scheme of BEM to solve the axisymmetric elastic problems, including those of fracture mechanics. Full regularization (10) permits to avoid thus calculation of the principal value integrals that is necessary to do using those BEM schemes of (Mukherjee, 2002; de Lacerda and Wrobel, 2001).

As for the infinite medium, the integral representation of stress tensor components (10) cannot be applied and should be slightly modified. Assume that a solid is bounded with the surface $\Gamma_\Sigma = \Gamma_R \cup \Gamma$, where Γ is a boundary of voids and Γ_R is a sphere of a radius R. Integration of (10) over the surface Γ_Σ and the limiting procedure when $R \to \infty$ gives

$$\begin{aligned}\sigma_{ij}(\boldsymbol{\xi}) &= \sigma_{ij}^{\text{hom}}(\boldsymbol{\xi}) + \\ &+ \int_\Gamma \alpha(\mathbf{x}) D_{ijk}(\boldsymbol{\xi},\mathbf{x})\left[t_k(\mathbf{x}) - t_k^*(\mathbf{x})\right] d\Gamma(\mathbf{x}) - \\ &- \int_\Gamma \alpha(\mathbf{x}) S_{ijk}(\boldsymbol{\xi},\mathbf{x})\left[u_k(\mathbf{x}) - u_k^*(\mathbf{x})\right] d\Gamma(\mathbf{x}),\end{aligned} \tag{11}$$

where $\sigma_{ij}^{\text{hom}}(\boldsymbol{\xi})$ is a homogenous solution of the problem for the infinite medium without voids. That is the problem is reduced to the analysis of the perturbation influence of voids, which are bounded domains.

3. STRESS BEM FORMULATION

Integral equations (10) and (11) due to the applied regularization technique are continuous to the boundary. Though the limit procedure of $\boldsymbol{\xi} \to \mathbf{y} \in \Gamma$ can be done by simple substitution. Taking into account that for the regularization point $\mathbf{y}$ according to (6) and Hook's law $\boldsymbol{\sigma}(\mathbf{y})=\boldsymbol{\sigma}^*(\mathbf{y})$ the following integral equations are obtained from (10) for bounded domains

$$\begin{aligned}0 &= \int_\Gamma \alpha(\mathbf{x}) D_{ijk}(\mathbf{y},\mathbf{x})\left[t_k(\mathbf{x}) - t_k^*(\mathbf{x})\right] d\Gamma(\mathbf{x}) - \\ &- \int_\Gamma \alpha(\mathbf{x}) S_{ijk}(\mathbf{y},\mathbf{x})\left[u_k(\mathbf{x}) - u_k^*(\mathbf{x})\right] d\Gamma(\mathbf{x})\end{aligned} \tag{12}$$

and from (11) for unbounded domains

$$\begin{aligned}\sigma_{ij}(\mathbf{y}) - \sigma_{ij}^{\text{hom}}(\mathbf{y}) &= \\ &= \int_\Gamma \alpha(\mathbf{x}) D_{ijk}(\mathbf{y},\mathbf{x})\left[t_k(\mathbf{x}) - t_k^*(\mathbf{x})\right] d\Gamma(\mathbf{x}) - \\ &- \int_\Gamma \alpha(\mathbf{x}) S_{ijk}(\mathbf{y},\mathbf{x})\left[u_k(\mathbf{x}) - u_k^*(\mathbf{x})\right] d\Gamma(\mathbf{x}).\end{aligned} \tag{13}$$

For the solution of equations (12) or (13) the standard BEM procedure (see Richardson and Cruse, 1999) is applied. Unknown derivatives of displacements $u_{i,j}$ are obtained using Hook's law from the following system of equations

$$\begin{cases} \dfrac{2G\nu n_1(\eta)}{1-2\nu} u_{2,2} + \dfrac{2G(1-\nu)}{1-2\nu} n_1(\eta) u_{1,1} + \\ \qquad + G n_2(\eta)\left(u_{1,2} + u_{2,1}\right) = t_1 - \dfrac{2G\nu n_1(\eta)}{1-2\nu}\dfrac{u_1}{r}, \\ \dfrac{2G\nu n_2(\eta)}{1-2\nu} u_{1,1} + \dfrac{2G(1-\nu)}{1-2\nu} n_2(\eta) u_{2,2} + \\ \qquad + G n_1(\eta)\left(u_{1,2} + u_{2,1}\right) = t_2 - \dfrac{2G\nu n_2(\eta)}{1-2\nu}\dfrac{u_1}{r}, \\ -u_{1,1} n_2(\eta) J(\eta) + u_{1,2} n_1(\eta) J(\eta) = u_{1,\eta}, \\ -u_{2,1} n_2(\eta) J(\eta) + u_{2,2} n_1(\eta) J(\eta) = u_{2,\eta}, \end{cases} \tag{14}$$

where G is shear modulus; $n_i(\eta)$ are the components of unit normal vector to the boundary element; η is a boundary element parameter; $J(\eta)$ is a Jacobian of the considered boundary element. Derivatives $u_{i,\eta}$ are obtained directly from the used approximation, e.g. if displacements on the element are given as

$$u_i = \sum_{p=1}^{n} N^p(\eta) u_i^p,$$

then $u_{i,\eta}$ equals

$$u_{i,\eta} = \frac{du_i}{d\eta} = \sum_{p=1}^{n} \frac{d}{d\eta} N^p(\eta) u_i^p,$$

where $N^p(\eta)$ are base functions.

All the rest of BEM procedure is standard (see Richardson and Cruse, 1999).

4. NUMERICAL EXAMPLES

To demonstrate the efficiency of the proposed regularization technique for calculation of the stress field let us consider numerical examples for the unbounded and bounded domains.

As an example of the unbounded domain consider the perturbation of the stress field by the spherical cavity of the radius R in the infinite elastic isotropic medium that is loaded on infinity by the homogeneous stresses q acting along axis Oz. According to (Barber, 2004) the maximum stresses on the boundary of the cavity for such loading equal

$$\sigma_{zz} = \frac{27-15\nu}{2(7-5\nu)} q.$$

For the BEM model of this problem 5 quadratic isoparametric boundary elements are used. The boundary nodes are uniformly distributed. The relative error of σ_{zz} determination by the equation (11) on the boundary of the cavity at a point (r=R, z=0) is less, than 0.2 %. At the same time the ordinary stress equation (1) gives a considerable error even far enough from the boundary of a cavity. Fig. 1 shows the values of stress tensor component $\sigma_{zz}(\boldsymbol{\xi})$ on the axis Or, when $x=r(\boldsymbol{\xi})$ comes close to R.

It can be seen from Fig. 1, that ordinary stress equation (1) gives good results only for the points that are far enough from the boundary. When the source point approaches the boundary, due to the calculation errors, the solution begins to oscillate, and the received values can differ from the true one even in ten times. The regularized equation (11) gives good values in the whole domain. The continuous curve on the plot practically coincides with the analytical solution of the problem (Barber, 2004) (it is not possible to distinguish these results on the plot).

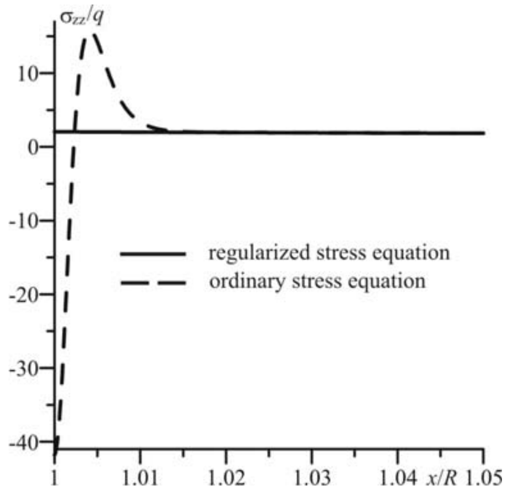

Fig. 1. Determination of stress field near the spherical cavity using
the regularized and ordinary stress integral equations

As an example of a problem with the bounded domain, consider the Lame problem. Its solution can be found, for example, in (Timošenko, 1972). For numerical solution the following parameters are used: the ration of internal and external pressure is p_1/p_2=0,5; the ratio of internal and external radius is R_1/R_2=0,6. For the axisymmetric BEM model the length of a pipe was equal 4 R_2. The maximum relative error of the hoop stresses $\sigma_{\theta\theta}$ determination using the self-regular equation (10) is less than 0.8 %. Corresponding plots of change of these stresses with the thickness of the pipe received by equations (1), (10) and analytical solution (Timošenko, 1972) are shown on Fig. 2.

It can be noticed (Fig. 2), that the hoop stress $\sigma_{\theta\theta}$ received using the ordinary stress equation (1) more than in 100 times differs from the true one. The curves received by the formula (10) and analytical solution of the problem practically coincide.

Now consider a new problem for a finite cylinder with an ellipsoidal elastic inclusion. It is well known that if the ellipsoidal inclusion is bonded into infinite medium the stress field in it is constant (Eshelby, 1957). It is interesting to obtain the influence of cylinder size on the stress field in inclusion and to obtain the size, for which this field is nearly constant.

Consider the cylinder of a radius R and heights $2R$. In the center of cylinder the ellipsoidal inclusion of length a and heights b is placed (a/b=10). The Poisson ratios of cylinder and inclusion are equal 0.3. The ratio of Young's modulus of inclusion and cylinder is denoted by k. The relative size of inclusion is $\lambda = a/R$. The scheme
of the problem and stress deviations

$$\delta\sigma_{ij} = \left[\sigma_{ij}(\lambda) - \sigma_{ij}(0)\right] / \sigma_{ij}(0) \cdot 100\%$$

are plotted in Fig. 3. Hear $\sigma_{ij}(0)$ are the stresses for inclusion in infinite medium (Eshelby, 1957).

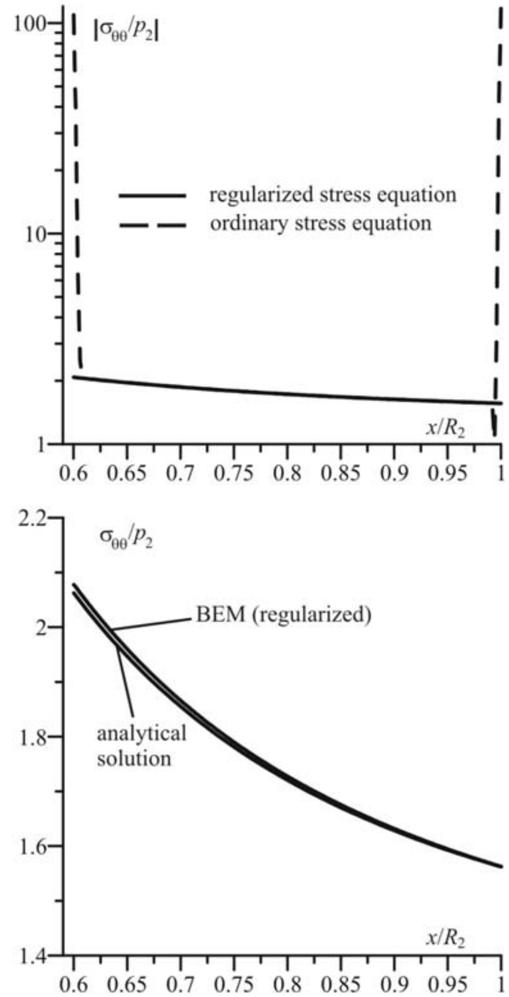

Fig. 2. The BEM and analytical solution of the Lame problem

Stress deviations at the center O of inclusion are denoted by continuous curves, at the point A by dashed curves, and at point B by dash-dot. It can be seen that for the inclusion in cylinder stresses at its center are little greater than those on the surface. The influence of size is greater for soft inclusions ($k < 1$). Fig. 3 shows that with an error of 10 % the solution (Eshelby, 1957) for the infinite medium can be applied to the problem of finite cylinder if the relative size of inclusion is less than 0.4. If the error should be less than 5 % then $\lambda < 0.2$, less than 1 % – $\lambda < 0.1$.

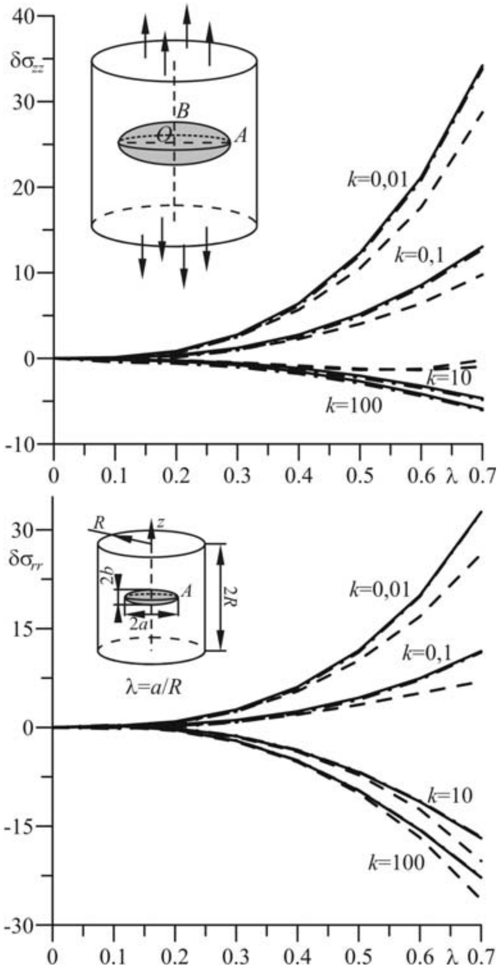

Fig. 3. Stress deviation in inclusion inside the cylinder

5. CONCLUSION

The ordinary hypersingular integral equations of axisymmetric elasticity actually do not suite when the stress field is determined close enough to the boundary of a solid. Due to the numerical integration of nearly-singular integrals, which are crucial for the accuracy, the computational error of ordinary equations is intolerable and the received values are in tens to hundreds times greater, than the true ones. So, instead of ordinary one the self-regular integral equations are to be used. Using the polynomial solution of the partial differential equations of the problem both singular and hypersingular integrals can be regularized and self-regular integral equations are received for both bounded and unbounded domains. These equations are utilized in the new self-regular stress BEM formulation. The numerical procedure of this BEM has much in common with one for 2D elasticity. The peculiarities of the new BEM are discussed separately. Presented numerical examples show high efficiency of the proposed integral equations. New results are obtained for the problem of ellipsoidal inclusion in cylinder.

REFERENCES

1. **Barber J. R.** (2004), *Elasticity*, Kluwer Academic Publishers.
2. **Cruse T. A.** (1969), Numerical solutions in three dimensional elastostatics, *Int. J. of Solids & Structures*, Vol. 5, 1259–1274.
3. **de Lacerda L. A., Wrobel L. C.** (2001), Hypersingular boundary integral equations for axisymmetric elasticity, *Int. J. Numer. Meth. Eng.*, Vol. 52, 1337–1354.
4. **Eshelby J. D.** (1957), The Determination of the elastic field of an ellipsoidal inclusion, and related problems, *Proc. Royal Soc. London*, A241, 376–396.
5. **Lin'kov A. M.** (1999), *Kompleksnyj metod graničnyh elementov*, Nauka, Sankt-Peterburg.
6. **Mukherjee S.** (2000), Finite parts of singular and hypersingular integrals with irregular boundary source points, *Eng. Anal. with Boundary Elements*, Vol. 24, 767–776.
7. **Mukherjee S.** (2002), Regularization of hypersingular boundary integral equations: a new approach for axisymmetric elasticity, *Eng. Anal. with Boundary Elements*, Vol. 26, 839–844.
8. **Richardson J. D., Cruse T. A.** (1999), Weakly singular stress-BEM for 2D elastostatics, Int. J. Num. Meth. Eng., Vol. 45, No. 1, 13–35.
9. **Timošenko S. P.** (1972), *Kurs teorii uprugosti*, Naukova dumka, Kiev.

The work was supported by the State Committee for Scientific Research of Poland under grant No. 7 T07C 006 12.

BALL PUMP

Kirill VOYNOV[*], Helen CHERTOK[*]

Mechanical Faculty, Petersburg State Transport University, 190031,ST Petersburg, 9, Moskovsky pr., Russia

forstar@mail.ru, forstar@mail.ru

Abstact: A new and very effective ball pump is created. It can pump across the different liquids, for example: water, lubricants, oil, glycerine and even blood. Moreover it works not only like a pump but as a hydro-machine which can be applied in the various systems, namely, locomotives, robots and so on.

1. INTRODUCTION

There are very many types of pumps in the world and they have a lot of pairs of friction inside their bodies. It decreases the reliability and durability of pumps. That's why the main aim which we demonstrate in this article is the next: how to increase the operation life for a pump and how to make it more effective in practice. This important task is solved by means of improvement of the design.

2. NEW DESIGN

The new ball pump doesn't have any valves; it has minimum pairs of friction, can work as a hydro-machine, be reversible, and has a very high productivity. The pump design has a very small amount of basic parts only – body, rotor which has a shaft with two discs. There are four windows on the ball pump. Two of them stand duty as windows for injection of liquid and the others two are to throw the liquid out of the body. The volume which the ball pump can pump across is proportional to the diameter of a ball in the third power. Both the alteration of the direction for the liquid stream and the productivity adjustment in a ball pump can be realized by means of change of the discs' inclines relatively each other. This new ball pump in its design doesn't have any complicated junctions (Fig. 1).

Two discs 1 and 2 inside the ball pump divide the volume into four chambers (4-7) which are connected with the windows 3 for injection and to throw any liquid out. For this purpose in each window there is a coupling for the hose. When the shaft 9 rotates clockwise, the disc 1 opens two windows 3 and the volumes of chambers 4 and 6 begins to diminish and liquid from them is being forced out. At the same time the volumes in two chambers 5 and 7 are increasing and liquid in these chambers is being soaked through. These actions will be stopped when disc 1 closes appropriate windows 3 (after the moment when the shaft 9 made the turning on the 180^0). After it the role for the chambers 4 and 6 becomes another as for the chambers 5 and 7. Further the cycle will be repeated many times.

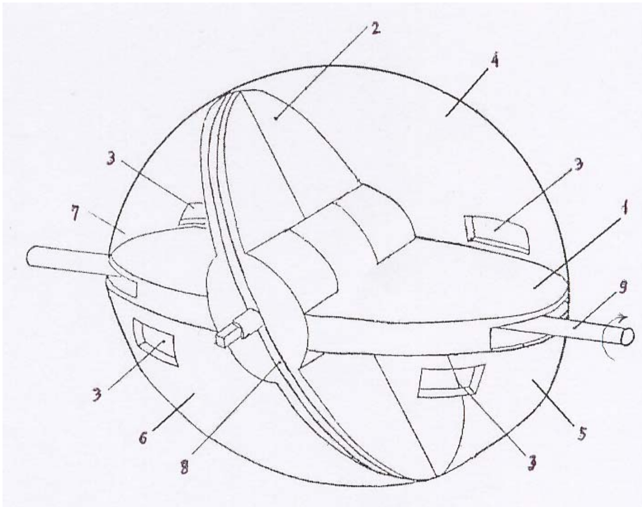

Fig. 1. The design of the new ball pump: 1 and 2 – discs which are connected by hinge; 4, 5, 6 and 7 are chambers which are joined with the windows 3; 8 - adjusting ring; 9 – shaft

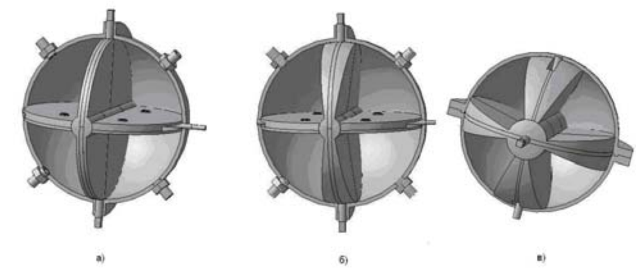

Fig. 2. Ball pump: а) old type with the flat discs; б), в) discs with the special shapes

Turning disc 2 by using adjusting ring 8 we can get the equal volumes in chambers when the angle between of two dicks will be 90^0. But if we continue the turn of the disc 2 in the same direction then the way of movement for liquid will be changed in the opposite direction instantaneously.

The analog of the new ball pump was suggested some years ago in Russia (reader B.A. Dezhinov) and it was named as a "pump for the artificial heart". But in the old version in one position the pump couldn't throw liquid out in full. Professor K. Voynov changed the shape of the discs made them like a cone (Fig. 2) (Патент 79619, 2009). In this case any liquid is being deleted constantly and completely.

3. THEORETICAL PART AND EXPERIMENT

The formula to the ideal feed for the pump (m^3 per hour) is the next: $Q_u=60 \cdot V_0 \cdot n$, where V_0 is the working volume of the pump (m^3); n is the frequency of the rotation for the shaft.

V0=(Vk/V).z.k.(V – Vr),

where V_k is the ideal feed from the each working chamber during one cycle; $V=(4/3) \cdot \pi \cdot R^3$ is the inner volume of the pump; R is the inner radius of the pump; z=4 are the numbers of the working chambers; k=1 is the number of the feeds from each chamber during one rotation of the shaft; V_r is the volume for the pump rotor.

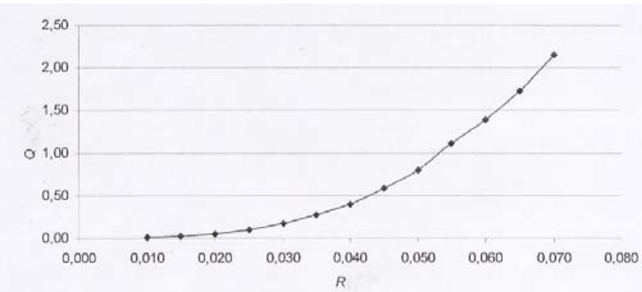

Fig. 3. Chart of the ideal feed Q of a pump-to-the inner radius R of the body ratio

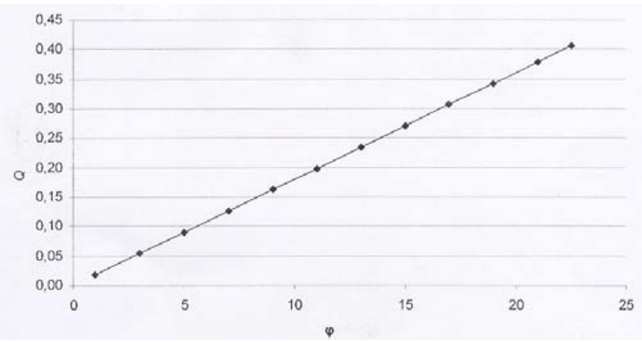

Fig. 4. Chart of the ideal feed Q of a pump-to-the angle φo ratio

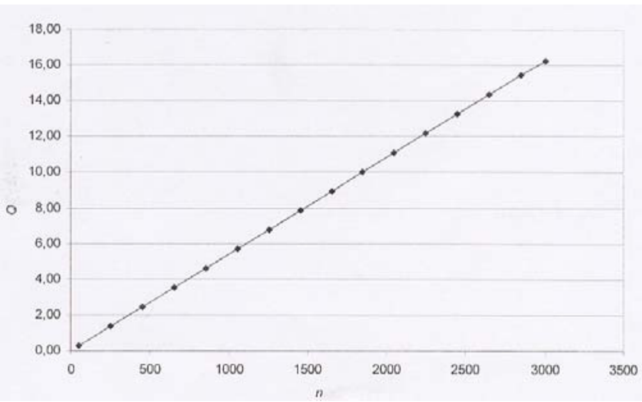

Fig. 5. Chart of the ideal feed Q of a pump-to-frequency n of rotor rotation ratio

Then $V_k=V_{max}–V_{min}=(4/3) \cdot R^3 \cdot \varphi$, φ is the angle of the incline for the driven disc which is counted out from the vertical axis, radian.

Finally the volume of rotor will be the next; $V_r=8 \cdot s \cdot (R^2 \cdot \arccos(a/R) - a \cdot \sqrt{(R^2 - a^2)}) - 8 \cdot b \cdot (r^2 \cdot \arccos(a/r) - s \cdot a) + 2 \cdot \pi \cdot r^2 \cdot b + (2/3) \cdot \pi \cdot (2 \cdot R^2 - r^2 - 2 \cdot R \cdot b) \cdot (2 \cdot R + b)$,

where s is the half of the disc's thickness; r is the radius of a hinge; $a=\sqrt{(r^2 - s^2)}$; $b=\sqrt{(R^2 - r^2)}$.

In Figures 3-5 there are three charts connected with the results of calculations.

The special experiments were made using a new apparatus (Fig. 6). Electric motor can change the speed of rotation. It results in the variation in a feed and a productivity of a ball pump. Because there are too little pairs of friction in the new pump (only one hinge) the reliability of this mechanical system is higher than there is in another known system. The effectiveness of a new ball pump was tested using different liquids, for example: water, oil, glycerine and even blood substitute. And at last the reliability of our ball pump is against than the same index for the prototype 1.26 times as large.

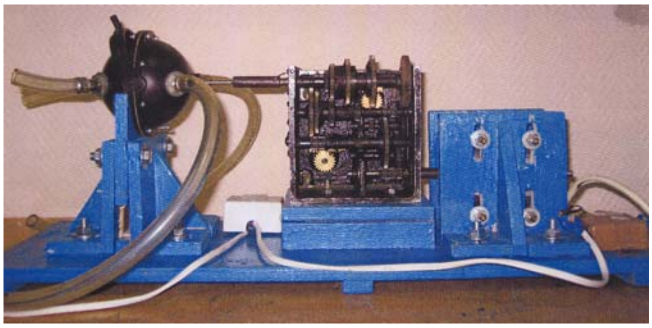

Fig. 6. The experimental apparatus with the new ball pump, gear box (in the middle) and a motor (on the right side)

4. CONCLUSION

1. The new and effective ball pump is created.
2. It can pump over different liquids which have various ductility.
3. Moreover this ball pump can work in a regime as the human heart is working (this fact some of Russian doctors have just confirmed) because the pump works with a pulsation too as our heart does.

REFRENCES

1. Патент 79619 Россия, C1 2008130797/22. 10.01.2009, F01C 3/00. Роторная объёмная машина / Дёжинов Б.А., Войнов К.Н., Черток Е.В. (Россия).